

PRODUCTION OF π^+ , K^+ , K^0 , K^{*0} , ϕ , p and Λ^0 IN HADRONIC Z^0 DECAYS*

The SLD Collaboration**

Stanford Linear Accelerator Center, Stanford University, Stanford, CA 94309

Abstract

We have measured the differential production cross sections as a function of scaled momentum $x_p = 2p/E_{cm}$ of the identified hadron species π^+ , K^+ , K^0 , K^{*0} , ϕ , p , Λ^0 , and of the corresponding antihadron species in inclusive hadronic Z^0 decays, as well as separately for Z^0 decays into light (u , d , s), c and b flavors. Clear flavor dependences are observed, consistent with expectations based upon previously measured production and decay properties of heavy hadrons. These results were used to test the QCD predictions of Gribov and Lipatov, the predictions of QCD in the Modified Leading Logarithm Approximation with the ansatz of Local Parton-Hadron Duality, and the predictions of three fragmentation models. Ratios of production of different hadron species were also measured as a function of x_p and were used to study the suppression of strange meson, strange and non-strange baryon, and vector meson production in the jet fragmentation process. The light-flavor results provide improved tests of the above predictions, as they remove the contribution of heavy hadron production and decay from that of the rest of the fragmentation process. In addition we have compared hadron and antihadron production as a function of x_p in light quark (as opposed to antiquark) jets. Differences are observed at high x_p , providing direct evidence that higher-momentum hadrons are more likely to contain a primary quark or antiquark. The differences for pseudoscalar and vector kaons provide new measurements of strangeness suppression for high- x_p fragmentation products.

Submitted to *Phys. Rev. D*

*Work supported by Department of Energy contracts: DE-FG02-91ER40676, DE-FG03-91ER40618, DE-FG03-92ER40689, DE-FG03-93ER40788, DE-FG02-91ER40672, DE-FG02-91ER40677, DE-AC03-76SF00098, DE-FG02-92ER40715, DE-FC02-94ER40818, DE-FG03-96ER40969, DE-AC03-76SF00515, DE-FG05-91ER40627, DE-FG02-95ER40896, DE-FG02-92ER40704; National Science Foundation grants: PHY-91-13428, PHY-89-21320, PHY-92-04239, PHY-95-10439, PHY-88-19316, PHY-92-03212; The UK Particle Physics and Astronomy Research Council; The Istituto Nazionale di Fisica Nucleare of Italy; The Japan-US Cooperative Research Project on High Energy Physics; The Korea Science and Engineering Foundation.

1 Introduction

The production of jets of hadrons from hard partons produced in high energy collisions is believed to proceed in three stages. Considering the process $e^+e^- \rightarrow q\bar{q}$, the first stage involves the radiation of gluons from the primary quark and antiquark, which in turn may radiate gluons or split into $q\bar{q}$ pairs until their virtuality approaches the hadron mass scale. This process is in principle calculable in perturbative QCD, and three approaches have been taken so far: i) differential cross sections have been calculated [1] for the production of up to 4 partons to second order in the strong coupling α_s , and leading order calculations have been performed recently for as many as 6 partons (see e.g. [2]); ii) certain parton distributions have been calculated to all orders in α_s in the Modified Leading Logarithm Approximation (MLLA) [3]; iii) “parton shower” calculations [4] have been implemented numerically; these consist of an arbitrary number of $q \rightarrow qg$, $g \rightarrow gg$ and $g \rightarrow q\bar{q}$ branchings, with each branching probability determined from QCD in the Leading Logarithm Approximation.

In the second stage these partons transform into “primary” hadrons. This “fragmentation” process is not understood quantitatively and there are few theoretical predictions that do not explicitly involve heavy (c or b) quarks. Using perturbative QCD, Gribov and Lipatov have studied [5] the fragmentation of quarks produced in e^+e^- collisions in the limit of high hadron momentum fraction $x_p = p_{hadron}/E_{beam}$, and have related it to the proton structure function at high $x = E_{quark}/E_{proton}$. They predict that as $x_p \rightarrow 1$ the distribution of x_p for baryons is proportional to $(1 - x_p)^3$, and that for mesons is proportional to $(1 - x_p)^2$. Another approach is to make the ansatz of local parton-hadron duality (LPHD) [3], that inclusive distributions of primary hadrons are the same, up to a normalization factor, as those for partons. Calculations using MLLA QCD, cut off at a virtual parton mass comparable with the mass of the hadron in question, have been used in combination with LPHD to predict that the shape of the distribution of $\xi = \ln(1/x_p)$ for a given primary hadron species is approximately Gaussian within about one unit of the peak, that the shape can be approximated over a wider ξ range by a Gaussian with the addition of small distortion terms, and that the peak position depends inversely on the hadron mass and logarithmically on the center-of-mass (c.m.) energy. It is desirable to test the existing calculations experimentally and to encourage deeper theoretical understanding of the fragmentation process.

In the third stage unstable primary hadrons decay into the stable particles that traverse particle detectors. This stage is understood inasmuch as proper lifetimes and decay branching ratios have been measured for many hadron species. However, these decays complicate fundamental fragmentation measurements because a sizable fraction of the stable particles are decay products rather than primary hadrons, and it is typically not possible to determine the origin of each detected hadron. Previous measurements at e^+e^- colliders (see e.g. [6, 7]) indicate that decays of vector mesons, strange baryons and decuplet baryons produce roughly two-thirds of the stable particles; scalar mesons, tensor mesons and radially excited baryons have also been observed [7], and there are large uncertainties on their contributions. Ideally one would measure every possible hadron species and distinguish primary hadrons from decay products on a statistical basis. A body of knowledge could be assembled by reconstructing heavier and heavier states, and subtracting their known decay products from the measured differential cross sections of lighter hadrons.

Additional complications arise in jets initiated by heavy quarks, since the leading heavy

hadrons carry a large fraction of the beam energy, restricting that available to other primary hadrons, and their decays produce a sizable fraction of the stable particles in the jet. Although decays of some B and D hadrons have been studied inclusively, there are large uncertainties in heavy hadron production, B_s^0 and heavy baryon decay, and the suppression of gluon radiation from heavy quarks. The removal of heavy flavor events will therefore simplify the study of the fragmentation of light quarks into hadrons.

A particularly interesting aspect of fragmentation is the question of what happens to the quark or antiquark that initiated the jet. A common prejudice is that the initial quark is “contained” as a valence constituent of a particular hadron, and that this “leading” hadron has on average a higher momentum than the other hadrons in the jet. The highly polarized electron beam delivered by the SLAC Linear Collider (SLC) gives a unique, high purity, unbiased tag of quark vs. antiquark jets, via the large electroweak forward-backward quark production asymmetry at the Z^0 resonance. We have previously observed [8] evidence for the production of leading baryons, K^\pm and K^{*0}/\bar{K}^{*0} in light-flavor jets. The quantification of leading particle effects could lead to methods for identifying jets of specific light flavors, which could have a number of applications in ep and hadron-hadron collisions as well as in e^+e^- annihilations.

There are several phenomenological models of jet fragmentation, which combine modelling of all three stages of particle production; it is important to test their predictions. To simulate the parton production stage, the HERWIG [9], JETSET [10] and UCLA [11] event generators use a combination of first order matrix elements and a parton shower. To simulate the fragmentation stage, the HERWIG model splits the gluons produced in the first stage into $q\bar{q}$ pairs, and these quarks and antiquarks are paired up locally to form colorless clusters that decay into the primary hadrons. The JETSET model takes a different approach, representing the color field between the partons by a semi-classical string, which is broken, according to an iterative algorithm, into several pieces that correspond to primary hadrons. In the UCLA model, whole events are generated according to weights derived from the phase space available to their final states and the relevant Clebsch-Gordan coefficients. Each of these models contains arbitrary parameters that control various aspects of fragmentation and have been tuned to reproduce data from e^+e^- annihilations. The JETSET model includes a large number of parameters that control, on average, the species of primary hadron produced at each string break, giving it the potential to model the observed properties of identified hadron species in great detail. In the HERWIG model, clusters are decayed into pairs of primary hadrons according to phase space, and the relative production of different hadrons is effectively governed by two parameters controlling the distribution of cluster masses. In the UCLA model, there is only one such free parameter, which controls the degree of locality of baryon-antibaryon pair formation.

In this paper we present an analysis of π^\pm , K^\pm , K^0/\bar{K}^0 , K^{*0}/\bar{K}^{*0} , ϕ , p/\bar{p} , and $\Lambda^0/\bar{\Lambda}^0$ production in hadronic Z^0 decays collected by the SLC Large Detector (SLD). The analysis is based upon the approximately 150,000 hadronic events obtained in runs of the SLC between 1993 and 1995. We measure differential production cross sections for these seven hadron species in an inclusive sample of hadronic Z^0 decays and use the results to test the QCD predictions of Gribov and Lipatov, the predictions of MLLA QCD+LPHD, and the predictions of the three fragmentation models just described, as well as to study the suppression of strange hadrons, baryons, and vector mesons in the fragmentation process. We

also measure these differential cross sections separately in Z^0 decays into light flavors ($u\bar{u}$, $d\bar{d}$ and $s\bar{s}$), $c\bar{c}$ and $b\bar{b}$, which provide improved tests of the QCD predictions, new tests of the fragmentation models that separate the heavy hadron production and decay modelling from that of the rest of the fragmentation process, and cleaner measurements of strangeness, baryon and vector-meson suppression. In addition we update our measurements of hadron and antihadron differential cross sections in light quark jets, and use the results to make additional new tests of the fragmentation models and to make two new measurements of strangeness suppression at high x_p .

In section 2 we describe the SLD, including a detailed description of the Cherenkov Ring Imaging Detector, which is used to identify charged hadrons. In section 3 we describe the selection of hadronic events of different primary flavor, using impact parameters of charged tracks measured in the Vertex Detector, and the selection of light quark and antiquark hemispheres, using the large production asymmetry in polar angle induced by the polarization of the SLC electron beam. In section 4 we describe the hadron identification analyses and present results for flavor-inclusive events. In section 5 we present results separately for light- ($Z^0 \rightarrow u\bar{u}, d\bar{d}, s\bar{s}$), c - ($Z^0 \rightarrow c\bar{c}$) and b -flavor ($Z^0 \rightarrow b\bar{b}$) events. In section 6 we use the flavor-inclusive and light-flavor results to test the QCD predictions of Gribov and Lipatov, and of MLLA QCD+LPHD. In section 7 we extract total production cross sections of each hadron species per hadronic event. In section 8 we update our measurements of leading particle production in light-flavor jets. In section 9 we present ratios of production of pairs of hadrons, and discuss the suppression of strange hadrons, baryons, and vector mesons in the fragmentation process.

2 The SLD

This analysis of data from the SLD [12] used charged tracks measured in the Central Drift Chamber (CDC) [13] and silicon Vertex Detector (VXD) [14], and identified in the Cherenkov Ring Imaging Detector (CRID) [15]. The CDC consists of 80 layers of sense wires arranged in 10 axial or stereo superlayers between 24 and 96 cm from the beam axis. The outermost layer covers the solid angle range $|\cos\theta| < 0.68$. The average spatial resolution for hits attached to charged tracks is $92\ \mu\text{m}$. Momentum measurement is provided by a uniform axial magnetic field of 0.6 T. The VXD and CRID are described in the following subsections.

Energy deposits reconstructed in the Liquid Argon Calorimeter (LAC) [16] were used in the initial hadronic event selection and in the calculation of the event thrust [17] axis. The LAC is a lead-liquid argon sampling calorimeter covering the solid angle range $|\cos\theta| < 0.98$, which is segmented into 33×36 mrad projective towers, each comprising two electromagnetic sections and two hadronic sections, for a total thickness of 2.8 interaction lengths. The energy resolution is measured to be $\sigma = 15\%\sqrt{E}$ for electromagnetic showers and $60\%\sqrt{E}$ for hadronic showers, where E is the energy in GeV.

2.1 The SLD Vertex Detector

Flavor tagging of events for this analysis was accomplished with the original SLD Vertex Detector [14], which was composed of 480 charge-coupled devices containing a total of 120 million $22\times 22\ \mu\text{m}^2$ pixels, arranged in four concentric layers of radius between 2.9 and 4.2

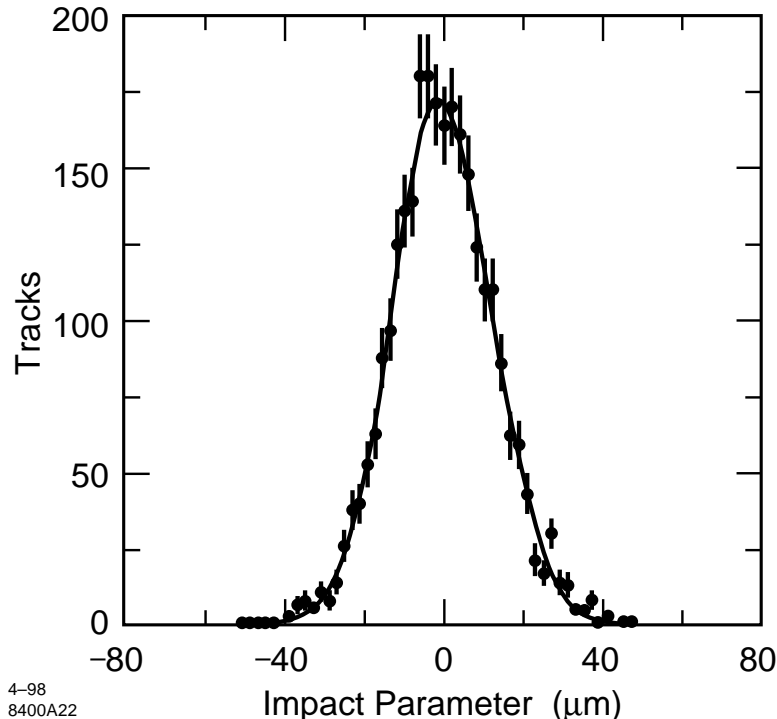


Figure 1: Distribution of transverse impact parameters of tracks in $e^+e^- \rightarrow \mu^+\mu^-$ events with respect to the primary interaction point measured in hadronic events.

cm. The outermost layer covered the solid angle range $|\cos\theta| < 0.75$, and the azimuthal arrangement was such that a track would always encounter one of the two innermost layers and one of the two outermost layers; the average number of reconstructed hits per track was 2.3. The 3-D spatial resolution for these hits was measured to be $5.5 \mu\text{m}$.

Here we used only the information in the plane transverse to the beam axis. The impact parameter resolution in this plane was measured [18] from the distribution of miss distances between the two tracks in $Z^0 \rightarrow \mu^+\mu^-$ events to be $11 \mu\text{m}$ for $45.6 \text{ GeV}/c$ muons reconstructed including at least one hit in the VXD. The transverse position of the primary interaction point (IP) was measured using tracks in sets of ~ 30 sequential hadronic Z^0 decays, with a resolution measured from the distribution of impact parameters in the statistically independent μ -pair event sample (see fig. 1) of $7 \pm 2 \mu\text{m}$. The impact parameter resolution for lower momentum tracks was determined using tracks in hadronic Z^0 decays, corrected for the contributions from decays of heavy hadrons. Including the uncertainty on the IP, a resolution of $11 \oplus 70/(p_\perp \sin^{3/2}\theta) \mu\text{m}$ was obtained, where p_\perp is the track momentum transverse to the beam axis in GeV/c and θ is the polar angle of the track with respect to the beam axis.

2.2 The SLD Cherenkov Ring Imaging Detector

Identification of charged tracks is accomplished with the barrel CRID [15], which covers the solid angle range $|\cos\theta| < 0.68$. Through the combined use of liquid C_6F_{14} and gaseous $\text{C}_5\text{F}_{12} + \text{N}_2$ radiators, the barrel CRID is designed to perform efficient separation of charged pions, kaons and protons over most of the momentum range in e^+e^- annihilations at the

Z^0 , $0.3 < p < 46$ GeV/c. A charged particle that passes through a radiator of refractive index n with velocity β above Cherenkov threshold, $\beta > \beta_0 = 1/n$, emits photons at an angle $\theta_c = \cos^{-1}(1/\beta n)$ with respect to its flight direction. In the SLD, a charged particle exiting the CDC encounters a 1 cm thick liquid radiator, contained in one of 40 radiator trays. If the momentum of the particle is above its liquid Cherenkov threshold, UV photons are emitted in a cone about the particle flight direction. This 1-cm thick cone expands over a standoff distance of ~ 12 cm and each photon can enter one of 40 time projection chambers (TPCs) through an inner quartz window.

The TPCs contain a photosensitive gas, ethane with $\sim 0.1\%$ TMAE [15]. The resulting single photoelectrons drift along the beam direction to a wire chamber where the conversion point of each Cherenkov photon is measured in three dimensions using drift time, wire address and charge division. These positions are used to reconstruct a Cherenkov angle with respect to the extrapolated charged track. Liquid rings span 2–3 TPCs in azimuth and can be split between TPCs in the forward and backward hemispheres.

The particle may then continue through a TPC, where it ionizes the drift gas, saturating the readout electronics, which were designed for single-electron detection, on 2–7 anode wires and effectively deadening ~ 5 cm² of detection area. Following the TPC, the particle passes through ~ 40 cm of the gas radiator volume. Radiated Cherenkov photons are focussed by one of 400 spherical mirrors onto the outer quartz window of a TPC. Gas rings are typically 2.5 cm in radius at the TPC surface, and the mirrors are positioned such that no ring is focussed near an edge of a TPC or near the region saturated by its own track. The mirror arrangement and the large size of the liquid rings make the identification performance largely independent of the proximity of the track to any jet axis.

The average liquid (gas) Cherenkov angle resolution was measured from the data to be 16 (4.5) mrad, including the effects of residual misalignments of the TPCs, radiator trays and mirrors, and track extrapolation resolution. The local or intrinsic resolution was measured to be 13 (3.8) mrad, consistent with the design value. The average number of detected photons per full ring for tracks with $\beta = 1$ was measured in μ -pair events to be 16.1 (10.0). For hadronic events, a set of cuts was applied to reduce backgrounds from spurious hits and cross-talk from saturating hits, resulting in an average of 12.8 (9.2) accepted hits per ring. The average reconstructed Cherenkov angle for $\beta = 1$ tracks was 675 (58.6) mrad, corresponding to an index of refraction of 1.281 (1.00172), and Cherenkov thresholds of 0.17 (2.4) GeV/c for charged pions, 0.62 (8.4) GeV/c for kaons and 1.17 (16.0) GeV/c for protons. This index was found to be independent of position within the CRID and the liquid index was found to be constant in time. Time variations in the gas index of up to ± 0.00007 were tracked with an online monitor and verified in the data.

Tracks were identified using a likelihood technique [19]. For each of the five stable charged particle hypotheses $i = e, \mu, \pi, K, p$, a likelihood L_i was calculated based upon the number of detected photoelectrons and their measured angles, the expected number of photons, the expected Cherenkov angle, and a background term. The background included the effects of overlapping Cherenkov radiation from other tracks in the event as well as a constant term normalized to the number of hits in the TPC in question that were not associated with any track. Particle separation was based upon differences between logarithms of these likelihoods, $\mathcal{L}_i = \ln L_i$.

The particle identification performance of the CRID depends on the track selection and

likelihood difference requirements for a given analysis. Here we discuss the example of the hadron fractions analysis described in section 4.1, where we consider only the three charged hadron hypotheses $i = \pi, K, p$. For tracks with $p < 2.5$ ($p > 2.5$) GeV/c, a particle was identified as species j if \mathcal{L}_j exceeded both of the other log-likelihoods by at least 5 (3) units. We quantify the performance in terms of a momentum-dependent identification efficiency matrix \mathbf{E} , each element E_{ij} of which represents the probability that a selected track from a true i -hadron is identified as a j -hadron, with $i, j = \pi, K, p$. The elements of this matrix were determined where possible from the data [20]. For example, tracks from selected K_s^0 and τ decays were used as “pion” test samples, having estimated kaon plus proton contents of 0.3% and 1.7% respectively. Figure 2 shows the probability for these tracks to be identified as pions, kaons and protons as a function of momentum. Also shown are results of the same analysis of corresponding samples from a detailed Monte Carlo (MC) simulation of the detector. The MC describes the momentum dependence well and reproduces the efficiencies to within ± 0.03 . Functional forms were fitted to the data, chosen to describe the momentum dependence of both data and simulated test samples, as well as that of simulated true pions in hadronic events. The simulation was used to correct the fitted parameters for non-pion content in the K_s^0 and τ samples and differences in tracking performance between tracks in these samples and those from the IP in hadronic events. The resulting identification efficiency functions, $E_{\pi\pi}$, $E_{\pi K}$ and $E_{\pi p}$, are shown in the leftmost column of fig. 3.

A similar procedure using only π and p likelihoods was used to measure the π - p separation in the liquid (gas) system for $p > 2$ (17) GeV/c, and the simulation was used to convert that into E_{pp} , shown in the bottom right of fig. 3. E_{pp} over the remaining momentum range, as well as the π - K separation in the gas system below and near kaon threshold ($p < 10$ GeV/c), was measured using protons from decays of tagged lambda hyperons [20]. The remaining efficiencies in fig. 3 were derived from those measured, using the simulation. For example, E_{KK} is equal to $E_{\pi\pi}$ for momenta in the ranges $1.5 < p < 2.5$ and $15 < p < 25$ GeV/c, since both species are well above the relevant Cherenkov threshold and their expected Cherenkov angles differ from that of the proton by an amount large compared with the angular resolution. Outside these ranges, E_{KK} was related to $E_{\pi\pi}$ by a function derived from the simulation to account for the effects of the reduced photon yield near the kaon Cherenkov threshold and the fact that the expected kaon ring radius lies between those of the pion and proton.

The bands in fig. 3 encompass the upper and lower systematic error bounds on the efficiencies. The discontinuities correspond to the π and K Cherenkov thresholds in the gas radiator. For the diagonal elements, the systematic errors correspond to errors on the fitted parameters and are strongly positively correlated across each of the three momentum regions. For the off-diagonal elements, representing misidentification rates, a more conservative 25% relative error was assigned at all points to account for the limited experimental constraints on the momentum dependence. These errors are also strongly positively correlated among momenta. The identification efficiencies in fig. 3 peak near or above 0.9 and the pion coverage is continuous from 0.3 GeV/c up to approximately 35 GeV/c. There is a gap in the kaon-proton separation between about 7 and 10 GeV/c due to the limited resolution of the liquid system and the fact that neither species is far above Cherenkov threshold in the gas system. The proton coverage extends to the beam momentum. Misidentification rates are typically less than 0.03, with peak values of up to 0.07.

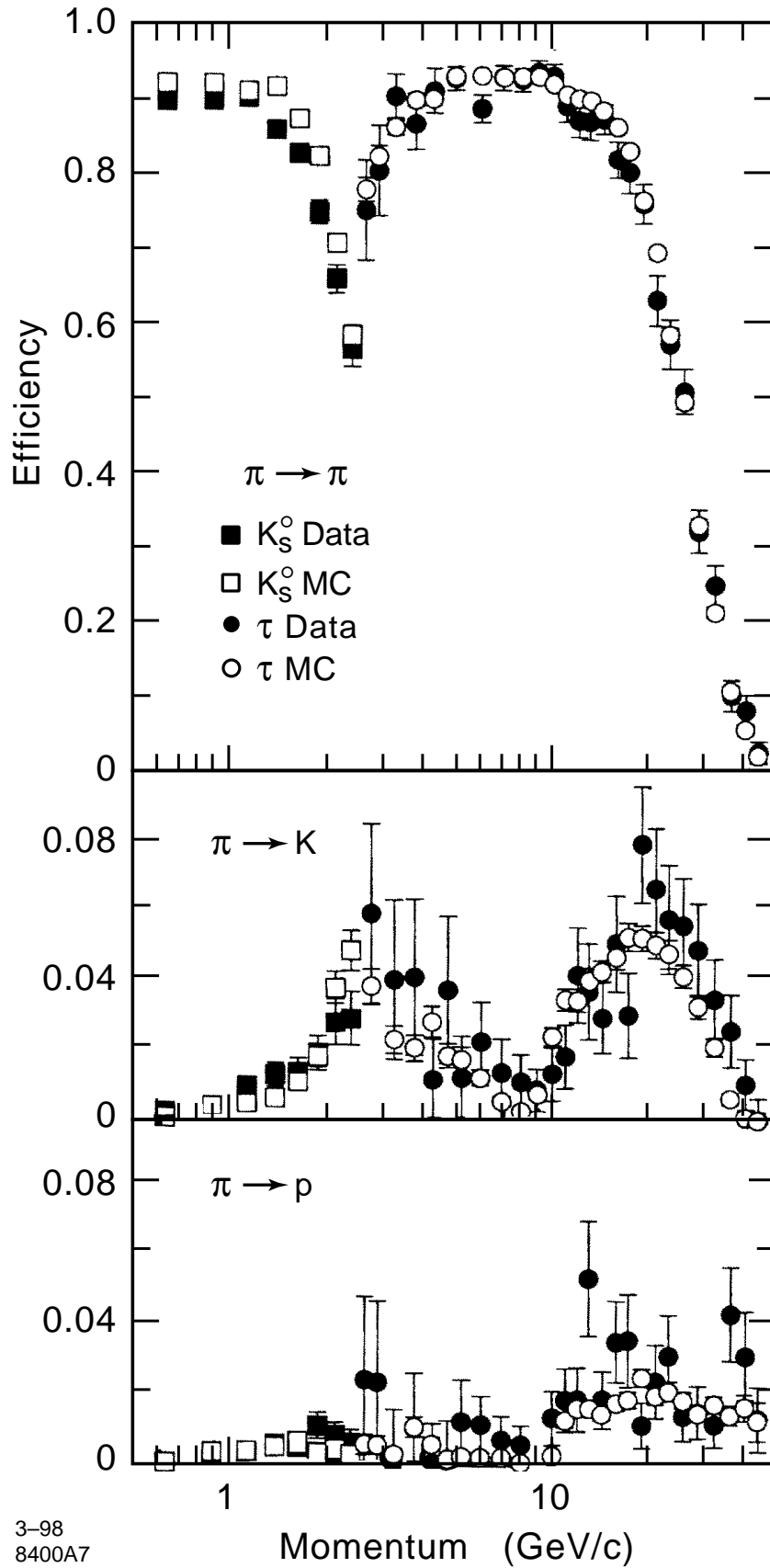
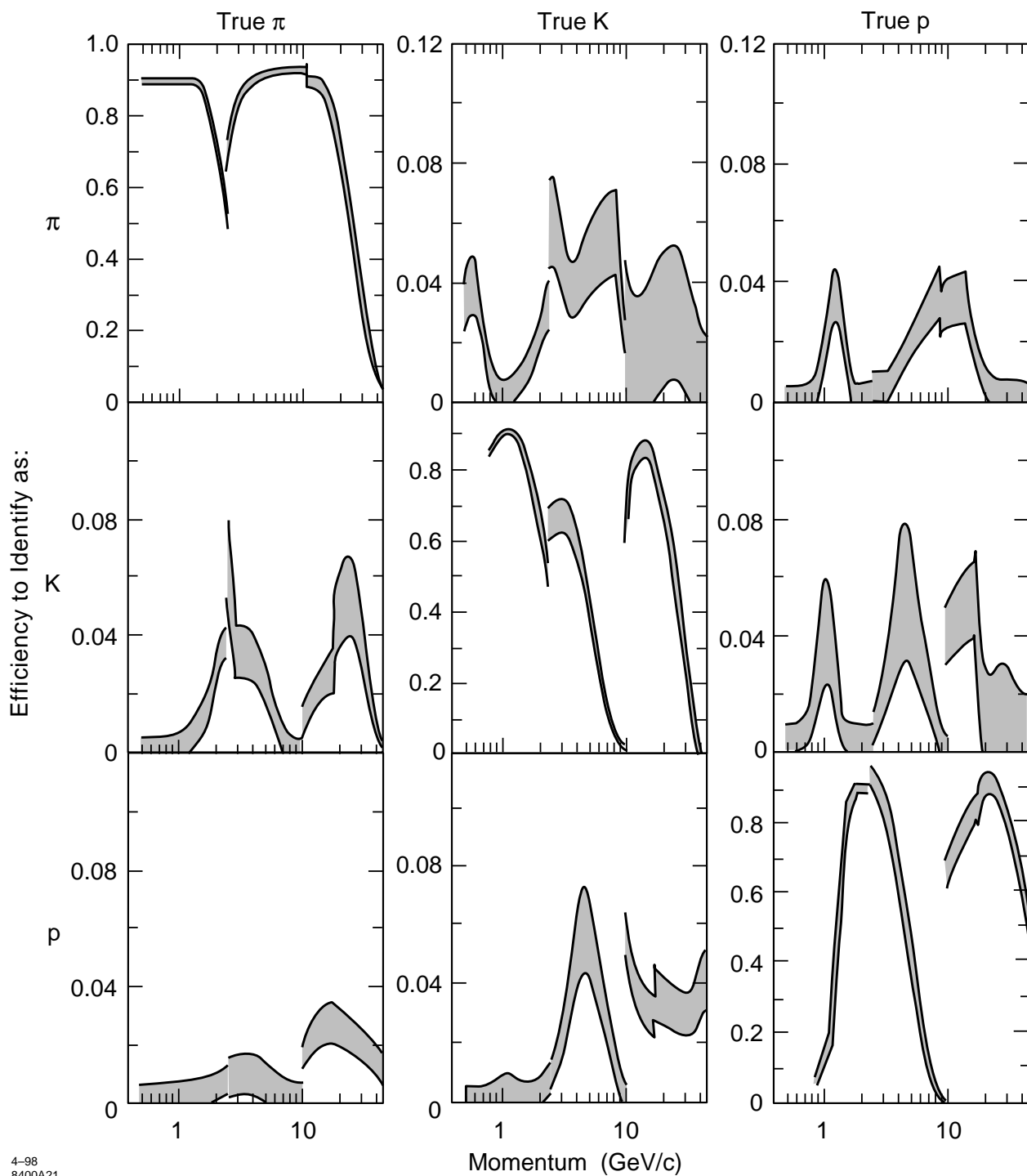


Figure 2: Efficiencies for selected tracks from K_s^0 (squares) and τ (circles) decays to be identified as each hadron species in the CRID. The solid symbols represent the data and the open symbols the simulation.



4-98
8400A21

Figure 3: Calibrated identification efficiencies for tracks used in the charged hadron fractions analysis. The half-widths of the grey bands represent the systematic uncertainties, which are strongly correlated between momenta. Note the expanded vertical scale for the off-diagonal efficiencies.

	Efficiency for $Z^0 \rightarrow$			Composition		
	$u\bar{u}, d\bar{d}, s\bar{s}$	$c\bar{c}$	$b\bar{b}$	$u\bar{u}, d\bar{d}, s\bar{s}$	$c\bar{c}$	$b\bar{b}$
light-tag	0.845	0.438	0.075	0.849	0.124	0.027
c -tag	0.153	0.478	0.331	0.378	0.333	0.290
b -tag	0.002	0.084	0.594	0.009	0.100	0.891

Table 1: Efficiencies for simulated events in the three flavor categories to be tagged as light, c or b events. The three rightmost columns indicate the composition of each simulated tagged sample assuming the Standard Model relative flavor production.

3 Event Selection

The trigger and initial selection of hadronic events are described in [21]. The analysis presented here is based on charged tracks measured in the CDC and VXD. A set of cuts was applied in order to select events well-contained within the detector acceptance. Tracks were required to have (i) a closest approach to the beam axis within 5 cm, and within 10 cm along the beam axis of the measured IP, (ii) a polar angle θ with respect to the beam axis with $|\cos\theta| < 0.80$, (iii) a momentum transverse to this axis $p_{\perp} > 150$ MeV/ c , and (iv) a momentum $p < 50$ GeV/ c . Events were required: to contain a minimum of seven such tracks; to contain a minimum visible energy $E_{vis} > 18$ GeV, calculated from the accepted tracks, assigned the charged pion mass; to have a thrust axis polar angle θ_t with respect to the beam axis, calculated from calorimeter clusters, with $|\cos\theta_t| < 0.71$; and to have good VXD data [18] and a well-measured IP position. A sample of 90,213 events passed these cuts. For the analyses using the CRID, the additional requirements were made that the CRID high voltage was on and that there was a good drift velocity measurement, resulting in a sample of 79,711 events. The non-hadronic background was estimated to be 0.1%, dominated by $Z^0 \rightarrow \tau^+\tau^-$ events.

Samples of events enriched in light and b primary flavors were selected based on signed impact parameters δ of charged tracks with respect to the IP in the plane transverse to the beam. For each event we define n_{sig} to be the number of tracks passing a set of impact-parameter quality cuts [18] that have impact parameter greater than three times its estimated error, $\delta > 3\sigma_{\delta}$. Events with $n_{sig} = 0$ were assigned to the light-tagged sample and those with $n_{sig} \geq 3$ were assigned to the b -tagged sample. The remaining events were classified as a c -tagged sample. The light-, c - and b -tagged samples comprised 60.4%, 24.5% and 15.2% of the selected hadronic events, respectively. The tagging efficiencies and sample purities were estimated from our Monte Carlo simulation and are listed in table 1.

Separate samples of hemispheres enriched in light-quark and light-antiquark jets were selected from the light-tagged event sample by exploiting the large electroweak forward-backward production asymmetry with respect to the beam direction. The event thrust axis was used to approximate the initial $q\bar{q}$ axis and was signed such that its z -component was along the electron beam direction, $\hat{t}_z > 0$. Events in the central region of the detector, where the production asymmetry is small, were removed by the requirement $|\hat{t}_z| > 0.2$, leaving 74%

of the light-tagged events. The quark-tagged hemisphere in events with left- (right-)handed electron beam polarization was defined to comprise the set of tracks with positive (negative) momentum projection along the signed thrust axis. The remaining tracks in each event were defined to be in the antiquark-tagged hemisphere. For the selected event sample, the average magnitude of the polarization was 0.73. Using this value and assuming Standard Model couplings, a tree-level calculation gives a quark (antiquark) purity of 0.73 in the quark-(antiquark-)tagged sample.

4 Hadron Identification Analysis

In the following subsections we discuss details of the analysis for three categories of identified hadrons: charged tracks identified as π^\pm , K^\pm or p/\bar{p} in the CRID; K_s^0 and $\Lambda^0/\bar{\Lambda}^0$ reconstructed in their charged decay modes and tagged by their long flight distance; and K^{*0}/\bar{K}^{*0} and ϕ reconstructed in charged decay modes including one and two identified K^\pm , respectively. The resulting differential cross sections for these seven hadron species in inclusive hadronic Z^0 decays are presented in the last subsection.

4.1 Charged Hadron Fractions

Reconstructed charged tracks were identified as charged pions, kaons or protons using information from only the CRID liquid (gas) radiator for tracks with $p < 2.5$ ($p > 7.5$) GeV/c; in the overlap region, $2.5 < p < 7.5$ GeV/c, liquid and gas information was combined. Additional track selection cuts [20] were applied to remove tracks that interacted or scattered through large angles before exiting the CRID and to ensure that the CRID performance was well-modelled by the simulation. Tracks were required to have at least 40 CDC hits, at least one of which was at a radius of at least 92 cm, to extrapolate through an active region of the appropriate radiator(s), and to have at least 80 (100)% of their expected liquid (gas) ring contained within a sensitive region of the CRID TPCs. The latter requirement included rejection of tracks with $p > 2.5$ GeV/c for which there was a saturated CRID hit within a 5 cm radius (twice the maximum ring radius) of the expected gas ring center. Tracks with $p < 7.5$ GeV/c were required to have a saturated hit within 1 cm of the extrapolated track, and tracks with $p > 2.5$ GeV/c were required to have either such a saturated hit or the presence of at least four hits consistent with a liquid ring. These cuts accepted 47%, 28% and 43% of the tracks within the CRID acceptance in the momentum ranges $p < 2.5$, $2.5 < p < 7.5$ and $p > 7.5$ GeV/c, respectively. For momenta below 2 GeV/c, only negatively charged tracks were used in order to reduce the background from protons produced in particle interactions with the detector material.

In each momentum bin we measured the fractions of the selected tracks that were identified as pions, kaons and protons. The observed fractions were related to the true production fractions by an efficiency matrix, composed of the values shown in fig. 3. This matrix was inverted and used to unfold our observed identified hadron fractions. This analysis procedure does not require that the sum of the charged hadron fractions be unity; instead the sum was used as a consistency check, which was found to be satisfied at all momenta (see fig. 4). In some momentum regions we cannot distinguish two of the three hadron species, so the procedure was reduced to a 2×2 matrix analysis and we present only the fraction of

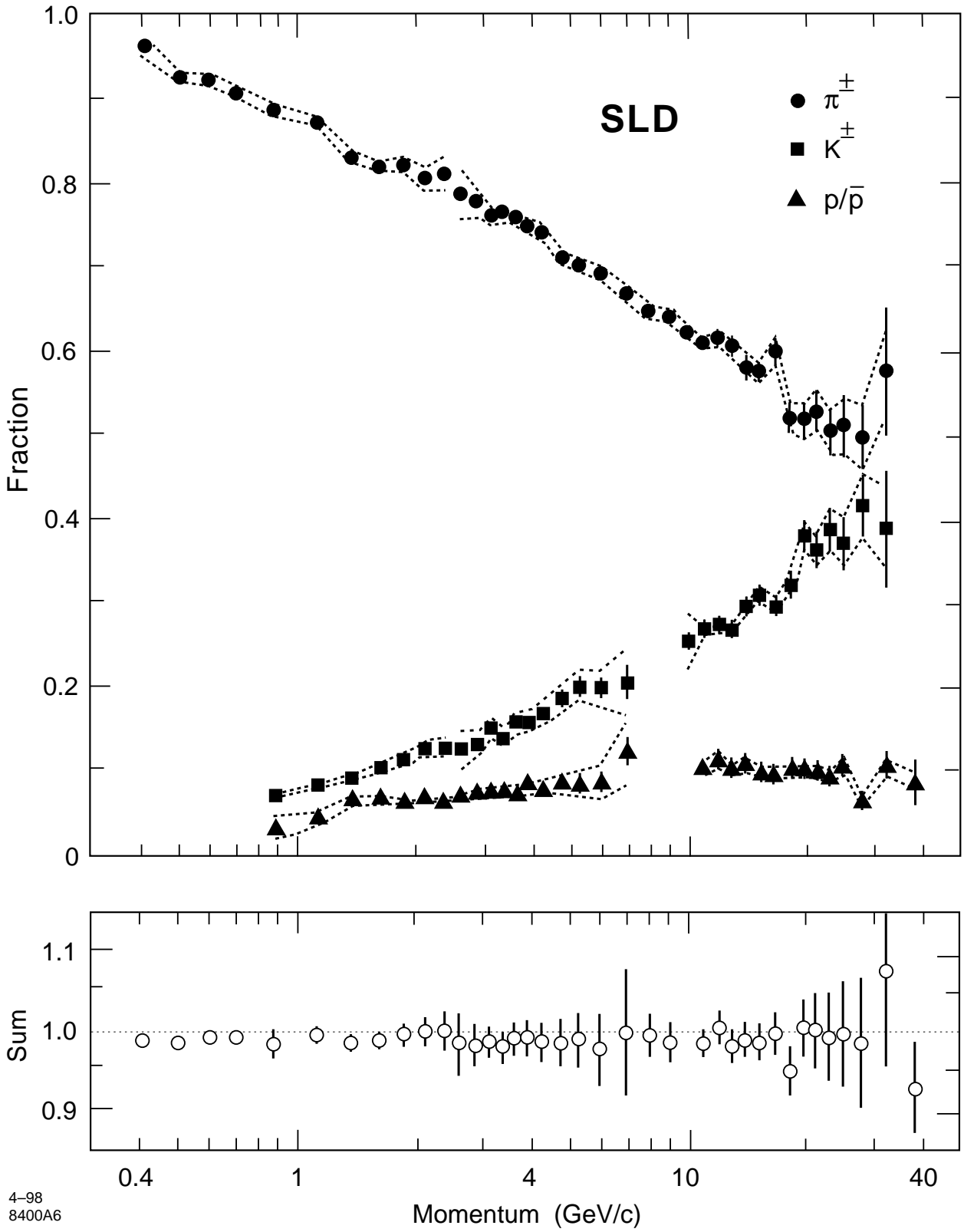
the identified species, i.e. protons above 35 GeV/c and pions below 0.75 GeV/c and between 7.5 and 9.5 GeV/c.

Electrons and muons were not distinguished from pions; this background was estimated from the simulation to be about 5% of the tracks in the inclusive flavor sample, predominantly from c - and b -flavor events. The fractions were corrected using the simulation for the lepton backgrounds, as well as for the effects of beam-related backgrounds, particles interacting in the detector material, and particles decaying outside the tracking volume. The conventional definition of a final-state charged hadron was used, namely a charged pion, kaon or proton that is either from the primary interaction or a direct decay product of a hadron that has proper lifetime less than 3×10^{-10} s and is itself a primary or a decay product of a primary hadron.

The measured charged hadron fractions in inclusive hadronic Z^0 decays are shown in fig. 4 and listed in tables 2–4. The systematic errors were determined by propagating the errors on the calibrated efficiency matrix (see sec. 2.2) and correspond to uncertainties in the average number of photons detected per track and the average resolution on the measured Cherenkov angles. They are therefore strongly positively correlated across each of the three momentum regions, $p < 2.5$, $2.5 < p < 7.5$ and $p > 7.5$ GeV/c, and are indicated by the pairs of dashed lines in fig. 4. The errors on the points below ~ 6 GeV/c are dominated by the systematic uncertainties; for the points above ~ 15 GeV/c the errors have roughly equal statistical and systematic contributions.

Pions are seen to dominate the charged hadron production at low momentum, and to decline steadily in fraction as momentum increases. The kaon fraction rises steadily to about one-third at high momentum. The proton fraction rises to a plateau value of about one-tenth at about 10 GeV/c. Where the momentum coverage overlaps, these measured fractions were found to be consistent with an average of previous measurements at the Z^0 [22, 23, 24]. Measurements based on ring imaging and those based on ionization energy loss rates cover complementary momentum ranges and can be combined to provide continuous coverage over the range $0.22 < p < 45.6$ GeV/c.

Differential production cross sections were obtained by multiplying these fractions by our measured inclusive charged particle differential cross section, corrected, using our simulation, for the contribution from leptons. The integral of this cross section was constrained to be 20.95 tracks per event, an average [25] of charged multiplicity measurements in Z^0 decays, and the momentum-dependence of our track reconstruction efficiency was checked by comparing the momentum distributions of charged tracks in data and simulated τ^\pm decays. We include a 1.7% error on the average multiplicity as a systematic normalization uncertainty, as well as a momentum-dependent uncertainty of $0.11 \times |p - 3.8 \text{ GeV/c}| \%$, derived from the study of τ^\pm decays. The inclusive charged particle differential cross section is listed in table 5, and the resulting differential cross sections per hadronic event per unit x_p for the identified hadrons are listed in tables 2–4. The 1.7% normalization uncertainty is not included in the systematic error listed for any of the identified hadrons, nor is it included in the error bars in any of the figures.



4-98
8400A6

Figure 4: Measured charged hadron production fractions in hadronic Z^0 decays. The circles represent the π^\pm fraction, the squares the K^\pm fraction, the triangles the p/\bar{p} fraction, and the open circles the sum of the three fractions. The error bars in the upper plot are statistical only; the dashed lines indicate the systematic errors, which are strongly correlated between momenta. The error bars on the sum are statistical and systematic added in quadrature.

x_p Range	$\langle x_p \rangle$	f_π	$1/N \, dn_\pi/dx_p$
0.008–0.010	0.009	0.963±0.004±0.014	482.3±2.3 ±7.2
0.010–0.012	0.011	0.924±0.004±0.006	439.0±2.3 ±3.7
0.012–0.014	0.013	0.921±0.003±0.006	400.5±2.0 ±3.3
0.014–0.016	0.015	0.906±0.004±0.006	356.1±1.9 ±3.0
0.016–0.022	0.019	0.886±0.002±0.006	292.8±1.0 ±2.4
0.022–0.027	0.025	0.872±0.003±0.006	228.5±1.0 ±1.9
0.027–0.033	0.030	0.831±0.003±0.006	176.6±0.9 ±1.4
0.033–0.038	0.036	0.820±0.004±0.006	144.4±0.8 ±1.2
0.038–0.044	0.041	0.823±0.004±0.010	121.7±0.8 ±1.6
0.044–0.049	0.047	0.806±0.006±0.015	102.5±0.9 ±1.9
0.049–0.055	0.052	0.812±0.008±0.020	89.2±0.9 ±2.2
0.055–0.060	0.058	0.788±0.007±0.029	75.3±0.8 ±2.8
0.060–0.066	0.063	0.779±0.007±0.016	66.0±0.7 ±1.4
0.066–0.071	0.069	0.763±0.007±0.010	57.81±0.60 ±0.81
0.071–0.077	0.074	0.767±0.007±0.009	51.63±0.56 ±0.60
0.077–0.082	0.079	0.761±0.007±0.009	45.95±0.52 ±0.54
0.082–0.088	0.085	0.750±0.007±0.008	41.35±0.49 ±0.49
0.088–0.099	0.093	0.743±0.006±0.008	35.24±0.32 ±0.42
0.099–0.110	0.104	0.714±0.006±0.008	28.12±0.29 ±0.35
0.110–0.121	0.115	0.705±0.007±0.009	23.57±0.27 ±0.30
0.121–0.143	0.131	0.695±0.005±0.009	18.32±0.17 ±0.24
0.143–0.164	0.153	0.670±0.006±0.009	13.22±0.14 ±0.19
0.164–0.186	0.175	0.651±0.006±0.009	9.84±0.11 ±0.15
0.186–0.208	0.197	0.644±0.007±0.008	7.47±0.09 ±0.11
0.208–0.230	0.219	0.625±0.008±0.007	5.711±0.083±0.080
0.230–0.252	0.241	0.611±0.009±0.006	4.414±0.074±0.063
0.252–0.274	0.263	0.618±0.010±0.010	3.612±0.068±0.072
0.274–0.296	0.285	0.608±0.011±0.010	2.886±0.061±0.060
0.296–0.318	0.307	0.583±0.012±0.011	2.206±0.054±0.049
0.318–0.351	0.334	0.578±0.012±0.012	1.739±0.040±0.044
0.351–0.384	0.366	0.603±0.014±0.015	1.350±0.036±0.040
0.384–0.417	0.400	0.523±0.017±0.016	0.874±0.031±0.032
0.417–0.450	0.432	0.520±0.021±0.020	0.670±0.029±0.029
0.450–0.482	0.465	0.534±0.024±0.024	0.520±0.026±0.025
0.482–0.526	0.503	0.508±0.028±0.027	0.355±0.021±0.020
0.526–0.570	0.547	0.514±0.036±0.031	0.248±0.018±0.016
0.570–0.658	0.609	0.501±0.040±0.038	0.146±0.012±0.012
0.658–0.768	0.704	0.580±0.076±0.053	0.071±0.009±0.007
Total Observed/Evt.			14.52±0.02 ±0.27

Table 2: Charged pion fraction f_π and differential cross section $(1/N)dn_\pi/dx_p$ per hadronic Z^0 decay. $\langle x_p \rangle$ is the average x_p -value of charged tracks in each bin. The last row gives the integral over the x_p range of the measurement. The first error is statistical, the second systematic. A 1.7% normalization uncertainty is included in the systematic error on the integral, but not in those on the cross section.

x_p Range	$\langle x_p \rangle$	f_K	$1/N \, dn_K/dx_p$
0.016–0.022	0.019	0.067±0.001±0.002	22.28±0.47 ±0.53
0.022–0.027	0.025	0.081±0.002±0.002	21.22±0.45 ±0.62
0.027–0.033	0.030	0.090±0.002±0.003	19.10±0.43 ±0.64
0.033–0.038	0.036	0.102±0.002±0.005	18.02±0.43 ±0.80
0.038–0.044	0.041	0.111±0.003±0.006	16.45±0.45 ±0.94
0.044–0.049	0.047	0.127±0.004±0.008	16.13±0.49 ±1.03
0.049–0.055	0.052	0.127±0.005±0.010	13.98±0.53 ±1.14
0.055–0.060	0.058	0.125±0.006±0.022	11.96±0.54 ±2.11
0.060–0.066	0.063	0.130±0.006±0.015	11.03±0.49 ±1.27
0.066–0.071	0.069	0.150±0.006±0.012	11.37±0.46 ±0.87
0.071–0.077	0.074	0.139±0.007±0.012	9.38±0.44 ±0.79
0.077–0.082	0.079	0.157±0.007±0.013	9.51±0.44 ±0.76
0.082–0.088	0.085	0.157±0.008±0.013	8.68±0.44 ±0.72
0.088–0.099	0.093	0.168±0.007±0.014	7.96±0.31 ±0.68
0.099–0.110	0.104	0.187±0.009±0.016	7.37±0.34 ±0.63
0.110–0.121	0.115	0.202±0.011±0.018	6.74±0.37 ±0.60
0.121–0.143	0.131	0.199±0.011±0.023	5.24±0.29 ±0.61
0.143–0.164	0.153	0.207±0.020±0.041	4.08±0.40 ±0.80
0.208–0.230	0.219	0.256±0.009±0.033	2.34±0.08 ±0.30
0.230–0.252	0.241	0.269±0.009±0.007	1.947±0.065±0.057
0.252–0.274	0.263	0.274±0.009±0.007	1.603±0.057±0.042
0.274–0.296	0.285	0.270±0.010±0.006	1.281±0.050±0.034
0.296–0.318	0.307	0.298±0.011±0.007	1.127±0.045±0.030
0.318–0.351	0.334	0.310±0.011±0.008	0.933±0.034±0.027
0.351–0.384	0.366	0.299±0.012±0.009	0.669±0.029±0.023
0.384–0.417	0.400	0.324±0.015±0.012	0.541±0.026±0.023
0.417–0.450	0.432	0.383±0.019±0.016	0.493±0.026±0.023
0.450–0.482	0.465	0.366±0.022±0.019	0.357±0.023±0.020
0.482–0.526	0.503	0.391±0.025±0.023	0.273±0.019±0.018
0.526–0.570	0.547	0.374±0.032±0.028	0.180±0.016±0.014
0.570–0.658	0.609	0.420±0.037±0.036	0.122±0.011±0.011
0.658–0.768	0.704	0.392±0.070±0.049	0.048±0.009±0.006
Total Observed/Evt.			1.800±0.016±0.124

Table 3: Charged kaon fraction and differential cross section per hadronic Z^0 decay.

x_p Range	$\langle x_p \rangle$	f_p	$1/N \, dn_p/dx_p$
0.016–0.022	0.019	$0.029 \pm 0.005 \pm 0.013$	$9.55 \pm 1.55 \pm 4.33$
0.022–0.027	0.025	$0.041 \pm 0.003 \pm 0.008$	$10.79 \pm 0.84 \pm 2.09$
0.027–0.033	0.030	$0.064 \pm 0.002 \pm 0.005$	$13.56 \pm 0.47 \pm 0.98$
0.033–0.038	0.036	$0.065 \pm 0.002 \pm 0.004$	$11.54 \pm 0.35 \pm 0.63$
0.038–0.044	0.041	$0.061 \pm 0.002 \pm 0.002$	$9.03 \pm 0.30 \pm 0.25$
0.044–0.049	0.047	$0.067 \pm 0.002 \pm 0.002$	$8.52 \pm 0.29 \pm 0.23$
0.049–0.055	0.052	$0.062 \pm 0.002 \pm 0.002$	$6.83 \pm 0.26 \pm 0.22$
0.055–0.060	0.058	$0.072 \pm 0.003 \pm 0.005$	$6.85 \pm 0.28 \pm 0.48$
0.060–0.066	0.063	$0.074 \pm 0.003 \pm 0.005$	$6.70 \pm 0.28 \pm 0.42$
0.066–0.071	0.069	$0.075 \pm 0.004 \pm 0.005$	$5.69 \pm 0.27 \pm 0.40$
0.071–0.077	0.074	$0.075 \pm 0.004 \pm 0.006$	$5.03 \pm 0.27 \pm 0.38$
0.077–0.082	0.079	$0.072 \pm 0.004 \pm 0.006$	$4.33 \pm 0.27 \pm 0.38$
0.082–0.088	0.085	$0.085 \pm 0.005 \pm 0.007$	$4.65 \pm 0.29 \pm 0.39$
0.088–0.099	0.093	$0.077 \pm 0.004 \pm 0.009$	$3.64 \pm 0.20 \pm 0.41$
0.099–0.110	0.104	$0.087 \pm 0.006 \pm 0.012$	$3.42 \pm 0.23 \pm 0.45$
0.110–0.121	0.115	$0.084 \pm 0.007 \pm 0.015$	$2.80 \pm 0.25 \pm 0.49$
0.121–0.143	0.131	$0.085 \pm 0.008 \pm 0.021$	$2.22 \pm 0.21 \pm 0.54$
0.143–0.164	0.153	$0.123 \pm 0.016 \pm 0.039$	$2.42 \pm 0.32 \pm 0.77$
0.230–0.252	0.241	$0.106 \pm 0.007 \pm 0.010$	$0.767 \pm 0.048 \pm 0.074$
0.252–0.274	0.263	$0.114 \pm 0.007 \pm 0.010$	$0.668 \pm 0.043 \pm 0.059$
0.274–0.296	0.285	$0.105 \pm 0.008 \pm 0.009$	$0.497 \pm 0.036 \pm 0.044$
0.296–0.318	0.307	$0.109 \pm 0.008 \pm 0.009$	$0.413 \pm 0.032 \pm 0.035$
0.318–0.351	0.334	$0.099 \pm 0.007 \pm 0.009$	$0.296 \pm 0.022 \pm 0.026$
0.351–0.384	0.366	$0.098 \pm 0.008 \pm 0.008$	$0.219 \pm 0.018 \pm 0.019$
0.384–0.417	0.400	$0.105 \pm 0.009 \pm 0.007$	$0.175 \pm 0.015 \pm 0.013$
0.417–0.450	0.432	$0.104 \pm 0.010 \pm 0.007$	$0.134 \pm 0.013 \pm 0.009$
0.450–0.482	0.465	$0.103 \pm 0.011 \pm 0.006$	$0.101 \pm 0.011 \pm 0.006$
0.482–0.526	0.503	$0.095 \pm 0.011 \pm 0.006$	$0.066 \pm 0.008 \pm 0.004$
0.526–0.570	0.547	$0.110 \pm 0.013 \pm 0.006$	$0.053 \pm 0.006 \pm 0.003$
0.570–0.658	0.609	$0.066 \pm 0.010 \pm 0.006$	$0.019 \pm 0.003 \pm 0.002$
0.658–0.768	0.704	$0.107 \pm 0.016 \pm 0.007$	$0.013 \pm 0.002 \pm 0.001$
0.768–0.987	0.836	$0.087 \pm 0.027 \pm 0.012$	$0.002 \pm 0.001 \pm 0.000$
Total Observed/Evt.			$0.864 \pm 0.015 \pm 0.106$

Table 4: Proton fraction and differential cross section per hadronic Z^0 decay.

x_p Range	$\langle x_p \rangle$	$1/N \, dn_{chg}/dx_p$
0.008–0.010	0.009	509.6±1.6 ±8.9
0.010–0.012	0.011	481.9±1.6 ±8.4
0.012–0.014	0.013	440.9±1.5 ±7.7
0.014–0.016	0.015	398.0±1.4 ±6.9
0.016–0.022	0.019	334.6±0.9 ±5.8
0.022–0.027	0.025	265.2±0.8 ±4.6
0.027–0.033	0.030	215.2±0.7 ±3.7
0.033–0.038	0.036	178.6±0.6 ±3.1
0.038–0.044	0.041	150.0±0.6 ±2.6
0.044–0.049	0.047	129.2±0.5 ±2.2
0.049–0.055	0.052	111.7±0.5 ±1.9
0.055–0.060	0.058	97.2±0.5 ±1.7
0.060–0.066	0.063	86.3±0.4 ±1.5
0.066–0.071	0.069	77.2±0.4 ±1.3
0.071–0.077	0.074	68.7±0.4 ±1.2
0.077–0.082	0.079	61.6±0.4 ±1.0
0.082–0.088	0.085	56.35±0.35 ±0.96
0.088–0.099	0.093	48.53±0.23 ±0.83
0.099–0.110	0.104	40.40±0.21 ±0.69
0.110–0.121	0.115	34.32±0.20 ±0.59
0.121–0.143	0.131	27.12±0.12 ±0.47
0.143–0.164	0.153	20.35±0.11 ±0.35
0.164–0.186	0.175	15.65±0.09 ±0.28
0.186–0.208	0.197	12.05±0.08 ±0.22
0.208–0.230	0.219	9.50±0.07 ±0.17
0.230–0.252	0.241	7.54±0.07 ±0.14
0.252–0.274	0.263	6.11±0.06 ±0.12
0.274–0.296	0.285	4.969±0.053±0.098
0.296–0.318	0.307	3.978±0.048±0.081
0.318–0.351	0.334	3.163±0.035±0.067
0.351–0.384	0.366	2.367±0.030±0.052
0.384–0.417	0.400	1.767±0.026±0.041
0.417–0.450	0.432	1.359±0.023±0.033
0.450–0.482	0.465	1.028±0.019±0.026
0.482–0.526	0.503	0.735±0.014±0.020
0.526–0.570	0.547	0.503±0.012±0.015
0.570–0.658	0.609	0.300±0.006±0.009
0.658–0.768	0.704	0.123±0.003±0.004
0.768–0.987	0.836	0.027±0.001±0.001

Table 5: Differential cross section $(1/N)dn_{chg}/dx_p$ for inclusive charged particle production per hadronic Z^0 decay. The first error is statistical, the second systematic.

4.2 Neutral K^0/\bar{K}^0 and $\Lambda^0/\bar{\Lambda}^0$ Production

We reconstructed the charged decay modes $K_s^0 \rightarrow \pi^+\pi^-$ and $\Lambda^0(\bar{\Lambda}^0) \rightarrow p\pi^-(\bar{p}\pi^+)$ [26], collectively referred to as V^0 decays. In order to ensure good invariant mass resolution tracks were required to have a minimum transverse momentum of 150 MeV/c with respect to the beam direction, at least 40 hits measured in the CDC, and a polar angle satisfying $|\cos\theta| < 0.8$.

Pairs of oppositely charged tracks satisfying these requirements were combined to form V^0 s if their separation was less than 15 mm at their point of closest approach in 3 dimensions. A χ^2 fit of the two tracks to a common vertex was performed, and to reject combinatoric background we required: the confidence level of the χ^2 to be greater than 2%; the vertex to be separated from the IP by at least 1 mm, and by at least $5\sigma_l$, where σ_l is the calculated error on the separation length of the V^0 ; and vertices reconstructed outside the Vertex Detector to have at most one VXD hit assigned to each track.

The two invariant masses $m_{\pi\pi}$ and $m_{p\pi}$ were calculated for each V^0 with, in the latter case, the proton (charged pion) mass assigned to the higher-(lower)-momentum track. In the plane perpendicular to the beam, the angle between the vector sum of the momenta of the two charged tracks and the line joining the IP to the vertex was required to be less than both 60 mrad and $k \cdot (2 + 20/p_\perp + 5/p_\perp^2)$ mrad. Here, p_\perp is the component of the vector sum momentum transverse to the beam in units of GeV/c and $k=1.75$ for $\Lambda^0/\bar{\Lambda}^0$ candidates and 2.5 for K_s^0 candidates. For $\Lambda^0/\bar{\Lambda}^0$ candidates, a minimum vector-sum momentum of 500 MeV/c was required.

Note that it is possible for one V^0 to be considered a candidate for both the K_s^0 and $\Lambda^0/\bar{\Lambda}^0$ hypotheses. Kinematic regions exist where the two hypotheses cannot be distinguished without particle identification. In addition there is background from other processes that occur away from the IP, most notably γ -conversions into e^+e^- pairs. Depending upon the type of analysis, such “kinematic-overlaps” may introduce important biases. In this analysis, the kinematic-overlap region was removed only when it distorted the relevant invariant mass distribution. For the K_s^0 analysis, the $\Lambda^0/\bar{\Lambda}^0$ background causes an asymmetric bump in the $m_{\pi\pi}$ distribution, which complicated the subsequent fitting procedure. A cut on the π^+ helicity angle θ_π^* , defined as the angle between the π^+ momentum vector in the K_s^0 rest frame and the K_s^0 flight direction, of $|\cos\theta_\pi^*| \leq 0.8$ was used to remove the Λ^0 , $\bar{\Lambda}^0$ and γ -conversion contamination.

For the $\Lambda^0/\bar{\Lambda}^0$ analysis, the shape of the K_s^0 background depends strongly on momentum. Above a V^0 momentum of a few GeV/c, the $K_s^0 \rightarrow \pi^+\pi^-$ background is essentially uniform in the peak region of the $m_{p\pi}$ distribution and no cuts were made to remove the K_s^0 overlap. At sufficiently low momentum, the K_s^0 background becomes asymmetric under the $\Lambda^0/\bar{\Lambda}^0$ peak due to detector acceptance; the softer π fails to be reconstructed and thus the K_s^0 is not found. Therefore, $\Lambda^0/\bar{\Lambda}^0$ candidates with total momentum below 1.8 GeV/c were required to have $m_{\pi\pi}$ more than 3σ away from the K_s^0 mass, where σ is the measured resolution on $m_{\pi\pi}$, parameterized as $\sigma_{\pi\pi}(p) = 4.6 - 0.27p + 0.21p^2 - 0.01p^3$ MeV/c², and p is the V^0 momentum in GeV/c. In order to remove γ conversions, the proton helicity angle was required to satisfy $\cos\theta_p^* \geq -0.95$.

The $m_{\pi\pi}$ and $m_{p\pi}$ distributions for the remaining candidates are shown in figs. 5 and 6, respectively. The V^0 candidates were binned in x_p , and the resulting invariant mass

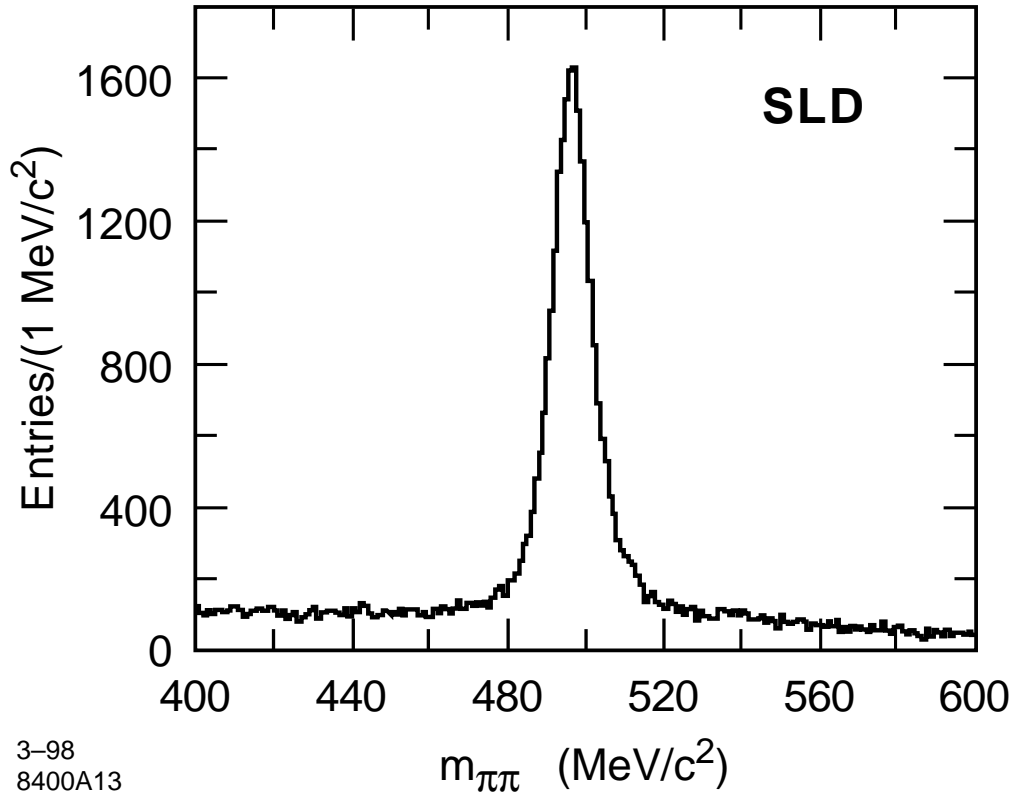


Figure 5: Invariant mass distribution for all $K_s^0 \rightarrow \pi^+\pi^-$ candidates.

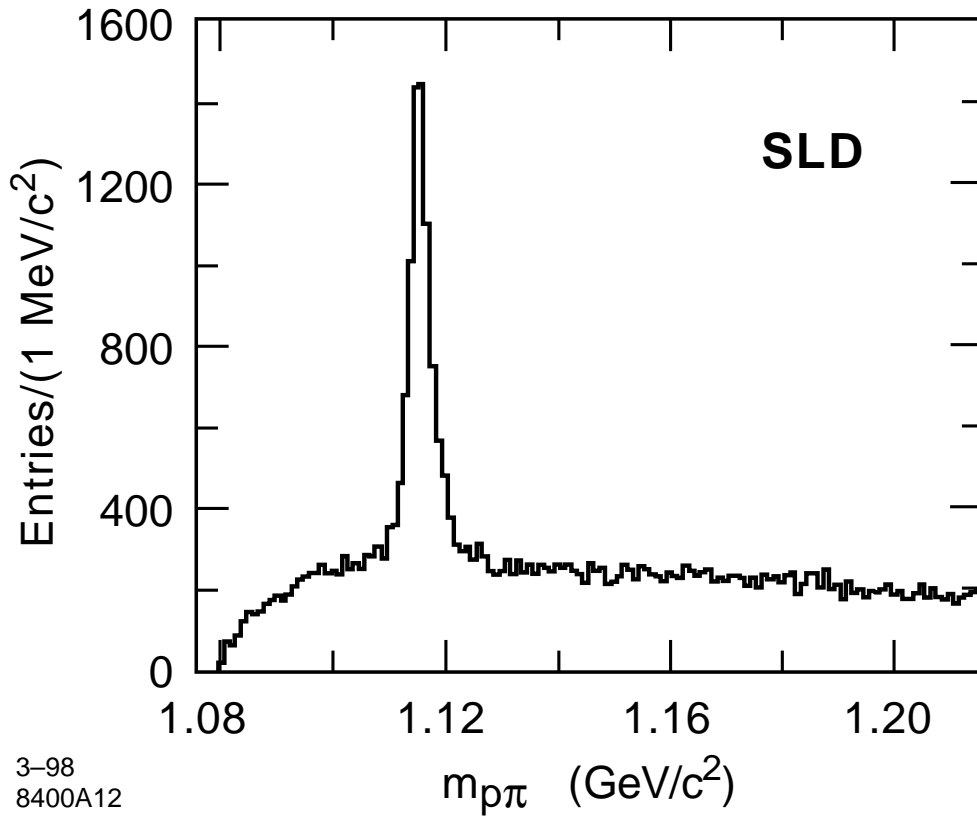


Figure 6: Invariant mass distribution for all $\Lambda^0 \rightarrow p\pi^-$ and $\bar{\Lambda}^0 \rightarrow \bar{p}\pi^+$ candidates.

distributions were fitted using a sum of signal and background functions. The function used for the signal peak was a Gaussian or a sum of two or three Gaussians of common center, depending on x_p . A single Gaussian was sufficient to describe the K_s^0 data in the lowest- x_p bin and the $\Lambda^0/\bar{\Lambda}^0$ data in the three lowest- x_p bins. However, the mass resolution is momentum-dependent and varies substantially over the width of a typical x_p bin; two Gaussians were sufficient in most cases, with three being needed for both the K_s^0 and $\Lambda^0/\bar{\Lambda}^0$ data in the highest- x_p bin. The relative fractions and nominal widths of the Gaussians in the sum were fixed from the MC simulation. The normalization, common center, and a resolution scale-factor were free parameters of the fit. The fitted centers were consistent with world average mass values [27], and the fitted scale factor was typically 1.1. The background shape used for the K_s^0 fits was a quadratic polynomial; for the $\Lambda^0/\bar{\Lambda}^0$ fits a more complicated function was required due to the proximity of the kinematic edge to the signal peak. The function $P_{bkg}(m) = a + b(m - m_\Lambda) + c(1 - e^{d((m-m_\Lambda)-0.038)})$ was found to be adequate in Monte Carlo studies, where a, b, c, d were free parameters.

The efficiencies for reconstructing true K_s^0 and $\Lambda^0/\bar{\Lambda}^0$ decays were calculated, using the simulation, by repeating the full selection and analysis on the simulated sample and dividing by the number of generated K_s^0 or $\Lambda^0/\bar{\Lambda}^0$. Several checks were performed to verify the MC simulation, and thus the V^0 reconstruction efficiency. In particular, the proper lifetimes of the K_s^0 and Λ^0 were measured, yielding values consistent with the respective world averages. The simulated reconstruction efficiencies are shown in fig. 7, and were parametrized as functions of x_p . The reconstruction efficiency is limited by the detector acceptance of ~ 0.67 and the charged decay branching fractions of 0.64 for $\Lambda^0/\bar{\Lambda}^0$ and 0.68 for K_s^0 . The efficiency at high momentum decreases due to finite detector size and two-track detector resolution, and the efficiency at low-momentum is limited by the minimum p_\perp and flight distance requirements. The discontinuity in the $\Lambda^0/\bar{\Lambda}^0$ reconstruction efficiency is due to the imposed K_s^0 mass cut for low- x_p candidates.

The differential cross section $1/N \, dn/dx_p$ per hadronic Z^0 decay was then calculated in each bin by dividing the integrated area under the fitted mass peak by the efficiency, the bin width and the number of observed hadronic events corrected for trigger and selection efficiency. As is conventional, the K^0/\bar{K}^0 cross section was obtained by multiplying the measured K_s^0 cross section by a factor of 2 to account for the undetected K_L^0 component. The resulting differential cross sections, including point-to-point systematic errors, discussed below, are shown in fig. 12 and listed in table 6.

Several sources of systematic uncertainty were investigated for the K_s^0 and $\Lambda^0/\bar{\Lambda}^0$ analysis. An important contribution to the overall V^0 spectrum is the track reconstruction efficiency of the detector, which was tuned using the world average measured charged multiplicity in hadronic Z^0 decays. We take the $\pm 1.7\%$ normalization uncertainty discussed above (sec. 4.1) as the uncertainty on our reconstruction efficiency, which corresponds to a normalization error on the K^0/\bar{K}^0 and $\Lambda^0/\bar{\Lambda}^0$ differential cross sections of 3.4%. This uncertainty is independent of momentum and is not shown in any of the figures or included in the errors listed in table 6. The momentum-dependent term discussed above and a conservative 50% variation of an ad hoc correction [26] to the simulated efficiency for V^0 s that decayed near the outer layers of the VXD were also included as systematic uncertainties due to detector modelling.

Each of the cuts used to select V^0 candidates was varied independently [26] and the

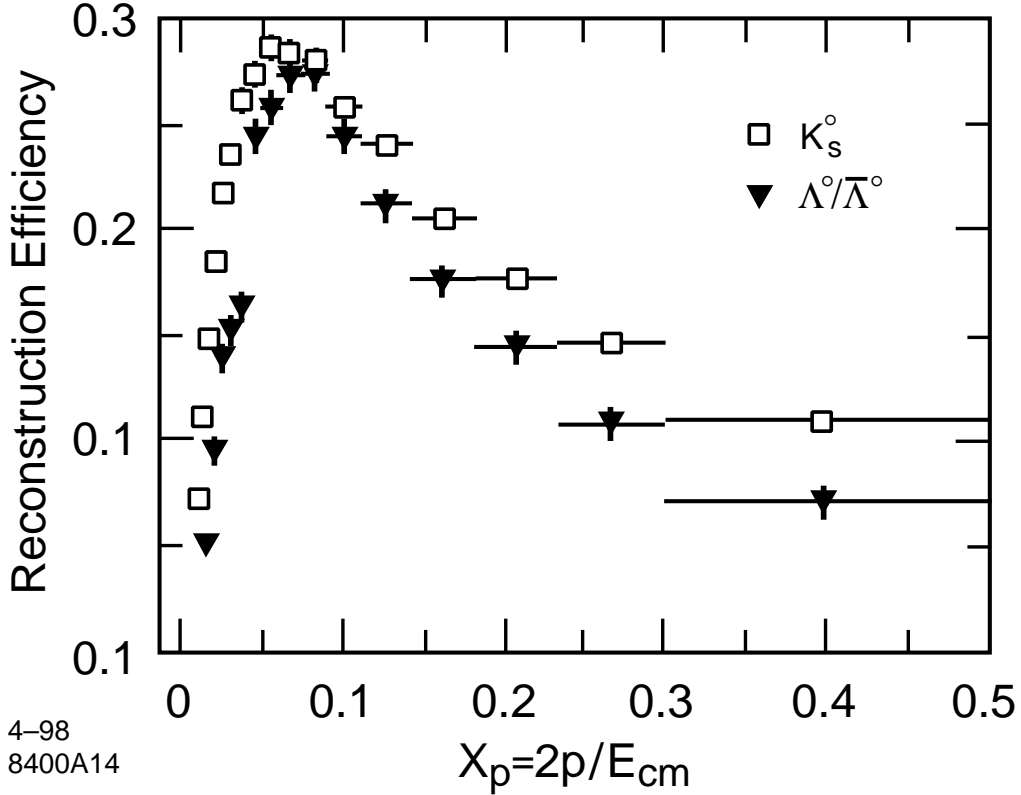


Figure 7: The simulated reconstruction efficiencies as a function of x_p for K_s^0 (squares) and $\Lambda^0/\bar{\Lambda}^0$ (triangles). The charged decay branching ratios are included in the efficiency. The discontinuity in the $\Lambda^0/\bar{\Lambda}^0$ reconstruction efficiency at $x_p = 0.04$ is due to the invariant-mass cut to remove the low-momentum K_s^0 background.

analysis repeated. For each bin the *rms* of this set of measurements was calculated and assigned as the systematic uncertainty due to modelling of the acceptance. For both the K^0/\bar{K}^0 and the $\Lambda^0/\bar{\Lambda}^0$ candidates, the signal and background shapes used in the fits were varied. Single and multiple independent Gaussians, without common centers or fixed widths, were used for the signal. Alternative background shapes included constants and polynomials of differing orders. In each case the fits were repeated on both data and simulated invariant mass distributions and the *rms* of the resulting differential cross sections was assigned as a systematic uncertainty. The MC statistical error on the calculated reconstruction efficiency was also assigned as a systematic error. These errors were added in quadrature to give the total systematic error.

4.3 Neutral K^{*0}/\bar{K}^{*0} and ϕ Production

We reconstructed the strange vector mesons ϕ and K^{*0}/\bar{K}^{*0} in the charged decay modes $\phi \rightarrow K^+K^-$ and $K^{*0}/\bar{K}^{*0} \rightarrow K^\pm\pi^\mp$ [28]. In order to ensure good invariant mass resolution, tracks were required to have at least 40 hits measured in the CDC, a track fit quality of $\chi^2/\text{dof} < 7$, and a polar angle satisfying $|\cos\theta| < 0.8$. Pairs of oppositely charged tracks satisfying these requirements were combined to form neutral candidates if a χ^2 fit of the two

Neutral V^0 Production				
x_p Range	$\langle x_p \rangle$	$1/N \, dn_{K^0}/dx_p$	$\langle x_p \rangle$	$1/N \, dn_{\Lambda^0}/dx_p$
0.009–0.011	0.010	$18.1 \pm 1.7 \pm 2.4$		
0.011–0.014	0.013	$19.1 \pm 1.2 \pm 1.1$		
0.014–0.018	0.016	$20.44 \pm 0.91 \pm 0.67$	0.015	$2.99 \pm 0.45 \pm 1.22$
0.018–0.022	0.020	$21.74 \pm 0.85 \pm 0.72$	0.020	$3.90 \pm 0.42 \pm 0.58$
0.022–0.027	0.025	$20.51 \pm 0.70 \pm 0.53$	0.025	$4.10 \pm 0.30 \pm 0.23$
0.027–0.033	0.030	$17.73 \pm 0.55 \pm 0.41$	0.030	$3.54 \pm 0.23 \pm 0.16$
0.033–0.041	0.037	$16.20 \pm 0.46 \pm 0.34$	0.037	$3.34 \pm 0.20 \pm 0.14$
0.041–0.050	0.045	$13.48 \pm 0.38 \pm 0.27$	0.045	$2.86 \pm 0.14 \pm 0.13$
0.050–0.061	0.055	$11.40 \pm 0.31 \pm 0.21$	0.055	$2.39 \pm 0.11 \pm 0.13$
0.061–0.074	0.067	$10.09 \pm 0.27 \pm 0.18$	0.067	$2.20 \pm 0.10 \pm 0.09$
0.074–0.091	0.082	$8.12 \pm 0.23 \pm 0.15$	0.082	$1.63 \pm 0.08 \pm 0.06$
0.091–0.111	0.100	$6.41 \pm 0.20 \pm 0.12$	0.100	$1.31 \pm 0.08 \pm 0.08$
0.111–0.142	0.126	$4.95 \pm 0.16 \pm 0.09$	0.125	$0.98 \pm 0.06 \pm 0.05$
0.142–0.183	0.161	$3.66 \pm 0.16 \pm 0.08$	0.160	$0.68 \pm 0.05 \pm 0.04$
0.183–0.235	0.206	$2.53 \pm 0.17 \pm 0.07$	0.205	$0.51 \pm 0.05 \pm 0.04$
0.235–0.301	0.262	$1.52 \pm 0.08 \pm 0.05$	0.262	$0.30 \pm 0.04 \pm 0.04$
0.301–0.497	0.371	$0.60 \pm 0.05 \pm 0.02$	0.368	$0.15 \pm 0.02 \pm 0.03$
Total Observed/Evt.		$1.90 \pm 0.02 \pm 0.07$		$0.37 \pm 0.01 \pm 0.02$

Table 6: Measured differential cross sections of neutral K^0/\bar{K}^0 -mesons and $\Lambda^0/\bar{\Lambda}^0$ -hyperons per hadronic Z^0 decay. A 3.4% normalization uncertainty is included in the systematic errors on the observed totals, but not in those on the cross sections.

tracks to a common vertex converged. The background from long-lived species was rejected by requiring the fitted vertex to be within 10 cm or $9\sigma_l$ of the IP in three dimensions, and within 4 cm or $6\sigma_l$ in the plane transverse to the beam direction. The background from γ -conversions was rejected by assigning the electron mass to both tracks and requiring m_{ee} to be greater than 70 MeV/c².

To reject the high combinatoric background from $\pi^+\pi^-$ pairs we used the CRID to identify charged kaon candidate tracks. Only liquid (gas) information was used for tracks with $p < 2.5$ (> 3.5) GeV/c, and liquid and gas information was combined for the remaining tracks. For this analysis a track was considered “identifiable” if it extrapolated through an active region of the appropriate CRID radiator(s); it was considered identified as a kaon if the log-likelihood difference between the kaon and pion hypotheses, $\mathcal{L}_K - \mathcal{L}_\pi$, exceeded 3. These cuts are considerably looser than those used in section 4.1, in order to maximize the acceptance for the neutral vector mesons. Efficiencies for identifying selected tracks as kaons by this definition were calibrated using the data in a manner similar to that described in section 2.2. The $K \rightarrow K$ efficiency was found to have a momentum dependence very

similar to the $\pi \rightarrow \pi$ efficiency shown in the upper left plot of fig. 3, with about 12% lower amplitude. There is no dip in the 5–10 GeV/c region since no cut was made against protons. The $\pi \rightarrow K$ misidentification rate averages 10% and is roughly independent of momentum; the $p \rightarrow K$ misidentification rate is substantial, especially in the 3–10 GeV/c region, but protons constitute only a small part of the combinatoric background.

A track pair was accepted as a $\phi \rightarrow K^+K^-$ candidate if both tracks were identified as kaons. A pair was accepted as a $K^{*0} \rightarrow K^+\pi^-$ candidate if one track was identified as a kaon and the other was not. Thus a track pair cannot be both a K^{*0}/\bar{K}^{*0} and ϕ candidate.

The ϕ candidates were binned in x_p , and the resulting m_{KK} distributions were fitted in a manner similar to that described above for the V^0 candidates. The signal shape was a sum of Gaussians of common center; the center was fixed at the world-average mass value [27], and the amplitude and a resolution scale factor were free parameters. A typical fitted scale factor was 1.08. The background shape was parametrized as a threshold term multiplied by a slowly decreasing exponential:

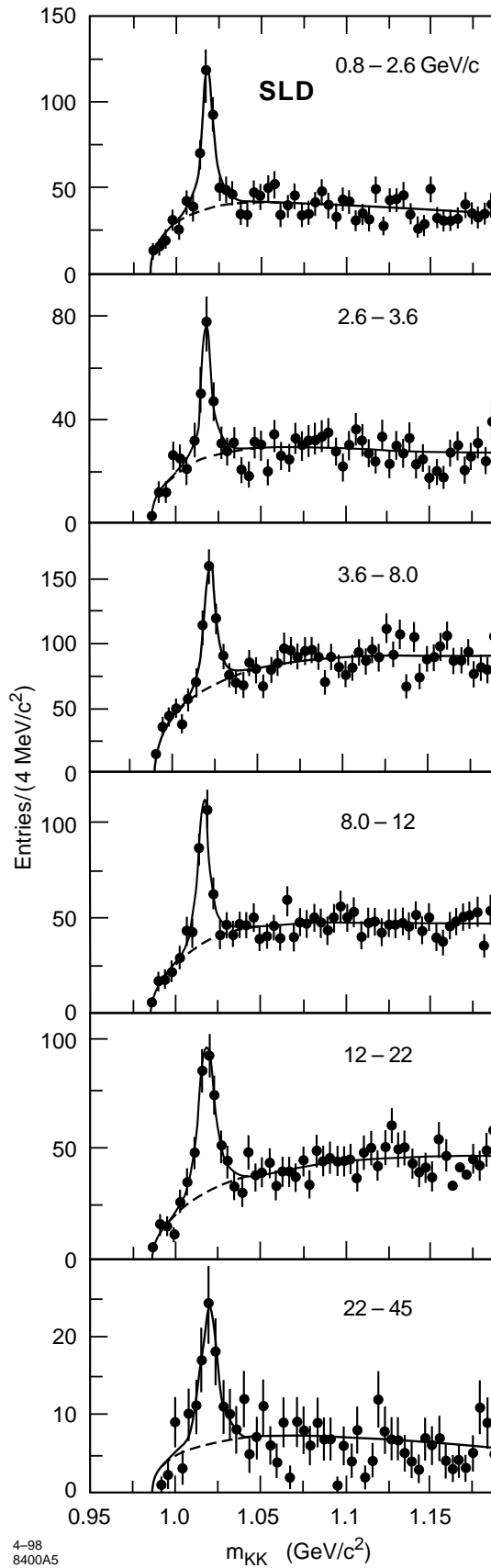
$$P_{bkg}(x) = Nx^\gamma e^{c_1x+c_2x^2+c_3x^3+c_4x^4+c_5x^5} \quad (1)$$

where $x = m_{KK} - 2m_K$, N is an overall normalization factor, and γ and $c_{1..5}$ are free parameters. Initial values of the background parameters were determined from fits to the m_{KK} distributions for simulated true combinatorial background and for same-sign track pairs in the data. The resulting parameters were consistent with each other and the functions described the shape of the distribution for candidates in the data in the region away from the signal peak. The measured m_{KK} distributions for the six x_p bins are shown in fig. 8, along with the results of the fits.

The case of the K^{*0}/\bar{K}^{*0} is considerably more complicated due to the natural width of the K^{*0} and the presence of many reflections of resonances decaying into $\pi^+\pi^-$ (π^0). The K^{*0}/\bar{K}^{*0} signal was parametrized using a relativistic Breit-Wigner with the amplitude free and the center and width fixed to world-average values [27]. The background was divided into combinatorial and resonant pieces. The combinatorial piece was described by a polynomial parametrization similar to that of the ϕ but with seven parameters. Parameter values derived from fits to simulated combinatorial background and a same-sign data test sample were found not to agree with each other or with the opposite-sign data away from the peak, and a search over a space of initial values was required in order to find the best fit.

Knowledge of the resonant contributions to the background is essential, since the K^{*0} is a wide state and non-monotonic background variation within its width can lead to systematic errors in the measured cross section. We considered four classes of reflections:

- $\rho^0 \rightarrow \pi^+\pi^-$, $K_s^0 \rightarrow \pi^+\pi^-$, and $\omega^0, \eta, \eta' \rightarrow N\pi$, where one of the charged pions is misidentified as a K^\pm . These backgrounds are large, even after reduction by a factor of about 5 by the particle identification. They are particularly important since the combination of ρ and ω decays gives rise to a dip in the total background near the center of the signal peak, and there is some uncertainty as to the shape of the ρ resonance in Z^0 decays (see ref. [29]).
- γ conversions where one electron is misidentified as a kaon. These are removed effectively by the m_{ee} cut against γ conversions noted above.



4-98
8400A5

Figure 8: Distributions of invariant mass m_{KK} for ϕ candidates in six momentum bins. The points with error bars represent the data. The solid curves represent the results of the fits described in the text; the dashed curves represent the fitted background component.

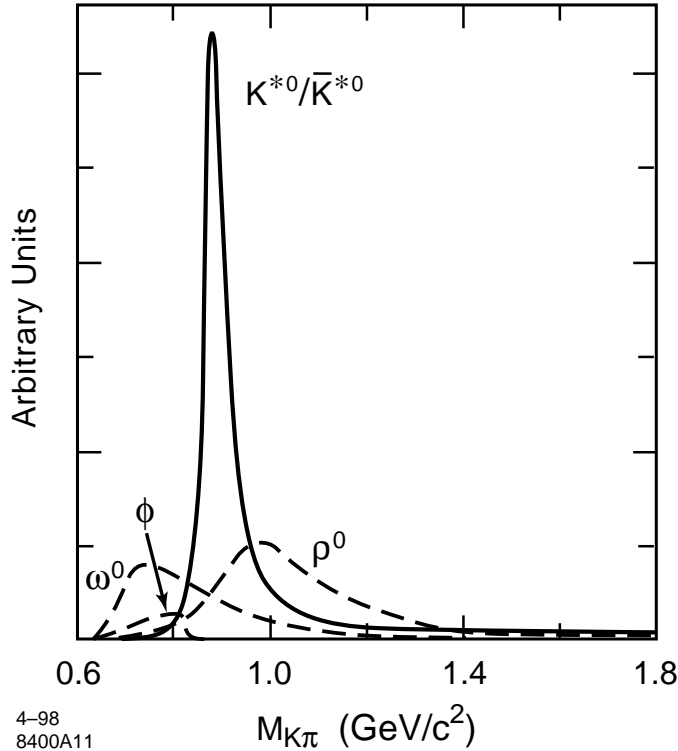


Figure 9: Simulated relative contributions of the K^{*0}/\bar{K}^{*0} signal (line) and of various resonant backgrounds (dashed lines) to the $m_{K\pi}$ distribution after all analysis cuts.

- $\phi \rightarrow K^+K^-$, where one track is identified as a kaon but the other is not. This background is reduced substantially by the requirement that only one of the tracks in the pair is identified as a kaon.
- $\Lambda^0 \rightarrow p\pi$, where the proton is misidentified as a kaon. These are removed effectively by the cut against long-lived species noted above. This and the last two categories give rise to a more pronounced shoulder in the background just below the signal peak, so their removal is quite useful in obtaining a robust fit.

The shape of the $m_{K\pi}$ distribution for each reflection was parametrized by a smooth function fitted to its simulated $m_{K\pi}$ distribution, and its total production cross section was set to the world average value [27] for Z^0 decays. Figure 9 shows the simulated relative contributions from the main resonant backgrounds along with the simulated signal, which was scaled to match our measured total cross section (see below). The set of reflection functions was added to the combinatorial function to give the total background function. A scale factor for each of the four categories of reflections was included as a free parameter in the fit to account for possible mismodelling of the misidentification rates; their fitted values were consistent with unity. Figure 10 shows the $m_{K\pi}$ distribution for each momentum bin, along with the results of the fits.

As for the K_s^0 and $\Lambda^0/\bar{\Lambda}^0$ analysis, the ϕ and K^{*0}/\bar{K}^{*0} reconstruction efficiencies were determined using the simulation, and are shown in fig. 11. Differential cross sections were calculated in the same way as for the K_s^0 and $\Lambda^0/\bar{\Lambda}^0$, and the results are shown in fig. 12 and listed in table 7.

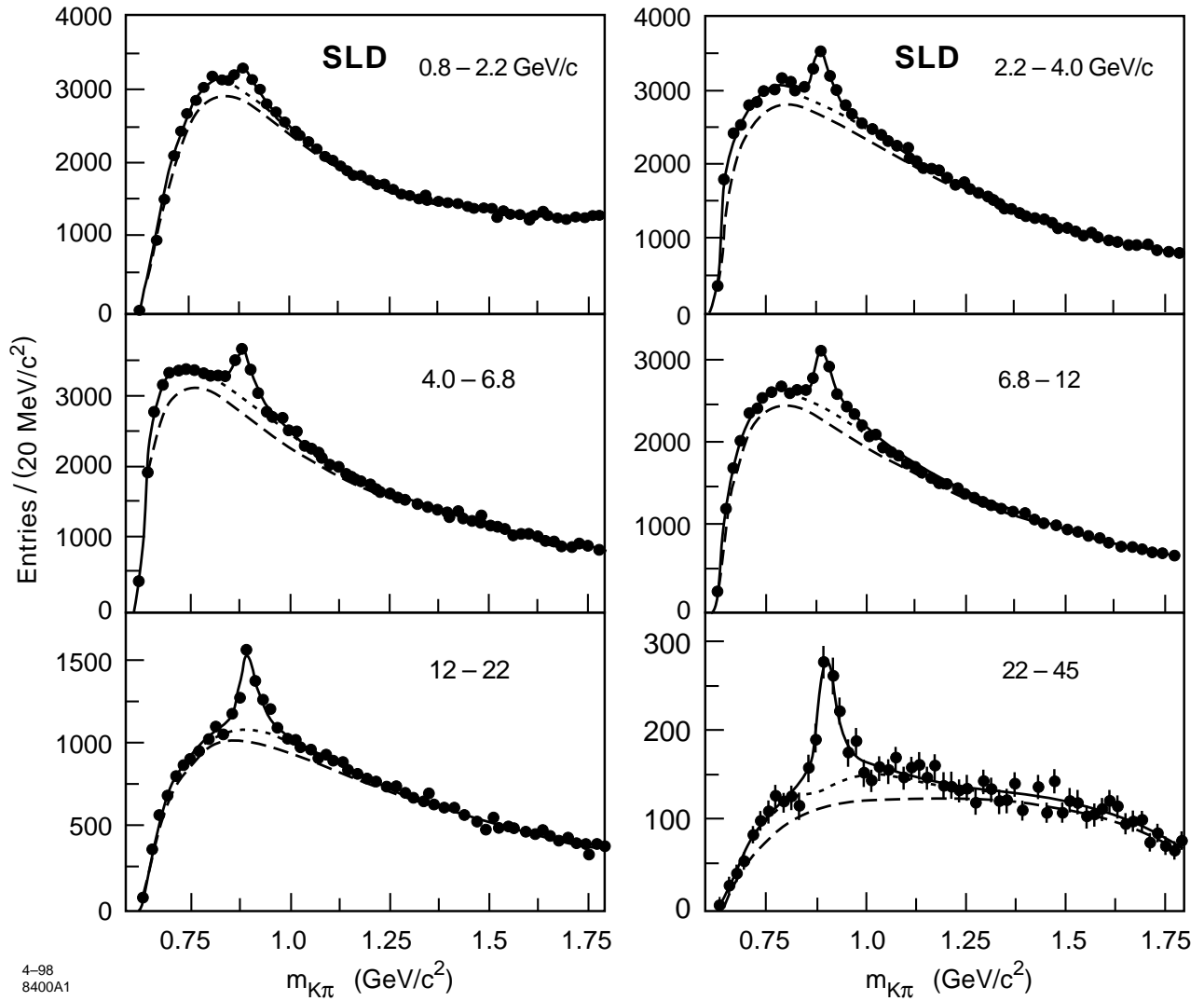


Figure 10: Distributions of invariant mass $m_{K\pi}$ for K^{*0}/\bar{K}^{*0} candidates in six momentum bins. The points represent the data. The solid curves represent the results of the fits described in the text; the dotted and dashed curves represent the fitted total background and combinatoric background components, respectively.

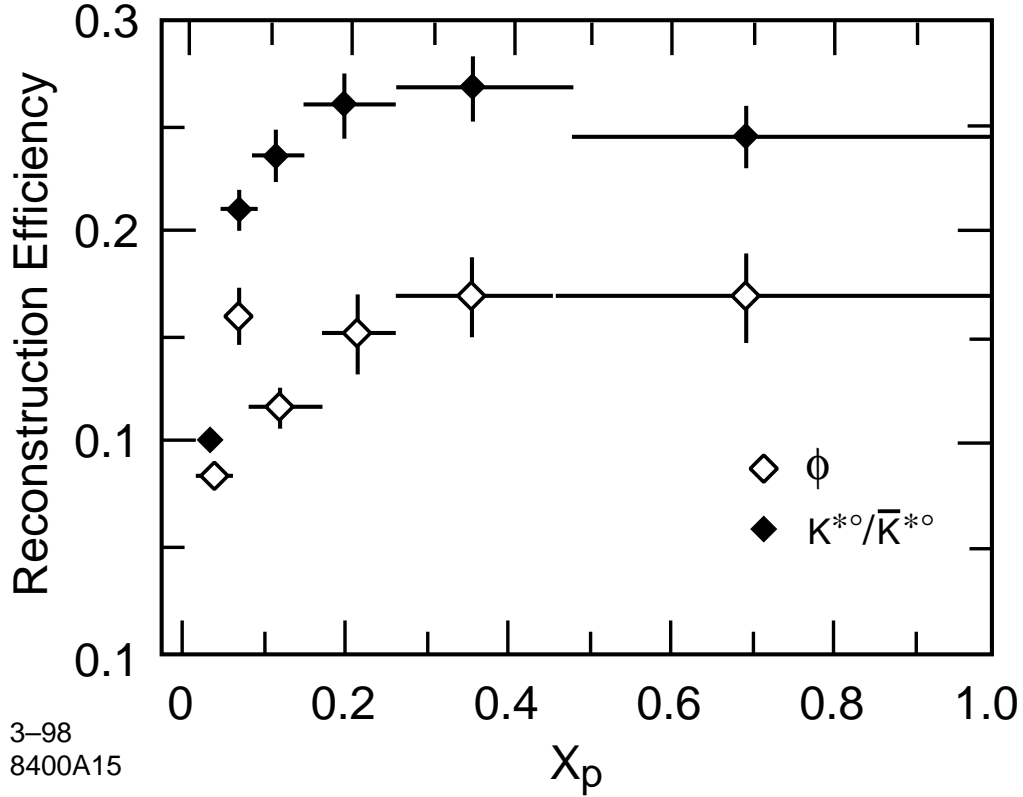


Figure 11: The simulated reconstruction efficiencies as a function of x_p for ϕ (open diamonds) and K^{*0}/\bar{K}^{*0} (diamonds). The charged decay branching ratios are included in the efficiency. The dip in the ϕ efficiency at $x_p \approx 0.13$ reflects the dip in the CRID K - π separation at $p \approx 2.5$ GeV/c (see fig. 3, upper left).

Neutral Strange Meson Production					
x_p Range	$\langle x_p \rangle$	$1/N \, dn_{K^{*0}}/dx_p$	x_p Range	$\langle x_p \rangle$	$1/N \, dn_{\phi}/dx_p$
0.018–0.048	0.033	$4.69 \pm 0.56 \pm 0.33$	0.018–0.057	0.037	$0.744 \pm 0.074 \pm 0.048$
0.048–0.088	0.068	$3.79 \pm 0.21 \pm 0.17$	0.057–0.079	0.068	$0.411 \pm 0.055 \pm 0.033$
0.088–0.149	0.118	$2.23 \pm 0.13 \pm 0.14$	0.079–0.175	0.127	$0.255 \pm 0.026 \pm 0.021$
0.149–0.263	0.206	$1.012 \pm 0.056 \pm 0.062$	0.175–0.263	0.215	$0.167 \pm 0.018 \pm 0.020$
0.263–0.483	0.342	$0.343 \pm 0.019 \pm 0.019$	0.263–0.483	0.357	$0.0739 \pm 0.0068 \pm 0.0085$
0.483–1.000	0.607	$0.051 \pm 0.004 \pm 0.004$	0.483–1.000	0.689	$0.0089 \pm 0.0015 \pm 0.0011$
Total Observed/Evt.		$0.647 \pm 0.022 \pm 0.029$			$0.0985 \pm 0.0046 \pm 0.0055$

Table 7: Measured differential cross sections of K^{*0}/\bar{K}^{*0} and ϕ mesons per hadronic Z^0 decay. A 3.4% normalization uncertainty is included in the systematic errors on the observed totals, but not in those on the cross sections.

Systematic uncertainties for this analysis were grouped into efficiency and fit-related categories. The dominant contributions to the efficiency category were the uncertainty in the track-finding efficiency (see above) and the uncertainty in kaon identification efficiency, for which the statistical error on the calibration from the data was used. The total uncertainties on the reconstruction efficiencies were 4–6% for K^{*0}/\bar{K}^{*0} and 6–11% for ϕ , depending on momentum.

In the case of the ϕ , fitting systematics were evaluated by varying the signal shape as in the V^0 analysis. In addition, fits were performed with the signal center shifted by plus and minus the error on the world-average mass value. The effect of background fluctuations was evaluated by taking the largest variation in the result over a set of fits done with the background shape parameters c_i fixed to all combinations of their fitted values $\pm 1\sigma$. The total fitting uncertainties were 2–8%.

In the case of the K^{*0}/\bar{K}^{*0} , we considered the same variations, as well as variation of the signal width by $\pm 1\sigma$ from the world-average value and several variations of the resonant background. Fits were performed with the misidentification scale factors fixed to their fitted values $\pm 50\%$ for the $\pi\pi$ category and $\pm 15\%$ for the others, corresponding to roughly twice the error on our measured misidentification rates. All 16 combinations were considered, and the largest variation taken as a systematic error. The cross section for production of each resonance was varied by the error on the world-average value. The sizes of the ρ and ω contributions were varied in all four combinations of $\pm 30\%$ and $\pm 10\%$, respectively, and the largest variation was taken as a systematic error. Following [29] an error due to the uncertainty in the ρ^0 lineshape was evaluated by shifting the ρ reflection function down by 40 MeV/c². The total fitting uncertainties were 2–6%.

4.4 Hadron Production in Inclusive Hadronic Z^0 Decays

Our measured differential cross sections per hadronic event of the seven hadron species are shown as a function of x_p in fig. 12, along with that of inclusive charged particles. At low x_p pions are seen to dominate the hadrons produced in hadronic Z^0 decays. For example, at $x_p \approx 0.03$, pseudoscalar K^\pm and K^0/\bar{K}^0 are produced at a rate about ten times lower than pions, vector K^{*0} are suppressed by an additional factor of ~ 4 , and the doubly strange vector ϕ by another factor of ~ 12 . The most commonly produced baryons, protons, are suppressed by a factor of ~ 25 relative to pions, and the strange baryon $\Lambda^0/\bar{\Lambda}^0$ by an additional factor of ~ 3 .

These results are in general consistent with previous measurements from experiments at LEP [7], provided that the point-to-point correlations in the systematic errors are taken into account. However, although our proton differential cross section for $x_p > 0.35$ is consistent with that measured by ALEPH [24], it is not consistent with that measured by OPAL [23].

We compared our results with the predictions of the JETSET 7.4, UCLA 4.1 and HERWIG 5.8 event generators described in section 1, using in all cases the default parameters. Figures 13 and 14 show the charged fractions and the neutral differential cross sections, respectively, along with the predictions of these three models. The momentum dependence for each of the seven hadron species is reproduced qualitatively by all models. For momenta below about 1.5 GeV/c, all models overestimate the kaon fraction significantly and all except UCLA underestimate the pion fraction by about 2σ (taking into account the correlation

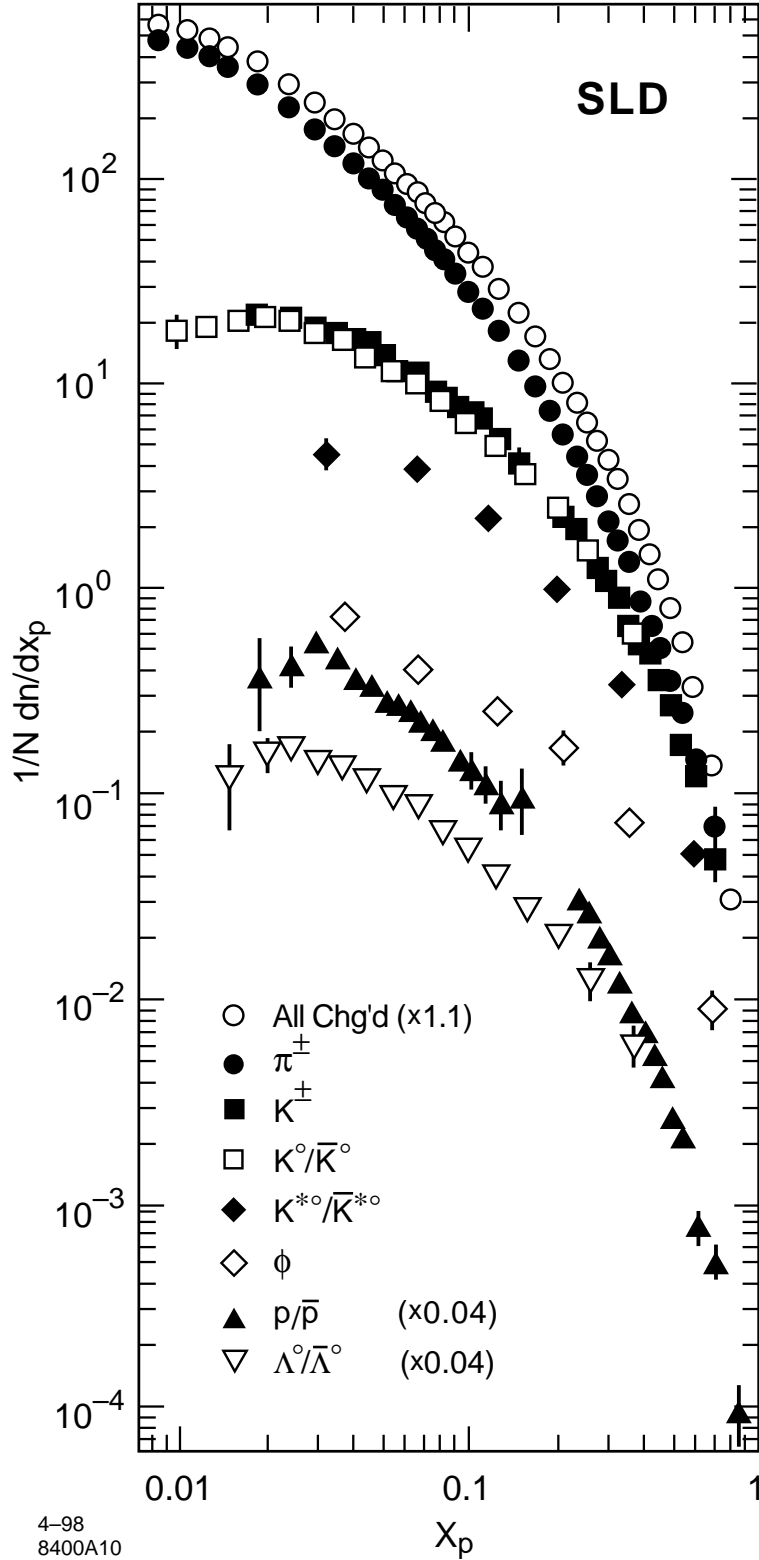


Figure 12: Differential cross sections per hadronic Z^0 decay per unit x_p for inclusive charged particles (open circles), π^\pm (circles), K^\pm (squares), K^0/\bar{K}^0 (open squares), K^{*0}/\bar{K}^{*0} (diamonds), ϕ (open diamonds), p/\bar{p} (triangles), and $\Lambda^0/\bar{\Lambda}^0$ (open triangles). The baryon and all-charged differential cross sections have been scaled by 0.04 and 1.1, respectively, for clarity. The error bars represent statistical and systematic errors added in quadrature. Each point is plotted at the average x_p value of reconstructed particles in that bin (see tables 2–7).

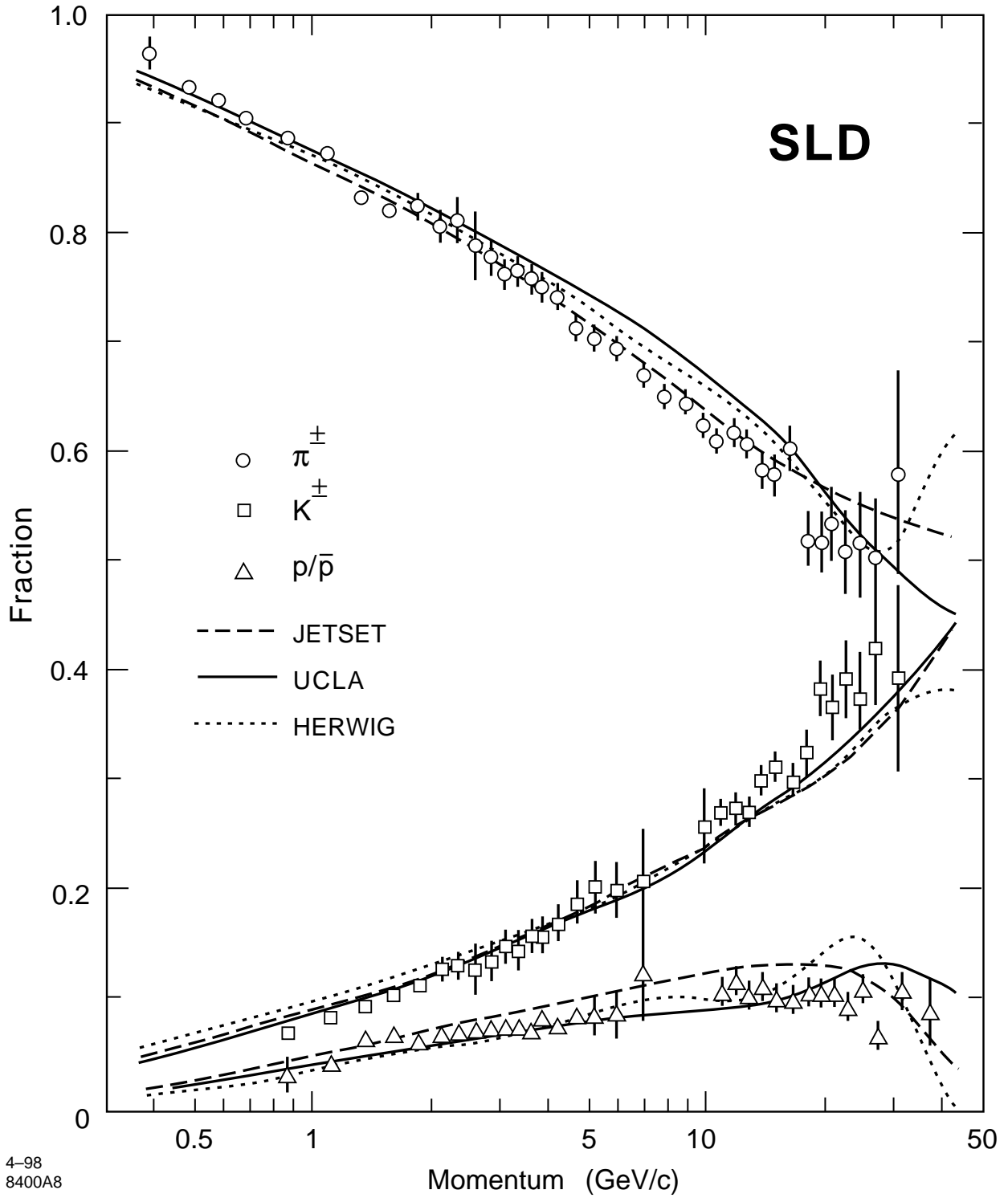


Figure 13: Comparison of our measured charged hadron fractions (symbols) with the predictions of the JETSET (dashed lines), UCLA (solid lines) and HERWIG (dotted lines) fragmentation models.

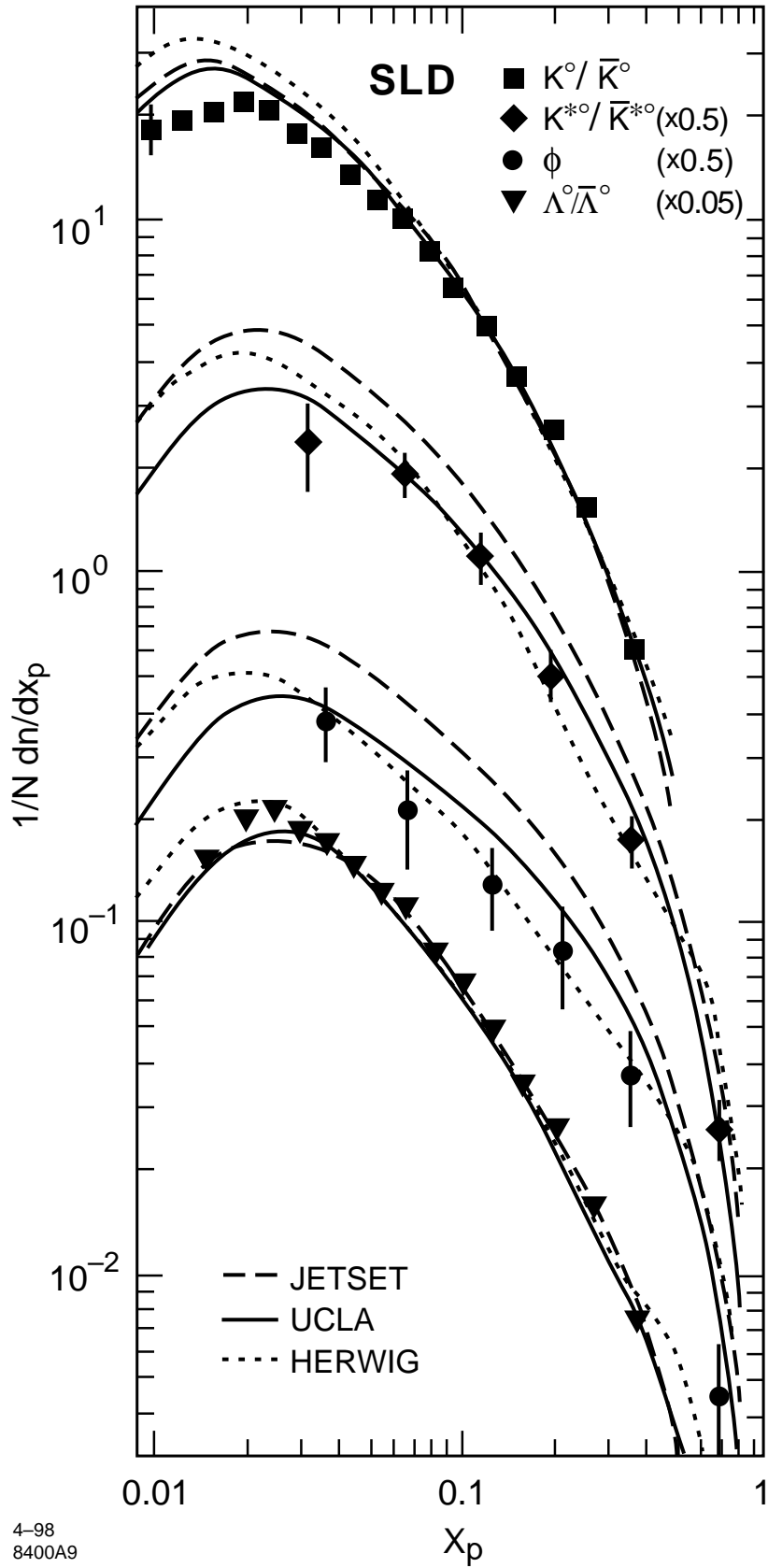


Figure 14: Comparison of our measured neutral hadron differential cross sections with the predictions of three fragmentation models.

in the experimental errors). In the 5–10 GeV/c range UCLA and HERWIG overestimate the pion fraction by 2–3 σ . For $p > 10$ GeV/c, JETSET overestimates the proton fraction, but describes the momentum dependence. In this momentum region, HERWIG and UCLA predict a momentum dependence in the proton fraction that is inconsistent with the data.

In the case of K^0/\bar{K}^0 , all models describe the data well at high x_p , but overestimate the cross section at low x_p by as much as 50%. A similar excess was seen in the charged kaon fraction (see fig 13). In the case of $\Lambda^0/\bar{\Lambda}^0$, JETSET and UCLA describe the data well except for a 10% shortfall near $x_p = 0.02$. HERWIG describes the data well except for the lowest and highest x_p points, where it overestimates the production. The structure in the HERWIG prediction at very high x_p is similar to that seen in the proton fraction, and is also visible to varying degrees in the predictions for the neutral strange mesons. In the case of K^{*0}/\bar{K}^{*0} , JETSET is high by a roughly constant factor of 1.5 across the x_p range; HERWIG and UCLA reproduce the data except at the lowest x_p point. In the case of ϕ , JETSET is high by a factor of two over all x_p , UCLA is high for $x_p > 0.06$, and HERWIG describes the data except at the highest x_p point.

5 Flavor-Dependent Analysis

The analyses described above were repeated on the light-, c - and b -tagged event samples described in section 3, to yield differential cross sections R_h^{ktag} for each hadron species h in each tagged sample. True differential cross sections R_h^m in events of the three flavor types, $k, m = l, c, b$, representing events of the types $Z^0 \rightarrow u\bar{u}, d\bar{d}, s\bar{s}$, $Z^0 \rightarrow c\bar{c}$, and $Z^0 \rightarrow b\bar{b}$, respectively, were extracted by solving for each species h the relations:

$$R_h^{ktag} = \frac{\sum_m B_{mk}^h \epsilon_{mk} F_m R_h^m}{\sum_m \epsilon_{mk} F_m}. \quad (2)$$

Here, F_m is the fraction of hadronic Z^0 decays of flavor type m , taken from the Standard Model, ϵ_{mk} is the event tagging efficiency matrix (see table 1), and B_{mk}^h represents the momentum-dependent bias of tag k toward selecting events of flavor m that contain hadrons of species h . Ideally all biases would be unity in this formulation. The biases were calculated from the MC simulation as $B_{mk}^h = (n_{m,ktag}^h / N_{m,ktag}) / (n_m^h / N_m)$, where N_m (n_m^h) is the number of simulated events (hadrons of species h in events) of true flavor m and $N_{m,ktag}$ ($n_{m,ktag}^h$) is the number of (h -hadrons in) those events that are tagged as flavor k . The diagonal bias values [20, 26, 28] are within a few percent of unity for the charged hadrons, ϕ and K^{*0} , reflecting a small multiplicity dependence of the flavor tags. They deviate by as much as 10% from unity for the K^0/\bar{K}^0 and $\Lambda^0/\bar{\Lambda}^0$, since some tracks from V^0 decays are included in the tagging track sample and have large impact parameter. The off-diagonal bias values deviate from unity by a larger amount, but these have little effect on the unfolded results.

The resulting differential cross sections are listed in tables 8–14. The systematic errors listed are only those relevant for the comparison of different flavors, namely those due to uncertainties in the unfolding procedure; the systematic errors given in the preceding section are also applicable, but are common to all three flavor categories. The flavor unfolding systematic errors were evaluated by varying each element of the event tagging efficiency matrix ϵ_{ii} by ± 0.01 [30], varying the heavy quark production fractions R_b and R_c by the errors

x_p Range	$\langle x_p \rangle$	π^\pm Production Cross Sections			Ratios	
		$u\bar{u}, d\bar{d}, s\bar{s}$	$c\bar{c}$	$b\bar{b}$	$c:uds$	$b:uds$
0.008–0.010	0.009	467.2±9.0	493.±37.	508.1±10.6	1.05±0.09	1.09±0.03
0.010–0.012	0.011	428.1±8.2	413.±34.	481.2±9.7	0.96±0.09	1.12±0.03
0.012–0.014	0.013	383.2±7.3	403.±30.	441.3±8.6	1.05±0.09	1.15±0.03
0.014–0.016	0.015	337.1±6.6	375.±27.	388.4±7.9	1.11±0.09	1.15±0.03
0.016–0.022	0.019	274.7±4.6	301.±19.	333.6±4.8	1.10±0.08	1.21±0.02
0.022–0.027	0.025	214.5±3.7	230.±15.	264.4±4.1	1.07±0.08	1.23±0.03
0.027–0.033	0.030	165.5±3.1	178.±13.	205.4±3.6	1.08±0.09	1.24±0.03
0.033–0.038	0.036	137.2±2.7	141.±11.	166.9±3.3	1.03±0.09	1.22±0.03
0.038–0.044	0.041	117.2±2.5	111.±10.	141.4±3.2	0.95±0.10	1.21±0.04
0.044–0.049	0.047	98.4±2.4	96.±10.	118.6±3.3	0.97±0.11	1.20±0.04
0.049–0.055	0.052	83.6±2.4	86.±10.	106.3±3.5	1.03±0.13	1.27±0.06
0.055–0.066	0.060	66.9±1.4	65.8±5.9	84.2±2.0	0.98±0.10	1.26±0.04
0.066–0.077	0.071	52.8±1.1	48.8±4.8	64.0±1.6	0.93±0.10	1.21±0.04
0.077–0.088	0.082	41.61±0.95	43.4±4.0	49.2±1.4	1.04±0.11	1.18±0.04
0.088–0.099	0.093	34.11±0.81	32.3±3.5	40.6±1.2	0.95±0.11	1.19±0.04
0.099–0.110	0.104	28.74±0.72	23.6±3.1	30.1±1.1	0.82±0.11	1.05±0.04
0.110–0.132	0.120	21.64±0.46	21.3±2.1	22.72±0.76	0.99±0.10	1.05±0.04
0.132–0.164	0.147	15.26±0.31	12.4±1.4	13.54±0.51	0.81±0.10	0.89±0.04
0.164–0.186	0.175	10.76±0.26	8.8±1.1	8.26±0.42	0.82±0.11	0.77±0.04
0.186–0.208	0.197	8.44±0.22	6.66±0.90	5.57±0.34	0.79±0.11	0.66±0.04
0.208–0.230	0.219	6.29±0.19	6.03±0.77	3.93±0.29	0.96±0.13	0.62±0.05
0.230–0.274	0.251	4.81±0.12	3.77±0.48	2.52±0.18	0.78±0.11	0.52±0.04
0.274–0.318	0.294	2.932±0.090	2.62±0.36	1.39±0.13	0.89±0.13	0.47±0.05
0.318–0.384	0.348	1.815±0.059	1.69±0.23	0.695±0.084	0.93±0.14	0.38±0.05
0.384–0.471	0.421	0.915±0.037	0.42±0.14	0.380±0.053	0.46±0.16	0.42±0.06
0.471–0.603	0.529	0.376±0.023	0.146±0.084	0.108±0.031	0.39±0.22	0.29±0.08
0.603–0.768	0.654	0.145±0.017	0.027±0.054	0.006±0.015	0.18±0.37	0.04±0.10

Table 8: Measured differential cross sections $(1/N)dn_{\pi^\pm}/dx_p$ for the production of charged pions per Z^0 decay into light (u, d, s), c and b primary flavors. The errors are the sum in quadrature of statistical errors and those systematic uncertainties arising from the unfolding procedure. Systematic errors common to the three flavors are not included. The $\langle x_p \rangle$ values for the three flavor samples are consistent in each bin, and have been averaged.

x_p Range	$\langle x_p \rangle$	K^\pm Production Cross Sections			Ratios	
		$u\bar{u}, d\bar{d}, s\bar{s}$	$c\bar{c}$	$b\bar{b}$	$c:uds$	$b:uds$
0.016–0.022	0.019	22.6±1.2	19.5±5.0	24.3±1.7		1.08±0.09
0.022–0.027	0.025	19.2±1.1	26.8±4.7	22.3±1.6	1.11±0.18	1.16±0.11
0.027–0.033	0.030	18.6±1.1	16.4±4.4	22.3±1.6		1.20±0.11
0.033–0.038	0.036	17.0±1.0	14.9±4.4	22.8±1.6	0.88±0.19	1.34±0.12
0.038–0.044	0.041	14.6±1.1	18.5±4.5	19.7±1.6		1.35±0.15
0.044–0.049	0.047	15.3±1.2	13.6±4.9	19.9±1.8	1.08±0.24	1.30±0.15
0.049–0.055	0.052	14.5±1.3	6.1±5.2	18.3±1.9		1.26±0.17
0.055–0.066	0.060	10.29±0.85	10.7±3.6	15.2±1.4	0.78±0.26	1.48±0.18
0.066–0.077	0.071	9.00±0.73	9.5±3.1	14.5±1.2		1.61±0.19
0.077–0.088	0.082	7.38±0.70	8.9±3.0	13.4±1.2	1.13±0.28	1.82±0.23
0.088–0.099	0.093	6.12±0.70	10.5±3.0	10.6±1.1		1.73±0.27
0.099–0.110	0.104	6.00±0.75	10.2±3.2	8.4±1.2	1.72±0.40	1.40±0.26
0.110–0.132	0.120	4.78±0.57	8.1±2.5	8.71±0.98		1.82±0.30
0.132–0.164	0.147	3.30±0.61	8.0±2.6	3.65±0.94	2.06±0.54	1.11±0.35
0.208–0.230	0.219	2.29±0.17	2.64±0.70	2.01±0.27	1.16±0.32	0.88±0.13
0.230–0.274	0.251	1.498±0.089	3.29±0.37	1.18±0.14		0.79±0.10
0.274–0.318	0.294	1.272±0.068	1.30±0.27	0.811±0.098	1.66±0.19	0.64±0.08
0.318–0.384	0.348	0.925±0.046	0.66±0.17	0.496±0.060		0.54±0.07
0.384–0.471	0.421	0.548±0.032	0.65±0.12	0.113±0.035	0.92±0.15	0.21±0.06
0.471–0.603	0.529	0.266±0.020	0.229±0.073	0.043±0.021		0.16±0.08
0.603–0.768	0.654	0.101±0.015	-0.003±0.046	0.020±0.014	0.57±0.24	0.20±0.14

Table 9: Differential cross sections for the production of K^\pm mesons per Z^0 decay into light, c and b primary flavors.

x_p Range	$\langle x_p \rangle$	K^{*0}/\bar{K}^{*0} Production Cross Sections			Ratios	
		$u\bar{u}, d\bar{d}, s\bar{s}$	$c\bar{c}$	$b\bar{b}$	$c:uds$	$b:uds$
0.018–0.048	0.033	5.2±1.3	7.8±5.6	1.3±2.1	1.51±1.15	0.25±0.41
0.048–0.088	0.068	4.28±0.52	1.0±2.6	4.53±0.83	0.23±0.60	1.06±0.23
0.088–0.149	0.118	2.14±0.29	0.5±1.6	3.64±0.47	0.23±0.73	1.70±0.31
0.149–0.263	0.206	0.81±0.12	1.10±0.59	1.43±0.24	1.35±0.76	1.75±0.40
0.263–0.483	0.342	0.345±0.042	0.29±0.20	0.400±0.078	0.85±0.58	1.16±0.27
0.483–1.000	0.607	0.076±0.010	0.026±0.034	0.012±0.009	0.36±0.45	0.15±0.11

Table 10: Differential cross sections for the production of K^{*0}/\bar{K}^{*0} mesons per Z^0 decay into light, c and b primary flavors.

x_p Range	$\langle x_p \rangle$	p/ \bar{p} Production Cross Sections			Ratios	
		$u\bar{u}, d\bar{d}, s\bar{s}$	$c\bar{c}$	$b\bar{b}$	$c:uds$	$b:uds$
0.016–0.022	0.019	8.55±1.31	17.6±5.5	6.3±1.8		0.74±0.24
0.022–0.027	0.025	10.88±0.96	12.9±4.0	9.0±1.3	1.57±0.38	0.83±0.14
0.027–0.033	0.030	12.52±0.87	15.2±3.7	14.9±1.3		1.19±0.13
0.033–0.038	0.036	11.22±0.79	13.6±3.3	10.6±1.1	1.21±0.23	0.94±0.12
0.038–0.044	0.041	8.65±0.73	10.7±3.1	8.7±1.1		1.00±0.15
0.044–0.049	0.047	8.87±0.72	8.0±3.0	7.9±1.02	1.07±0.26	0.89±0.13
0.049–0.055	0.052	6.16±0.65	10.8±2.8	5.48±0.92		0.89±0.18
0.055–0.066	0.060	7.09±0.50	5.1±2.1	5.97±0.75	1.04±0.27	0.84±0.12
0.066–0.077	0.071	4.91±0.49	7.7±2.2	4.60±0.74		0.94±0.18
0.077–0.088	0.082	4.71±0.49	3.6±2.1	4.37±0.76	1.18±0.34	0.93±0.19
0.088–0.099	0.093	3.43±0.51	4.2±2.2	3.49±0.80		1.02±0.28
0.099–0.110	0.104	2.72±0.58	6.2±2.6	2.99±0.88	1.72±0.61	1.10±0.40
0.110–0.132	0.120	2.98±0.46	0.9±1.9	1.77±0.68		0.59±0.25
0.132–0.164	0.147	3.16±0.59	−0.2±2.5	2.93±0.86	0.07±0.54	0.93±0.32
0.230–0.274	0.251	0.738±0.085	0.84±0.34	0.506±0.098		0.69±0.15
0.274–0.318	0.294	0.514±0.062	0.46±0.24	0.241±0.065	1.04±0.35	0.47±0.14
0.318–0.384	0.348	0.338±0.037	0.16±0.14	0.093±0.034		0.27±0.10
0.384–0.471	0.421	0.141±0.021	0.277±0.079	0.012±0.016	1.02±0.35	0.09±0.12
0.471–0.603	0.529	0.088±0.010	0.040±0.034	−0.002±0.006		−.02±0.07
0.603–0.768	0.654	0.020±0.004	0.004±0.014	0.001±0.003	0.40±0.35	0.04±0.13

Table 11: Differential cross sections for the production of p/ \bar{p} per Z^0 decay into light, c and b primary flavors.

x_p Range	$\langle x_p \rangle$	$\Lambda^0/\bar{\Lambda}^0$ Production Cross Sections			Ratios	
		$u\bar{u}, d\bar{d}, s\bar{s}$	$c\bar{c}$	$b\bar{b}$	$c:uds$	$b:uds$
0.011–0.020	0.016	4.72±0.87	1.5±3.3	2.8±1.2	0.32±0.70	0.59±0.27
0.020–0.030	0.025	3.87±0.49	2.5±2.0	4.19±0.79	0.66±0.53	1.08±0.24
0.030–0.045	0.038	3.41±0.35	4.5±1.5	2.39±0.50	1.32±0.46	0.70±0.16
0.045–0.067	0.056	2.21±0.22	3.56±0.97	2.47±0.34	1.61±0.46	1.12±0.19
0.067–0.100	0.082	1.14±0.16	2.89±0.72	1.44±0.25	2.11±0.58	1.05±0.22
0.100–0.150	0.122	1.15±0.13	0.54±0.54	1.10±0.17	0.47±0.48	0.96±0.18
0.150–0.247	0.189	0.52±0.08	0.56±0.32	0.60±0.09	1.08±0.64	1.15±0.25
0.247–0.497	0.319	0.24±0.05	−0.13±0.19	0.20±0.04	−0.54±0.81	0.83±0.25

Table 12: Differential cross sections for the production of $\Lambda^0/\bar{\Lambda}^0$ per Z^0 decay into light, c and b primary flavors.

x_p Range	$\langle x_p \rangle$	K^0/\bar{K}^0 Production Cross Sections			Ratios	
		$u\bar{u}, d\bar{d}, s\bar{s}$	$c\bar{c}$	$b\bar{b}$	$c:uds$	$b:uds$
0.009–0.011	0.010	19.0±4.4	6.±19.	6.1±3.1	0.29±0.99	0.32±0.17
0.011–0.011	0.013	23.2±3.2	−3.±15.	23.1±5.6	−0.14±0.64	0.99±0.39
0.014–0.018	0.016	20.4±2.4	15.±10.	25.8±4.4	0.72±0.52	1.27±0.25
0.018–0.022	0.020	21.2±2.3	22.7±9.7	21.7±3.3	1.07±0.47	1.02±0.18
0.022–0.027	0.025	20.5±1.8	17.4±7.8	21.4±2.6	0.85±0.39	1.04±0.15
0.027–0.033	0.030	17.3±1.4	12.8±6.2	20.7±2.2	0.74±0.36	1.20±0.15
0.033–0.041	0.037	14.1±1.2	12.8±5.1	19.3±1.9	0.91±0.37	1.37±0.17
0.041–0.050	0.045	12.0±1.0	13.2±4.4	15.6±1.5	1.10±0.38	1.30±0.16
0.050–0.061	0.055	10.1±0.8	10.9±3.5	13.2±1.2	1.08±0.36	1.31±0.15
0.061–0.074	0.067	7.73±0.69	12.8±3.2	13.5±1.1	1.66±0.43	1.75±0.20
0.074–0.091	0.082	7.07±0.52	3.0±2.4	12.3±0.9	0.42±0.33	1.74±0.17
0.091–0.111	0.100	5.33±0.44	7.0±2.0	8.35±0.81	1.31±0.39	1.57±0.19
0.111–0.142	0.126	4.17±0.34	4.6±1.5	5.85±0.57	1.10±0.37	1.40±0.17
0.142–0.183	0.161	3.17±0.30	3.7±1.6	4.26±0.55	1.18±0.53	1.35±0.21
0.183–0.235	0.206	2.16±0.22	2.68±0.97	1.99±0.48	1.24±0.46	0.92±0.24
0.235–0.301	0.262	1.12±0.16	2.62±0.72	0.09±0.24	2.15±0.66	0.71±0.22
0.301–0.497	0.371	0.69±0.10	0.79±0.45	0.10±0.10	1.44±0.70	0.14±0.14

Table 13: Differential cross sections for the production of K^0/\bar{K}^0 mesons per Z^0 decay into light, c and b primary flavors.

x_p Range	$\langle x_p \rangle$	ϕ Production Cross Sections			Ratios	
		$u\bar{u}, d\bar{d}, s\bar{s}$	$c\bar{c}$	$b\bar{b}$	$c:uds$	$b:uds$
0.018–0.057	0.037	0.64±0.18	1.08±0.77	0.73±0.28	1.67±1.28	1.13±0.53
0.057–0.079	0.068	0.48±0.18	0.31±1.02	0.37±0.31	0.64±2.15	0.78±0.70
0.079–0.175	0.127	0.222±0.073	0.12±0.39	0.42±0.11	0.56±1.75	1.88±0.81
0.175–0.263	0.215	0.091±0.052	0.35±0.23	0.228±0.068	3.85±3.32	2.51±1.61
0.263–0.483	0.357	0.052±0.021	0.185±0.085	0.054±0.023	3.58±2.17	1.05±0.61
0.483–1.000	0.689	0.017±0.004	−0.016±0.013	0.007±0.004	−0.96±0.78	0.43±0.27

Table 14: Differential cross sections for the production of ϕ mesons per Z^0 decay into light, c and b primary flavors.

on their respective world averages, and varying each diagonal bias value B_{ii}^h by the larger of ± 0.005 and $\pm 20\%$ of its difference from unity. Since the lepton background is strongly flavor-dependent, the photon conversion rate in the simulation was varied by $\pm 15\%$, and the simulated rates of lepton production from other sources in light-, c , and b -flavor events were varied by $\pm 50\%$, $\pm 10\%$ and $\pm 5\%$, respectively. The unfolding systematic errors are typically small compared with the statistical errors, and are dominated by the variation in the bias.

In figure 15 we show the differential cross sections for the seven hadron species in light-flavor Z^0 decays. Qualitatively these are similar to those in flavor-inclusive decays (fig. 12), although all differential cross sections are larger at high x_p in light flavor events. The same general features of π - K and p - Λ^0 convergence at high x_p are visible, and the relative suppressions of hadron species with respect to one another are similar in magnitude and momentum dependence.

Also shown in fig. 15 are the predictions of the three simulation programs. All models reproduce the shape of each differential cross section qualitatively. The JETSET prediction for charged pions is smaller than the data in the range $x_p < 0.015$, and those for the pseudoscalar kaons are larger than the data for $0.015 < x_p < 0.03$; those for the vector mesons and protons reproduce the x_p dependence but show a larger normalization than the data. These differences were all seen in the flavor-inclusive results (figs. 13, 14), and we can now conclude that they all indicate problems with the modelling of light-flavor fragmentation, and cannot be due entirely to mismodelling of heavy hadron production and decay. The HERWIG prediction for pseudoscalar kaons is also larger than the data at low x_p and is slightly smaller than the data in the range $0.15 < x_p < 0.25$. For all hadron species the HERWIG prediction is larger than the data for $x_p > 0.4$, showing a characteristic shoulder structure. The UCLA predictions for the baryons and the vector mesons show a similar but less pronounced structure that is inconsistent with the proton and K^{*0}/\bar{K}^{*0} data. Otherwise UCLA reproduces the data except for pseudoscalar kaons in the range $0.015 < x_p < 0.03$.

In fig. 16 and tables 8–14 we give the ratios of production in b -flavor to light-flavor events for the seven species. The systematic errors on the hadron reconstruction and identification largely cancel in these ratios, and the total errors are predominantly statistical. There is higher production of charged pions in b -flavor events than in light-flavor events at low x_p , with the ratio rising with x_p for $0.008 < x_p < 0.03$ to a plateau value of about 1.25. The production of both charged and neutral kaons is approximately equal in the two samples for $x_p < 0.03$, but the relative production in b -flavor events then increases with x_p , peaking at a value of about 1.7 at $x_p \approx 0.09$. The errors on the K^{*0}/\bar{K}^{*0} and ϕ ratios are large, but the data are consistent with behavior similar to that of the pseudoscalar kaon ratios. There is approximately equal production of baryons in b -flavor and light-flavor events for $x_p < 0.15$. The production of pions and pseudoscalar kaons in b -flavor events falls rapidly with x_p for $x_p > 0.1$ relative to that in light-flavor events. The relative production of the vector mesons and protons also falls at high x_p .

These features are consistent with expectations based on the known properties of $e^+e^- \rightarrow b\bar{b}$ events, namely that a large fraction of the event energy (on average about 70% [7]) is carried by the leading B - and \bar{B} -hadrons, leaving little energy available to produce high momentum fragmentation hadrons. The B hadrons decay into a large number of lighter particles, including on average 5.5 stable charged hadrons [27], which are expected to populate primarily the region $0.02 < x_p < 0.2$. Also shown in fig. 16 are the predictions of

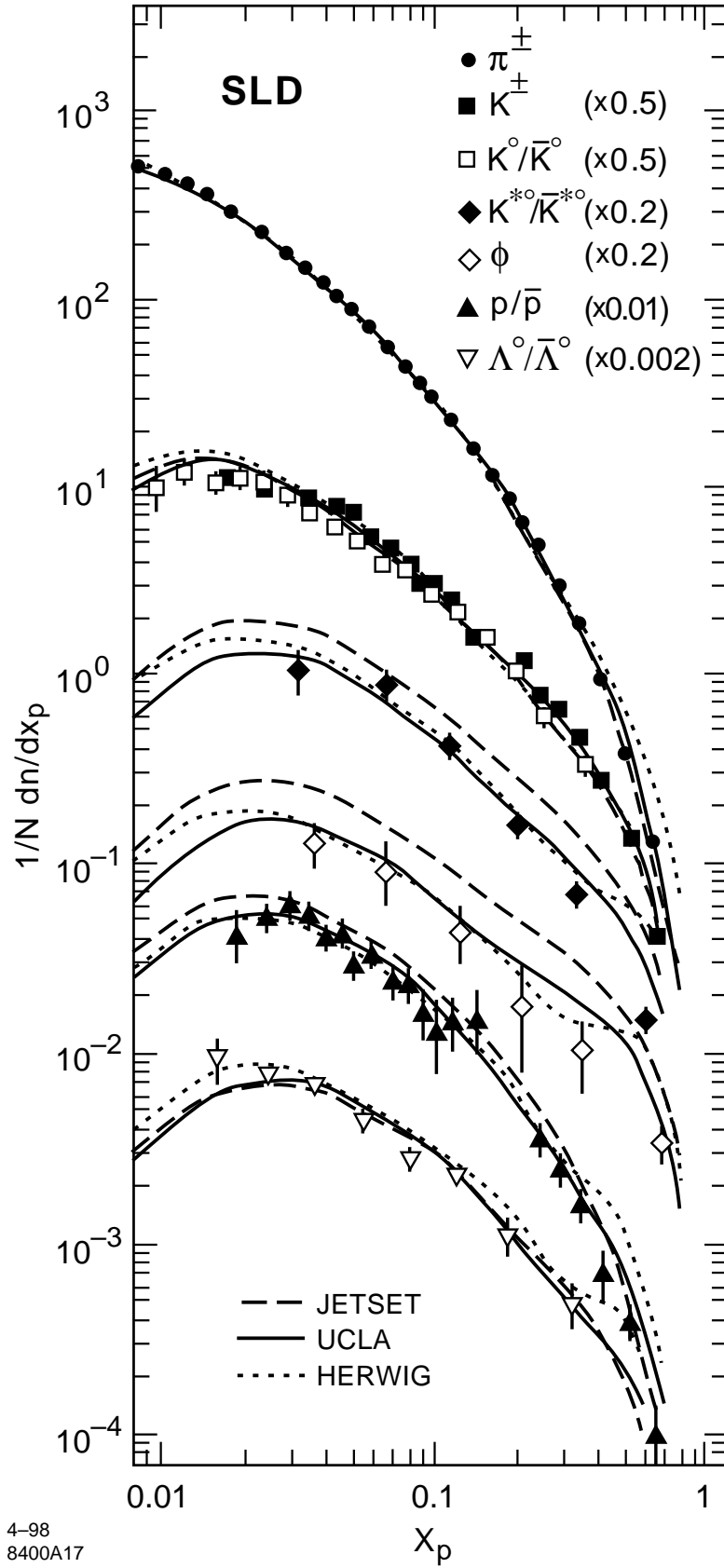


Figure 15: Identified hadron differential cross sections in light-flavor events. Also shown are the predictions of the three fragmentation models; the prediction of each model for K^\pm is similar to that for K^0/\bar{K}^0 , and the two have been averaged.

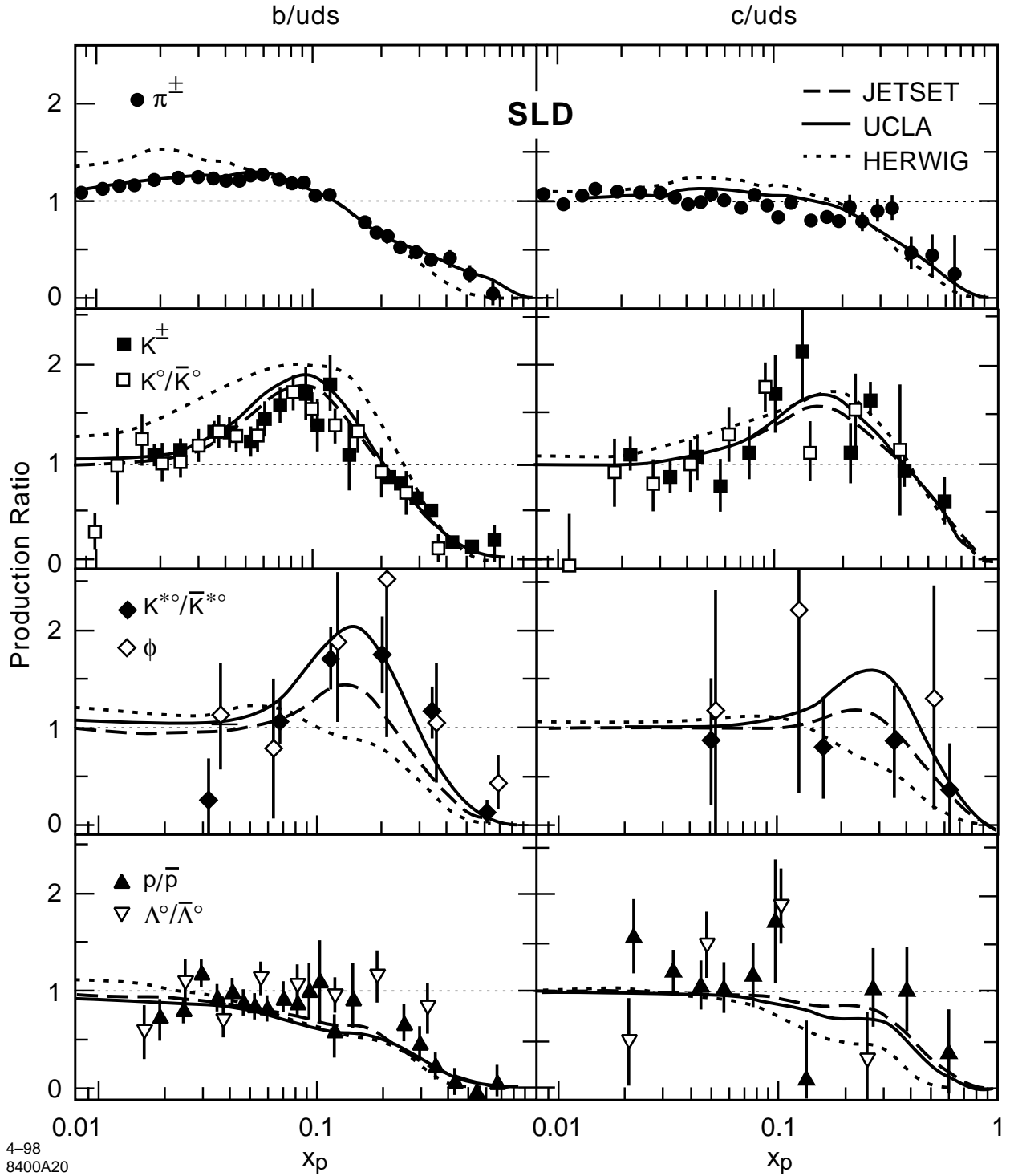


Figure 16: Ratios of production of each hadron species in b -flavor events to that in light-flavor events (left) and in c -flavor:light-flavor events (right). Also shown are the predictions of the three fragmentation models; for each model, the predictions for K^\pm and K^0/\bar{K}^0 were averaged, as were those for p/\bar{p} and $\Lambda^0/\bar{\Lambda}^0$. The model predictions for ϕ are not shown, but have the same x_p dependence as the corresponding prediction for K^{*0}/\bar{K}^{*0} , with a peak value typically higher by 40%.

the three fragmentation models, all of which reproduce these features qualitatively, although HERWIG overestimates the ratio for pions in the range $x_p < 0.05$ and that for kaons for $x_p < 0.3$. The values of these ratios depend on details of the B and D hadron energy spectra and decay properties, and so provide information complementary to that in fig. 15. However, in drawing conclusions regarding heavy flavor modelling from these ratios, one must consider how well the model in question reproduces the light flavor results. For example, the HERWIG prediction for pion (kaon) production in light-flavor events (fig. 15) is consistent with (higher than) the data for $x_p < 0.05$, so it is safe to conclude from fig. 16 that HERWIG mismodels pion and kaon production from B decays in this region. However the fact that the HERWIG ratio for kaons is high in the region $0.1 < x_p < 0.3$ is due at least in part to the low HERWIG prediction for kaon production in light-flavor events in that region.

In fig. 16 we also show the ratios of production in c -flavor to light-flavor events for the seven species. The errors are larger than for the $b:uds$ comparison and x_p bins have been combined in some cases for clarity. Similar qualitative features are observed: there is higher kaon production in c -flavor events than in light-flavor events at $x_p \sim 0.1$; pion production is slightly higher in c -flavor than in light-flavor events for $x_p < 0.03$, then decreases slowly with x_p ; both pion and kaon production appear to fall rapidly with x_p for $x_p > 0.3$, a somewhat higher value than the corresponding $b:uds$ ratios. These features are expected since c -jets produce a charmed hadron with on average about half [7] the beam energy, a lower fraction than B -hadrons, which leaves more energy available for fragmentation hadrons than in b -jets. The charmed hadron decay products often include a kaon carrying a large fraction of the charmed hadron momentum, and there are fewer additional charged pions than in B hadron decays. Also shown in fig. 16 are the $c:uds$ ratios predicted by the three fragmentation models. All models are consistent with the data, except that HERWIG overestimates the pion ratio for $0.03 < x_p < 0.15$.

6 Comparison with QCD Predictions

We tested the predictions of Gribov and Lipatov, that, in the limit $x_p \rightarrow 1$, the momentum distribution for primary leading hadrons be $(1 - x_p)^n$, with $n = 2$ for mesons and $n = 3$ for baryons. Since this test benefits from more bins at high x_p , we considered only the charged hadrons. The cross sections measured in light flavor events provide in principle a better test than those measured in flavor-inclusive events, since c - and b -flavor events cannot contain primary leading pions, kaons or protons. However, we have just shown that the contributions from c - and b -flavor events are small for x_p greater than about 0.5; since we have better statistics for flavor-inclusive events we performed the test on this data set, as well as on the light-flavor data. We are limited to $x_p < 0.77$ for the charged pions and kaons, but for the flavor-inclusive analysis of protons we have an additional bin, obtained from a 2-hypothesis analysis (see sec. 4.1) that also yielded the sum of meson cross sections ($\pi^\pm + K^\pm$). We also considered this meson sum at all momenta, which has smaller statistical errors than the sum of the individual π^\pm and K^\pm cross sections.

Figure 17 shows the π^\pm , K^\pm , p and $(\pi^\pm + K^\pm)$ differential cross sections as functions of $(1 - x_p)$ in flavor-inclusive Z^0 decays. Fits of the function $f(x) = A(1 - x_p)^n$, with the value of n fixed to 2 (3 for protons), were performed to the first m data points and the resulting

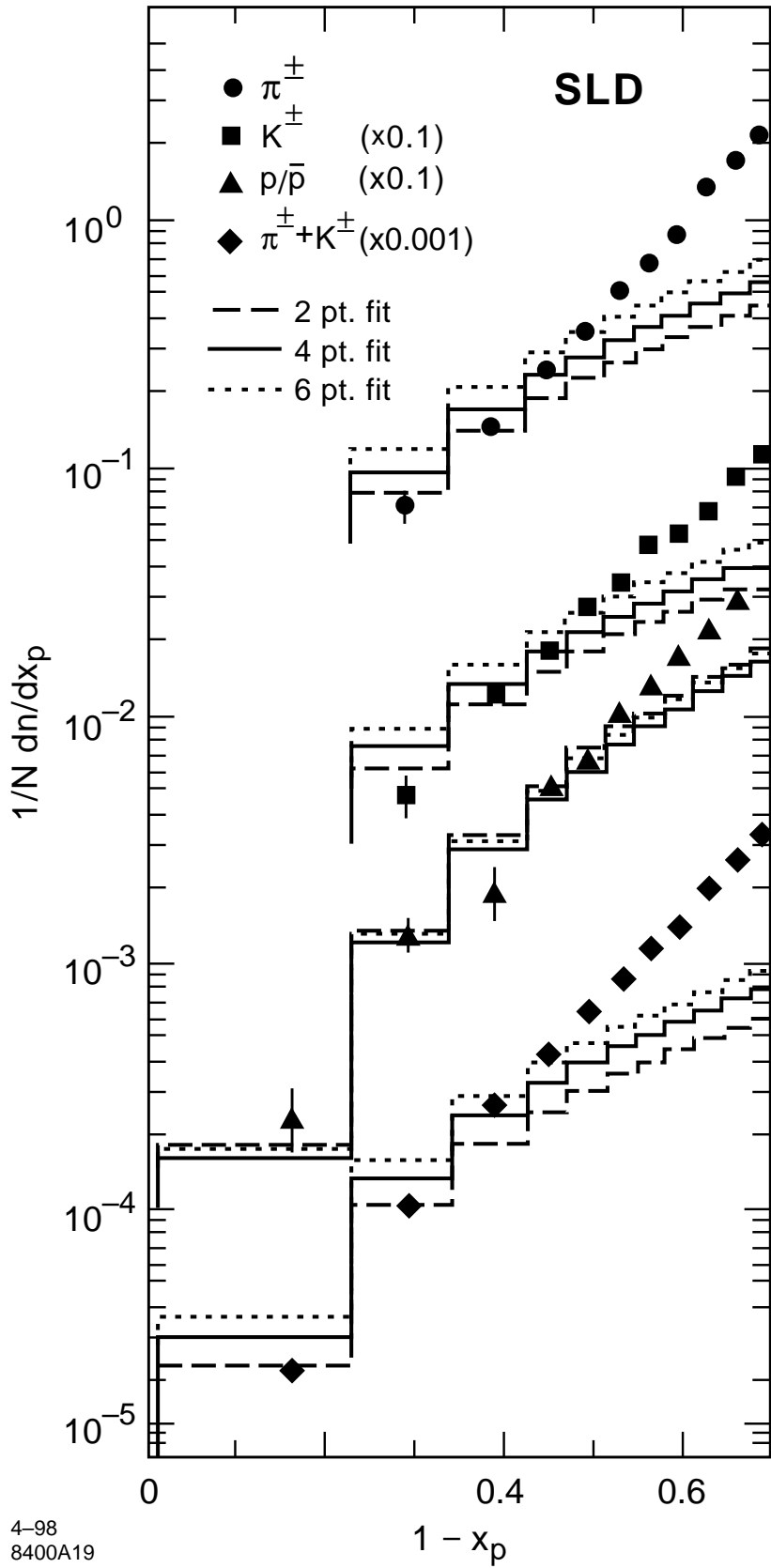
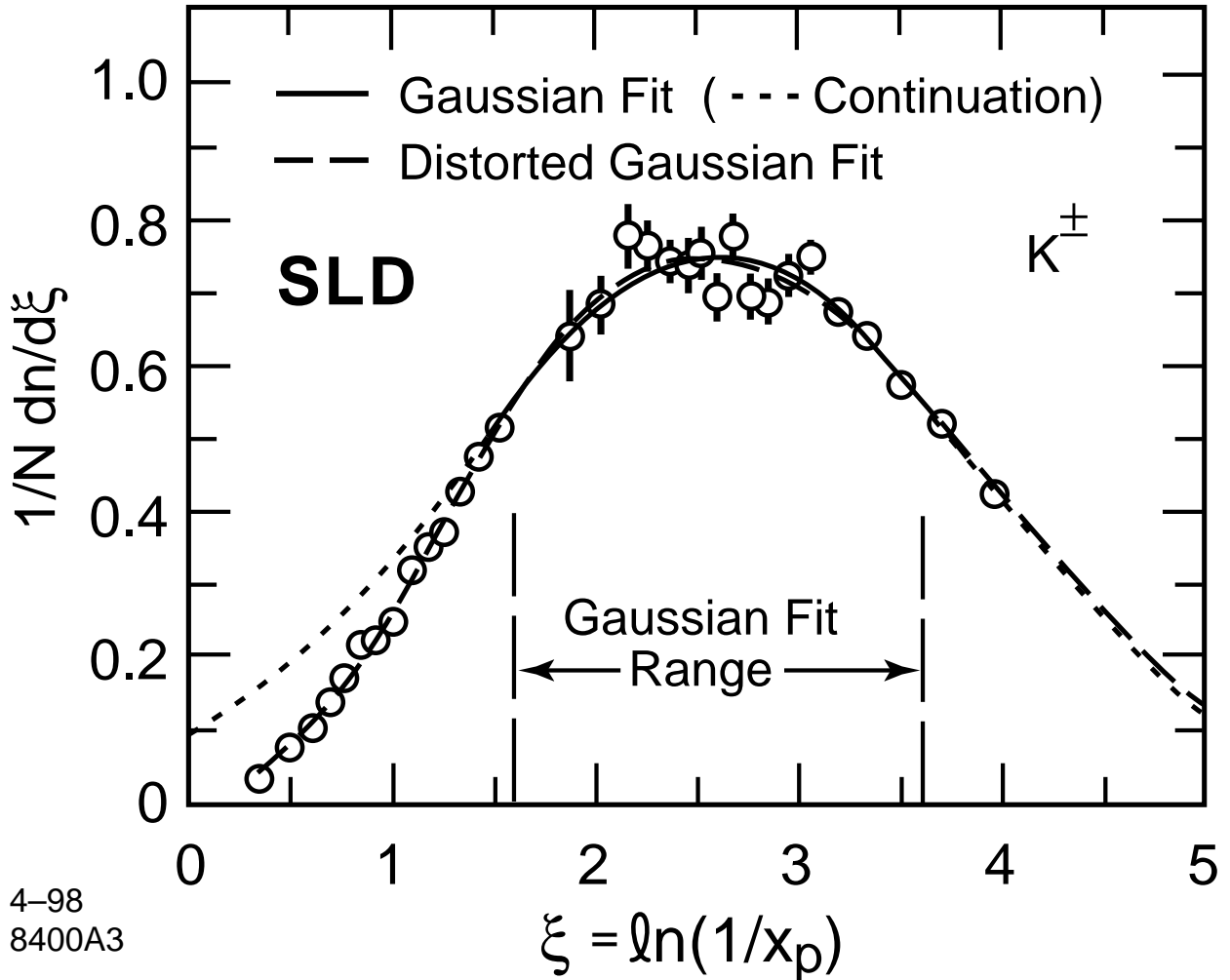


Figure 17: Measured differential cross sections in flavor-inclusive Z^0 decays as a function of $(1 - x_p)$, along with the results of polynomial fits, described in the text, to the data in the 2, 4 and 6 leftmost bins. Each fitted polynomial has been integrated over each bin and is shown as a histogram.



4-98
8400A3

Figure 18: Distribution of $\xi = \ln(1/x_p)$ for charged kaons in flavor-inclusive Z^0 decays. The solid and dashed lines indicated the results of fits of the Gaussian and distorted Gaussian approximations of MLLA QCD described in the text. The dotted lines indicate the continuations of the fitted Gaussian function.

fitted distributions for $m = 2, 4, 6$ are shown in the figure. In all cases the fit quality is good for $m = 2$, but worsens with increasing m . The maximum number of bins for which the confidence level of the χ^2 of the fit exceeded 0.01 was 3 for π^\pm and K^\pm , 6 for p/\bar{p} , and 2 for the meson sum ($\pi^\pm + K^\pm$).

Using this criterion, the theoretical prediction is consistent with our combined meson data for $(1 - x_p) < 0.34$, with our pion and kaon data for $(1 - x_p) < 0.47$, and with our proton data for $(1 - x_p) < 0.57$. A similar analysis of the light-flavor sample (not shown) yielded similar results; the prediction is consistent with our pion, kaon and combined meson data for $(1 - x_p) < 0.53$, and with our proton data for $(1 - x_p) < 0.62$.

In order to test the predictions of QCD in the Modified Leading Logarithm Approximation (MLLA) combined with the ansatz of Local Parton-Hadron Duality (LPHD), we converted our measurements into differential cross sections in the variable $\xi = \ln(1/x_p)$. Figure 18 shows our measured differential cross section as a function of ξ for the charged kaons. Also shown are the results of fits to a simple Gaussian, and a distorted Gaussian including skewness and kurtosis terms. The Gaussian fit was performed over a ξ range of

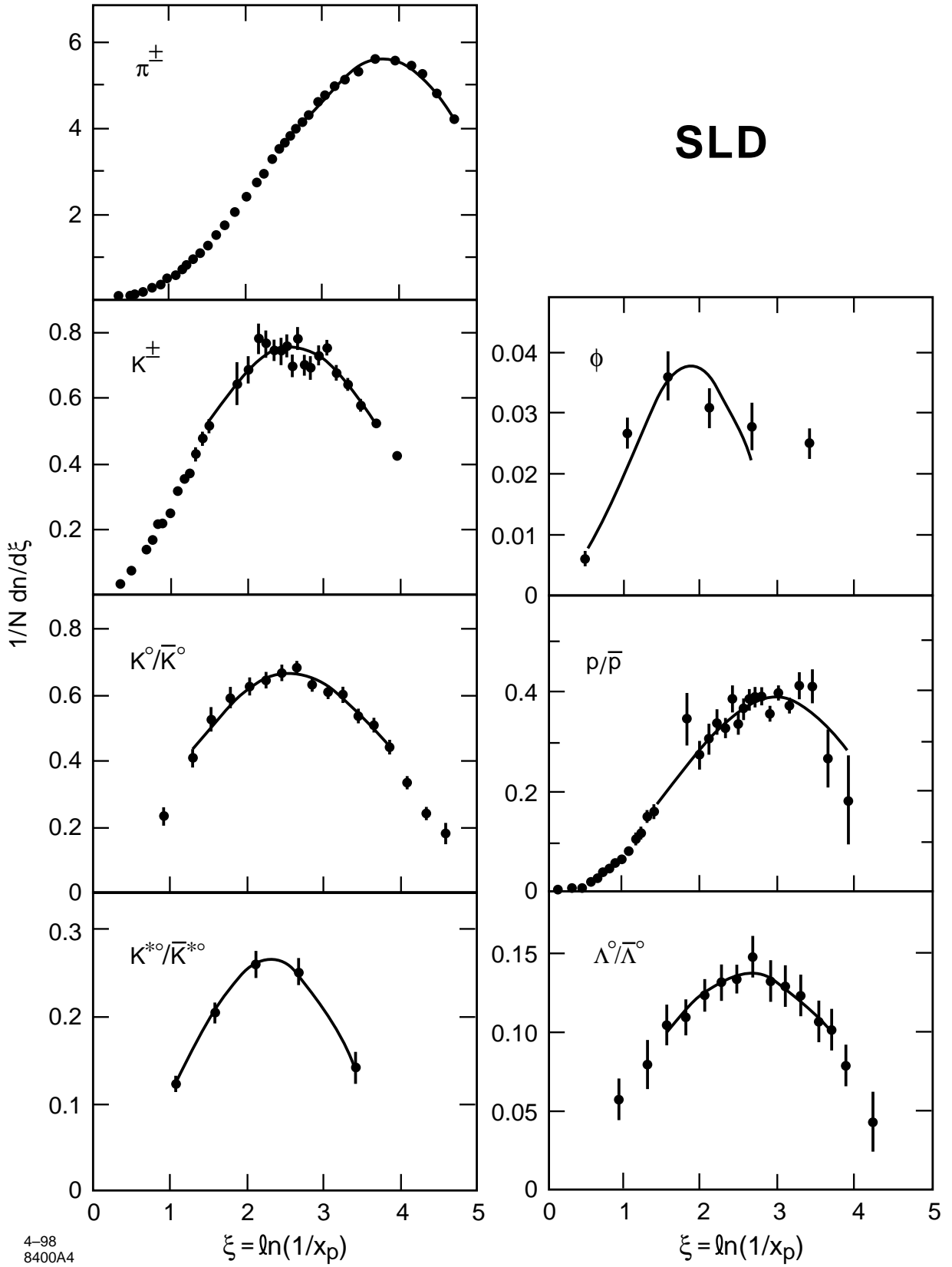


Figure 19: Distributions of ξ for the seven hadron species in flavor-inclusive hadronic Z^0 decays (points), along with the results of Gaussian fits (solid lines) to the data over a range of approximately ± 1 unit about the peak.

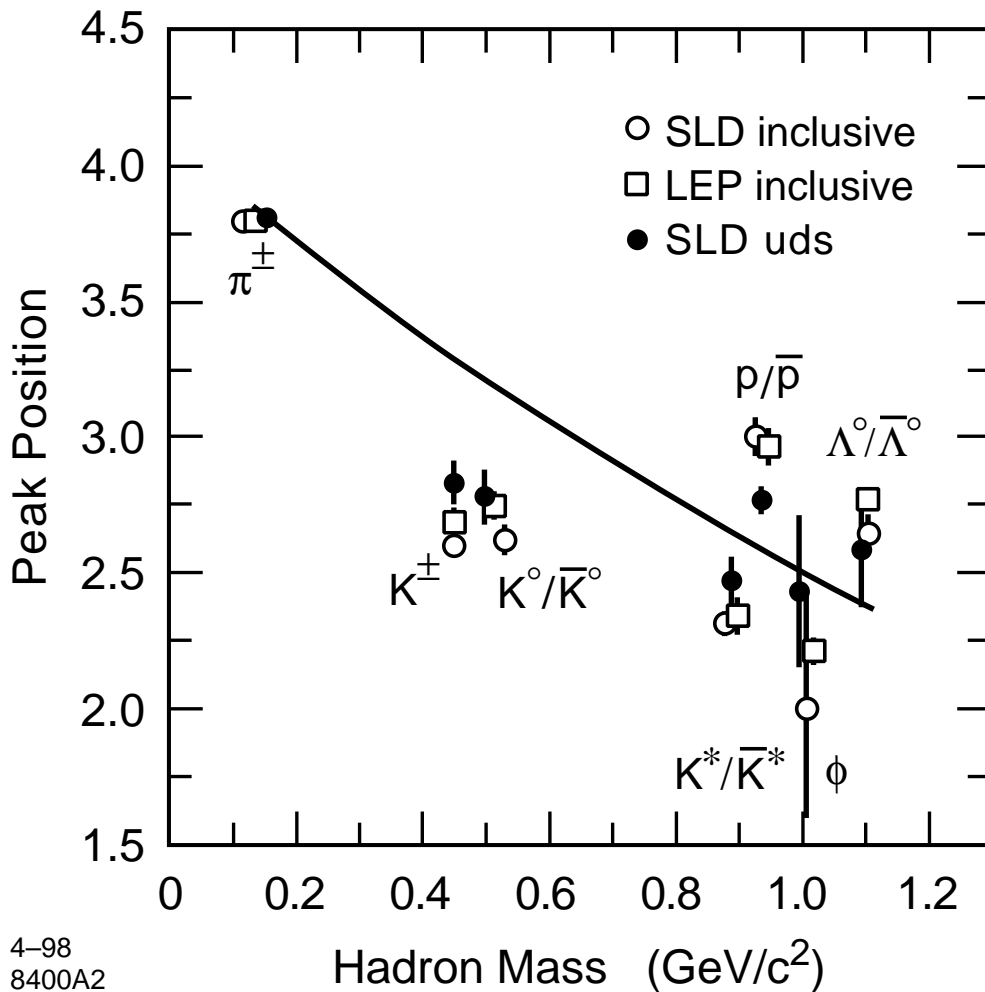


Figure 20: Peak positions ξ^* from fits to the ξ distributions in flavor-inclusive and light-flavor hadronic Z^0 decays. Also shown are averages of similar flavor-inclusive results from experiments at LEP. The line is the result of an ad hoc exponential fit to our light-flavor data.

width 2 units positioned near the maximum of the distribution. The fitted peak position ξ^* was found to be independent of the exact position of this range within statistical errors, and the solid line in fig. 18 represents the result of a fit over a range centered on this peak position. A good fit quality was obtained; the two points above this ξ range could be added to the fit, as could the first two points below the range, before the χ^2 began to increase rapidly, indicating that the Gaussian approximation is consistent with our data over a range of approximately ± 1.3 units of ξ around the peak position. The distorted Gaussian function is able to describe the data over the full measured range of ξ , as indicated by the dashed line in fig. 18, however the distortion terms grow rapidly as points outside the range described by the simple Gaussian are added.

Similar results were obtained for the other hadron species. Their ξ -distributions are shown in fig. 19. We fitted a simple Gaussian over a ξ range of approximately ± 1 unit centered on the maximum of each distribution in order to measure the peak position ξ^* for each hadron species. Systematic errors on this measurement were evaluated by varying the fit range and by refitting with each source of correlated experimental systematic error considered coherently in turn. Good fit qualities were obtained when the correlated systematic errors

	all flavors	light flavors	c	b
π^\pm	3.80 ± 0.01	3.81 ± 0.01	3.85 ± 0.04	3.71 ± 0.01
K^\pm	2.60 ± 0.03	2.83 ± 0.08	2.52 ± 0.12	2.67 ± 0.04
K^0/\bar{K}^0	2.62 ± 0.05	2.78 ± 0.10	2.32 ± 0.35	2.61 ± 0.06
K^{*0}/\bar{K}^{*0}	2.31 ± 0.04	2.47 ± 0.09	–	2.11 ± 0.07
ϕ	2.0 ± 0.4	2.43 ± 0.28	–	2.18 ± 0.18
p/\bar{p}	3.00 ± 0.07	2.77 ± 0.05	3.03 ± 0.26	2.86 ± 0.07
$\Lambda^0/\bar{\Lambda}^0$	2.64 ± 0.07	2.58 ± 0.21	2.75 ± 0.15	2.47 ± 0.18

Table 15: Peak positions ξ^* from Gaussian fits to the ξ distributions for each hadron species measured in flavor-inclusive and flavor-specific hadronic Z^0 decays. The errors are the sum in quadrature of statistical and systematic components.

were taken into account. The peak positions are given in table 15 and shown as a function of hadron mass in fig. 20, along with averages of similar measurements from experiments at LEP [7], with which they are consistent. The distribution for pions peaks at a higher ξ value than the those of the other hadron species, but otherwise there is no monotonic mass-dependence.

As discussed in section 1, the MLLA QCD+LPHD prediction is valid for primary fragmentation particles, whereas experiments so far have measured samples that include decay products of an unknown mix of resonances as well as of heavy hadrons. This mix may affect measured ξ^* values differently for different hadron species. It is of interest to try to resolve this question experimentally, and we have therefore applied the same analysis to the three primary event flavor categories discussed in the previous section. We expect the light flavor events to be less affected by decay products, as D - and B -hadron decays are excluded.

The Gaussian function provides an acceptable description of the ξ distribution for all hadron species in events of each flavor within about ± 1 unit of the peak (not shown), and the fitted peak positions are listed in table 15. For the K^{*0}/\bar{K}^{*0} and ϕ in c -flavor events, the limited sample size did not allow a reasonable systematic error evaluation, so they are omitted.

The ξ^* values measured in b -flavor events are significantly different from those measured in light-flavor events for π^\pm and K^{*0}/\bar{K}^{*0} ; the difference is 1.5σ for K^\pm and K^0/\bar{K}^0 . For the other hadron species the ξ^* values measured in events of all three flavors are consistent. The ξ^* values measured in light-flavor events differ significantly from those measured in flavor-inclusive events for K^\pm and p/\bar{p} . The light-flavor ξ^* values are also shown in fig. 20. The result of an ad hoc exponential fit to the light-flavor data is shown in fig. 20 as a reference trajectory, and the light-flavor data are seen to lie closer to a monotonic trajectory than the flavor-inclusive data.

	Total Cross Sections per Event of Flavor				Differences	
	all	<i>uds</i>	<i>c</i>	<i>b</i>	<i>c - uds</i>	<i>b - uds</i>
π^\pm	16.84±0.37	16.46±0.47	16.30±1.01	18.36±0.52	-0.15±0.96	1.91±0.36
K^\pm	2.22±0.16	2.04±0.15	2.47±0.28	2.40±0.19	0.43±0.23	0.36±0.10
K^0	2.01±0.08	1.86±0.09	1.86±0.21	2.11±0.11	0.01±0.21	0.25±0.09
K^{*0}	0.707±0.041	0.727±0.081	0.561±0.316	0.768±0.124	-0.166±0.321	0.041±0.132
ϕ	0.105±0.008	0.091±0.021	0.131±0.091	0.121±0.026	0.040±0.093	0.030±0.031
p	1.03±0.13	1.06±0.14	1.06±0.21	0.91±0.13	0.01±0.17	-0.15±0.07
Λ^0	0.395±0.022	0.421±0.030	0.341±0.088	0.383±0.032	-0.080±0.091	-0.038±0.039

Table 16: Corrected total cross sections per hadronic Z^0 decay, and per decay into light, c or b primary flavor. Differences between the total cross sections for c - and light-flavor and b - and light-flavor events. All errors are the sum in quadrature of experimental and extrapolation uncertainties

7 Total Production Cross Sections

We have integrated our differential cross sections over their respective measurement ranges, taking into account the bin-to-bin correlations in the systematic errors. These integrated cross sections per event are listed in tables 2–7; the errors are dominated by overall normalization uncertainties corresponding to the uncertainty in our track reconstruction efficiency. In order to quote total cross sections, we must extrapolate into the unmeasured regions of x_p , and we have done this using the three MC models discussed above. From the hadrons of each species generated using each of these models, we calculated the fraction that were generated with x_p in the range of our measurement. For each hadron species the three fractions were found to be similar, with the UCLA (HERWIG) fraction being typically 1% larger (1–2% smaller) than the JETSET fraction. The average of the three accepted fractions ranged from 0.812 for K^\pm to 0.945 for K^0/\bar{K}^0 . Each integrated measured cross section was divided by the corresponding average fraction, and an uncertainty of ± 0.01 (± 0.015) was assigned to the average fraction for π^\pm , K^\pm , K^0/\bar{K}^0 , p/\bar{p} and $\Lambda^0/\bar{\Lambda}^0$ (K^{*0}/\bar{K}^{*0} and ϕ), corresponding to a typical rms among the three predictions. The corrected total cross sections are shown in table 16, and were found to be consistent with an average of similar measurements from experiments at LEP [7].

As a cross check, we fitted the distorted Gaussian function described in section 6 to the ξ distribution for each hadron species, and calculated the fraction of the area under the fitted curve that was within the range of our measurement. An uncertainty was assigned corresponding to the largest variation obtained by varying the fitted parameter values by all combinations of $+1\sigma$ and -1σ . The resulting fractions are consistent with those obtained using the fragmentation models, giving confidence in both the central values and the uncertainties assigned.

We applied the same procedure to our measurements for the three flavor categories.

The three simulations were found to give similar flavor dependences, with the accepted fraction in b (c) events typically 0.02 (0.01) larger than that in light-flavor events. The resulting total cross sections are listed in table 16 along with differences between flavors, for which some of the systematic errors cancel. We observe roughly 15% more pseudoscalar mesons in b -flavor events than in light-flavor events, and the respective sums of the charged hadron differences are consistent with our previous measurement [31] of the differences in total charged multiplicity between light-, c - and b -flavor events. All other differences are consistent with zero.

8 Leading Particle Effects

We extended these studies to look for differences between particle and antiparticle production in light quark (as opposed to antiquark) jets, in order to address the question of whether e.g. a primary u -initiated jet contains more hadrons that contain a valence u -quark (e.g. π^+ , K^+ , p , Λ^0) than hadrons that do not (e.g. π^- , K^- , \bar{p} , $\bar{\Lambda}^0$). To this end we used the light quark- and antiquark-tagged hemispheres described in section 3.

We measured the differential cross sections per light quark jet

$$R_h^q = \frac{1}{2N_{evts}} \frac{d}{dx_p} \left[N(q \rightarrow h) + N(\bar{q} \rightarrow \bar{h}) \right], \quad (3)$$

$$R_{\bar{h}}^q = \frac{1}{2N_{evts}} \frac{d}{dx_p} \left[N(q \rightarrow \bar{h}) + N(\bar{q} \rightarrow h) \right], \quad (4)$$

where: q and \bar{q} represent light-flavor quark and antiquark jets respectively; N_{evts} is the total number of events in the sample; h represents any of the identified hadron species π^- , K^- , \bar{K}^{*0} , p , or Λ^0 , and \bar{h} indicates the corresponding antihadron. Then, for example, $N(q \rightarrow h)$ is the number of hadrons of species h in light quark jets. This formulation assumes CP symmetry, i.e. $N(q \rightarrow h) = N(\bar{q} \rightarrow \bar{h})$, which was found to be satisfied in the data in all cases.

The charged hadron fractions analysis was repeated on the sample of positively charged tracks in the quark-tagged jets and negatively charged tracks in the antiquark-tagged jets, yielding measured values of $R_{\pi^+}^q$, $R_{K^+}^q$, and R_p^q in the tagged samples. The same procedure applied to the remaining tracks yielded $R_{\pi^-}^q$, $R_{K^-}^q$, and $R_{\bar{p}}^q$. The K^{*0}/\bar{K}^{*0} and $\Lambda^0/\bar{\Lambda}^0$ analyses were applied similarly to the quark- and antiquark-tagged jets to yield $R_{K^{*0}}^q$, $R_{\bar{K}^{*0}}^q$, R_{Λ}^q and $R_{\bar{\Lambda}}^q$.

The light-tagged event sample contains a residual heavy flavor background of 12% $c\bar{c}$ and 3% $b\bar{b}$ events. The decays of the leading heavy hadrons in simulated heavy flavor background events give rise to substantial differences between hadron and antihadron production in the quark-tagged sample over the entire x_p range. It is essential to understand this contribution, which is typically 15% of the observed hadrons for $x_p < 0.5$ and decreases at higher x_p (see fig. 16). The simulated contribution to each cross section was applied as a correction, yielding differential cross sections per light-quark-tagged jet.

For each hadron species, differential cross sections in light quark jets were then extracted by correcting for the light-tag bias (see sec. 5) and unfolding for the effective quark (vs. antiquark) purity. The purity was estimated from the simulation to be 0.76 for the $\Lambda^0/\bar{\Lambda}^0$

x_p Range	$\langle x_p \rangle$	π^+ and π^- Production in u,d,s Jets		
		π^+	π^-	D_{π^-}
0.016–0.022	0.019	140.9±2.5	139.0±2.6	−0.007±0.016
0.022–0.033	0.027	98.2±1.5	96.7±1.4	−0.007±0.014
0.033–0.044	0.038	62.8±1.3	63.6±1.3	0.007±0.019
0.044–0.055	0.049	44.2±1.4	44.9±1.4	0.007±0.029
0.055–0.066	0.060	33.4±1.1	33.2±1.1	−0.003±0.030
0.066–0.077	0.071	25.79±0.82	27.16±0.82	0.026±0.028
0.077–0.088	0.082	21.66±0.71	22.34±0.71	0.016±0.029
0.088–0.099	0.093	17.17±0.62	18.40±0.63	0.034±0.032
0.099–0.110	0.104	14.45±0.57	14.52±0.57	0.003±0.036
0.110–0.121	0.115	11.44±0.50	12.84±0.52	0.057±0.038
0.121–0.143	0.131	9.32±0.32	9.61±0.32	0.015±0.031
0.143–0.164	0.153	7.21±0.28	7.39±0.28	0.012±0.035
0.164–0.186	0.175	5.40±0.24	5.49±0.25	0.008±0.041
0.186–0.208	0.197	4.30±0.21	4.44±0.22	0.016±0.045
0.208–0.230	0.219	3.14±0.19	3.30±0.19	0.026±0.053
0.230–0.274	0.251	2.37±0.12	2.59±0.12	0.043±0.043
0.274–0.318	0.295	1.398±0.091	1.687±0.097	0.093±0.055
0.318–0.384	0.348	0.972±0.061	0.996±0.064	0.012±0.057
0.384–0.471	0.423	0.456±0.040	0.504±0.042	0.050±0.077
0.471–0.603	0.527	0.180±0.025	0.210±0.026	0.08±0.12
0.603–0.768	0.668	0.065±0.019	0.089±0.021	0.16±0.23

Table 17: Differential cross sections for the production of positive and negative pions in light (u , d and s) quark jets from hadronic Z^0 decays, along with the normalized difference D_{π^-} between the two. The errors are the sum in quadrature of statistical errors and those systematic errors arising from the light quark tagging and unfolding procedure.

and 0.72 for the charged hadrons and K^{*0}/\bar{K}^{*0} , the latter value reflecting the cutoff in acceptance of the CRID at $|\cos\theta| = 0.68$.

The measured differential cross sections per light quark jet are listed in tables 17–21 for the five measured hadron species that are not self-conjugate. As for the flavor dependent results (sec. 5), the error given is the sum in quadrature of the statistical error and those systematic errors arising from the tagging and correction procedures. The latter include variation of the event tagging efficiencies and biases as described in section 5, variation of the electroweak parameters R_b , R_c , A_b and A_c by the errors on their respective world average values [27], and variation of the effective quark purity by ± 0.015 to cover the uncertainty in the electron beam polarization and statistical error on the simulated purity. The systematic errors are small compared with the statistical errors, and are typically dominated by the uncertainty on the effective quark purity. These results supersede those in our previous publication [8].

x_p Range	$\langle x_p \rangle$	K^{*0} and \bar{K}^{*0} Production in u,d,s Jets		
		K^{*0}	\bar{K}^{*0}	$D_{\bar{K}^{*0}}$
0.018–0.048	0.033	2.50 ± 0.94	2.69 ± 0.95	0.04 ± 0.29
0.048–0.088	0.068	1.64 ± 0.36	2.40 ± 0.38	0.18 ± 0.14
0.088–0.149	0.118	1.11 ± 0.22	0.88 ± 0.22	-0.11 ± 0.17
0.149–0.263	0.206	0.318 ± 0.087	0.447 ± 0.095	0.17 ± 0.19
0.263–0.483	0.342	0.053 ± 0.033	0.264 ± 0.042	0.67 ± 0.18
0.483–1.000	0.607	0.022 ± 0.012	0.100 ± 0.015	0.64 ± 0.16

Table 18: Differential cross sections for the production of K^{*0} and \bar{K}^{*0} mesons in light quark jets, along with their normalized difference.

x_p Range	$\langle x_p \rangle$	K^+ and K^- Production in u,d,s Jets		
		K^+	K^-	D_{K^-}
0.016–0.022	0.019	8.3 ± 1.1	14.8 ± 1.3	0.28 ± 0.09
0.022–0.033	0.027	9.27 ± 0.69	8.14 ± 0.68	-0.06 ± 0.07
0.033–0.044	0.038	8.05 ± 0.68	7.70 ± 0.68	-0.02 ± 0.08
0.044–0.055	0.049	8.03 ± 0.81	7.59 ± 0.81	-0.03 ± 0.09
0.055–0.066	0.060	3.75 ± 0.74	6.27 ± 0.79	0.25 ± 0.14
0.066–0.088	0.077	3.44 ± 0.45	3.90 ± 0.47	0.06 ± 0.11
0.088–0.121	0.101	3.09 ± 0.41	2.73 ± 0.42	-0.06 ± 0.13
0.208–0.230	0.219	0.99 ± 0.18	1.36 ± 0.19	0.15 ± 0.14
0.230–0.274	0.251	0.595 ± 0.091	1.120 ± 0.099	0.31 ± 0.10
0.274–0.318	0.295	0.383 ± 0.072	0.895 ± 0.081	0.40 ± 0.11
0.318–0.384	0.348	0.260 ± 0.049	0.665 ± 0.055	0.44 ± 0.10
0.384–0.471	0.423	0.163 ± 0.034	0.427 ± 0.039	0.45 ± 0.11
0.471–0.603	0.527	0.091 ± 0.023	0.219 ± 0.026	0.42 ± 0.14
0.603–0.768	0.668	-0.007 ± 0.017	0.120 ± 0.022	1.12 ± 0.28

Table 19: Differential cross sections for the production of positive and negative kaons in light quark jets from hadronic Z^0 decays, along with their normalized difference.

x_p Range	$\langle x_p \rangle$	p and \bar{p} Production in u,d,s Jets		
		p	\bar{p}	D_p
0.022–0.033	0.027	7.1 ± 1.1	4.7 ± 1.4	0.20 ± 0.21
0.033–0.044	0.038	5.76 ± 0.52	4.83 ± 0.51	0.09 ± 0.09
0.044–0.055	0.049	4.10 ± 0.44	4.07 ± 0.44	0.00 ± 0.10
0.055–0.066	0.060	3.65 ± 0.44	3.20 ± 0.44	0.07 ± 0.12
0.066–0.088	0.077	2.69 ± 0.30	2.31 ± 0.30	0.08 ± 0.11
0.088–0.121	0.101	1.82 ± 0.29	1.99 ± 0.30	-0.04 ± 0.14
0.230–0.274	0.251	0.618 ± 0.078	0.292 ± 0.072	0.36 ± 0.15
0.274–0.318	0.295	0.387 ± 0.056	0.157 ± 0.053	0.42 ± 0.18
0.318–0.384	0.348	0.257 ± 0.035	0.099 ± 0.033	0.44 ± 0.18
0.384–0.471	0.423	0.117 ± 0.020	0.076 ± 0.019	0.21 ± 0.19
0.471–0.603	0.527	0.070 ± 0.010	0.025 ± 0.009	0.47 ± 0.19
0.603–0.768	0.668	0.018 ± 0.004	0.001 ± 0.004	0.85 ± 0.42

Table 20: Differential cross sections for the production of protons and antiprotons in light quark jets, along with their normalized difference.

x_p Range	$\langle x_p \rangle$	Λ^0 and $\bar{\Lambda}^0$ Production in u,d,s Jets		
		Λ^0	$\bar{\Lambda}^0$	D_{Λ^0}
0.010–0.030	0.022	0.65 ± 0.16	1.05 ± 0.17	-0.23 ± 0.18
0.030–0.050	0.040	0.86 ± 0.13	0.91 ± 0.13	-0.03 ± 0.14
0.050–0.070	0.060	0.529 ± 0.084	0.555 ± 0.084	-0.02 ± 0.14
0.070–0.100	0.083	0.303 ± 0.057	0.468 ± 0.060	-0.21 ± 0.14
0.100–0.140	0.118	0.301 ± 0.053	0.319 ± 0.054	-0.03 ± 0.16
0.140–0.180	0.158	0.190 ± 0.048	0.157 ± 0.047	0.09 ± 0.25
0.180–0.300	0.227	0.171 ± 0.034	0.098 ± 0.032	0.27 ± 0.23
0.300–0.500	0.368	0.090 ± 0.022	0.013 ± 0.019	0.75 ± 0.37

Table 21: Differential cross sections for the production of Λ^0 and $\bar{\Lambda}^0$ hyperons in light quark jets, along with their normalized difference.

It is convenient to show these results in the form of the difference between hadron h and antihadron \bar{h} production normalized by the sum:

$$D_h = \frac{R_h^q - R_{\bar{h}}^q}{R_h^q + R_{\bar{h}}^q}. \quad (5)$$

The common systematic errors cancel explicitly in this variable, which is shown for each hadron species in fig. 21. A value of zero corresponds to equal production of hadron and antihadron, whereas a value of $+(-)1$ corresponds to complete dominance of (anti)particle production. In each case the difference is consistent with zero at low x_p . For charged pions it is also consistent with zero at high x_p , but for the other hadrons there are significant positive differences that appear to increase with increasing x_p .

The results for the baryons (fig. 21a,b) afford the most straightforward interpretation. Since baryons contain valence quarks and not antiquarks, the observed excess of both protons and Λ^0 s over their respective antibaryons for $x_p > 0.2$ is clear evidence for the production of leading baryons. The data suggest that the effect increases with x_p , however more data are needed to study the x_p dependence in detail. For $x_p < 0.2$ the data are consistent with equal production of baryons and antibaryons, however the contribution from fragmentation is very high in this region and we cannot exclude that leading baryons are also produced at low x_p .

Since a meson contains one valence quark along with one valence antiquark, the interpretation of our results for mesons is more complicated. All down-type quarks are produced equally and with the same forward-backward asymmetry in Z^0 decays in the Standard Model, so that if a leading neutral particle such as \bar{K}^{*0} ($s\bar{d}$) were produced equally in s and \bar{d} jets (i.e. $D_{\bar{K}^{*0}}^{d\bar{d}} = -D_{\bar{K}^{*0}}^{s\bar{s}}$), then our measured $D_{\bar{K}^{*0}}$ would be zero. Our two highest- x_p points are significantly positive, indicating both that there is leading \bar{K}^{*0} production *and* that more leading \bar{K}^{*0} are produced in s jets than in \bar{d} jets. This is an expected consequence of strangeness suppression in the fragmentation process. That is, it is expected to be less likely for an $s\bar{s}$ to be produced from the vacuum and the s to pair up with an initial \bar{d} than it is for a $d\bar{d}$ to be produced and the \bar{d} to pair up with the initial s .

In the case of charged hadrons such as π^- ($d\bar{u}$), the different Z^0 branching ratios and forward-backward asymmetries of up- and down-type quarks cause a nonzero dilution of leading particle effects. Assuming Standard Model couplings to the Z^0 and equal production of leading π^+ in u -jets and π^- in d -jets (i.e. $D_{\pi^-}^{d\bar{d}} = -D_{\pi^-}^{u\bar{u}}$), we calculate a dilution factor for our analysis cuts of 0.27. That is, we would expect to observe $D_{\pi^-} = 0.27 D_{\pi^-}^{d\bar{d}}$. For purposes of illustration, we have fitted a line to our D_p and D_{Λ^0} points for $x_p > 0.2$, scaled it by the dilution factor 0.27, and drawn it as the dot-dashed line on figs. 21c and 21d. We do not necessarily expect that leading particle effects are identical for mesons and for baryons, but this line serves as a basis for a qualitative comparison.

Our measured D_{π^-} are consistent with zero everywhere, and consistently below this line. This does not rule out leading pion production, but indicates that nonleading production of pions must be comparable or larger at all x_p . This could be due to a very soft leading pion momentum distribution and/or a large “background” contribution of pions from decays of excited states such as ρ^0 , ω , η , K^* . Our measured D_{K^-} are consistently positive and above the line for $x_p > 0.2$. As in the case of \bar{K}^{*0}/K^{*0} , this indicates both production of leading charged kaons and more frequent production of leading K^- in s -jets than in \bar{u} -jets.

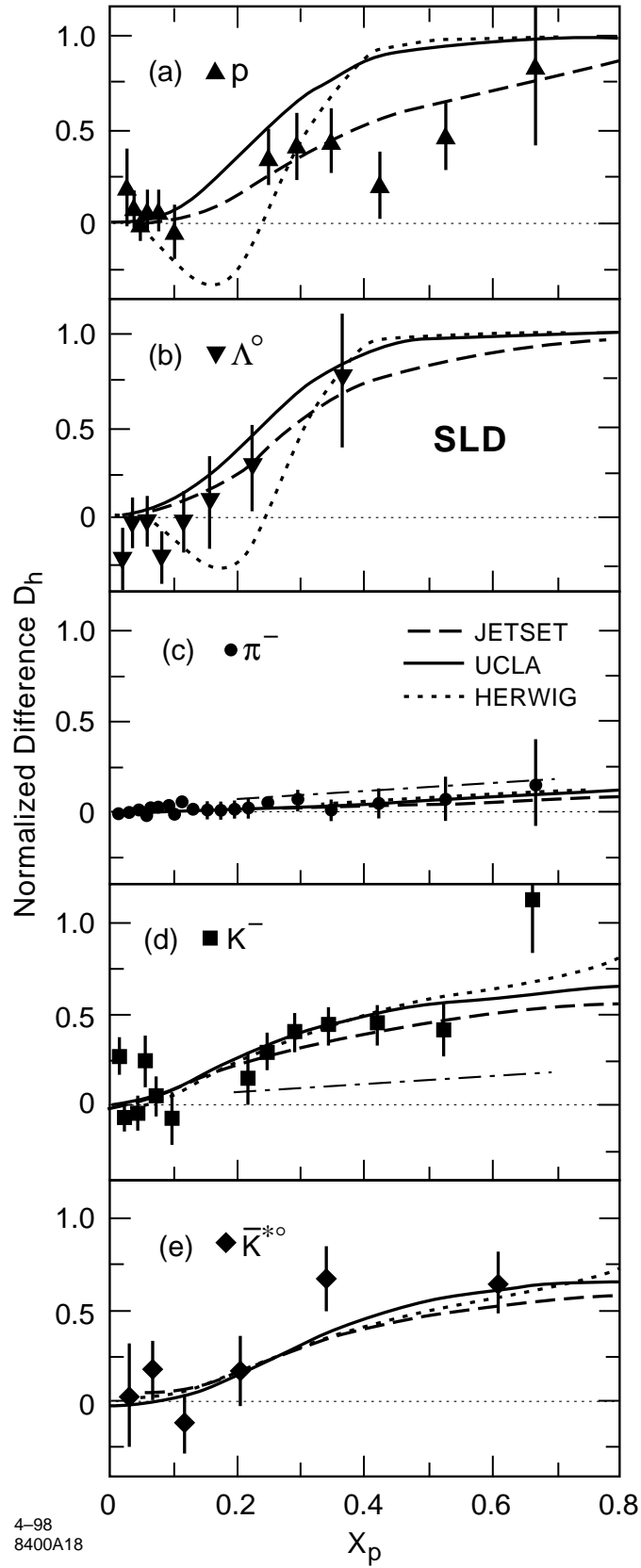


Figure 21: Normalized differences between hadron and antihadron production in light quark jets. The thin dot-dashed lines in (c) and (d) represent the fit to the baryon data scaled by the dilution factor of 0.27 described in the text. Also shown are the predictions of the three fragmentation models.

The quantification of the total number of observed leading particles is problematic. For example, in the region $x_p > 0.2$ we observe a total of 0.083 ± 0.005 protons and 0.036 ± 0.005 antiprotons per light quark jet. Some of the antiprotons are expected to be “subleading” antiprotons produced in association with a leading baryon, since baryon number is known to be conserved locally [32], whereas others are from a non-leading baryon-antibaryon pair, and provide a measure of the background of nonleading protons in the high- x_p sample. We conclude that the number of leading protons we have observed per light quark jet must lie between the p - \bar{p} difference and the total number of protons, i.e. in the range 0.047–0.083 per light quark jet. Similarly, the number of observed leading Λ^0 in the range $0.18 < x_p < 0.5$ is 0.024–0.039. For $x_p > 0.26$ we measure a total of $0.110 \pm 0.012 \bar{K}^{*0}$ and $0.023 \pm 0.010 K^{*0}$ per light quark jet. In this case, all of these could be leading due to contributions from s and d jets, and so the sum gives an upper bound on the number of leading K^{*0}/\bar{K}^{*0} produced. A lower bound is given by the possibility that no leading K^{*0} are produced in d jets. In this case all of the observed K^{*0} are nonleading, we expect an equal number of nonleading \bar{K}^{*0} , and the number of leading \bar{K}^{*0} produced is given by the $\bar{K}^{*0} - K^{*0}$ difference. Thus we have observed 0.087–0.133 leading K^{*0}/\bar{K}^{*0} per jet with $x_p > 0.26$. Similarly, the number of leading charged kaons produced in the range $0.21 < x_p < 0.77$ is 0.141–0.355 per jet.

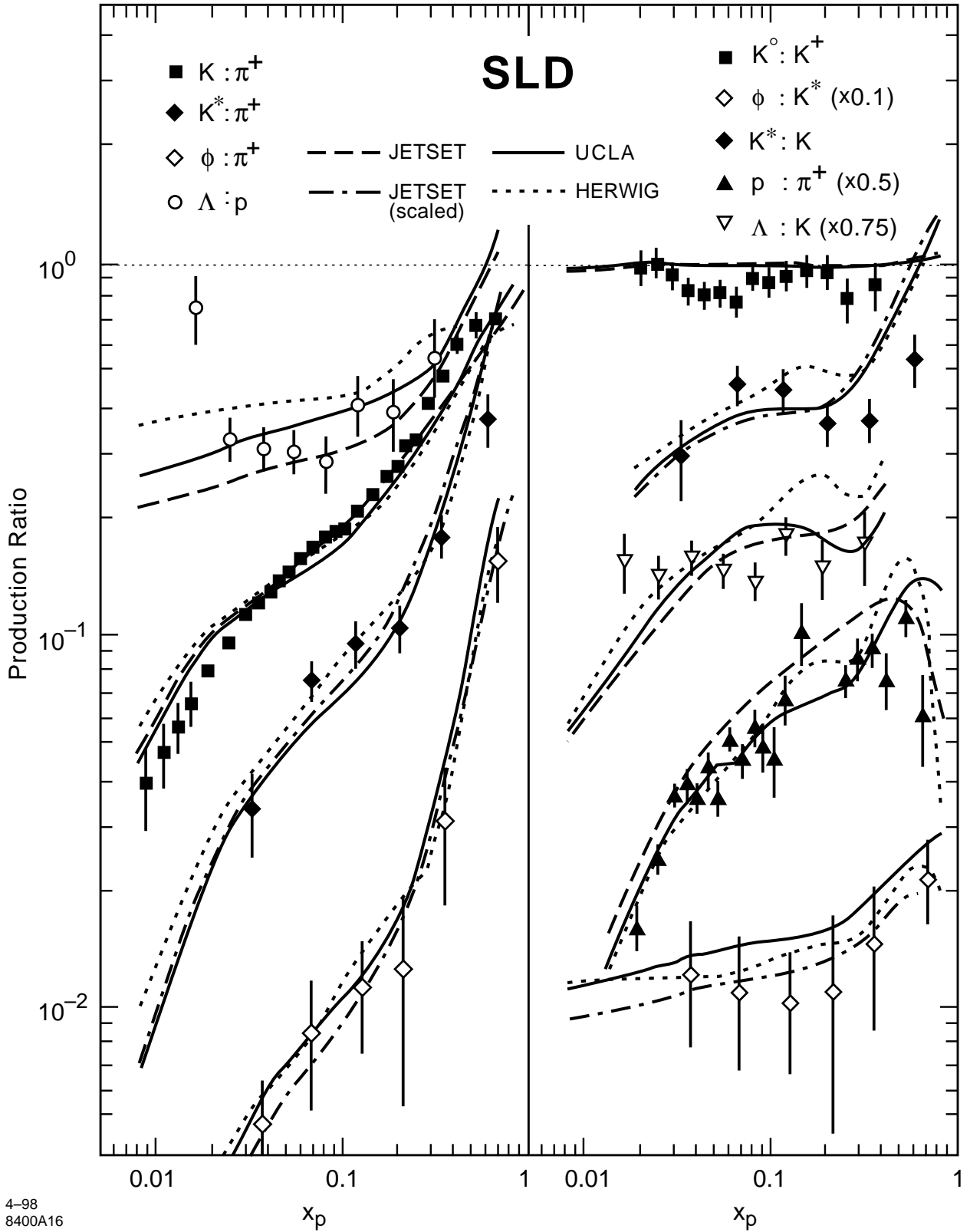
The measured normalized differences are compared with the predictions of the three fragmentation models in fig. 21. All models reproduce the qualitative features of our data. For the baryons, the HERWIG prediction drops below zero in the range in which we have no proton coverage; this behavior might be ruled out with more $\Lambda^0/\bar{\Lambda}^0$ data. The HERWIG and UCLA predictions rise sharply to unity at $x_p \approx 0.4$ and are inconsistent with the proton data. For the mesons all models are consistent with the data.

9 Production Ratios and Fragmentation Parameters

Certain aspects of the fragmentation process can be studied more directly by measuring the relative production of two hadron species that differ by a single quantum number. We have calculated the ratios of differential cross sections for a number of pairs of hadron species, for flavor-inclusive and light-flavor events, taking into account any systematic errors common to the two species. The results are shown for light-flavor events in fig. 22. In the cases where binning was different for the two hadron species in a pair, the ratio was obtained by fitting a curve to the denominator over a region near each x_p value in the numerator. In some cases charged and neutral pseudoscalar kaons were averaged, and are denoted simply “K”. In all cases, charge-conjugate states are included in both numerator and denominator.

The ratios of the strange mesons to pions vary rapidly with x_p . In flavor-inclusive events (not shown), the values of each of these ratios vary over a similar range but show less structure, being consistent with simple powers of x_p for $x_p > 0.04$. The proton:pion ratio also varies rapidly for $x_p < 0.1$. The other ratios shown in fig. 22 are independent of x_p within our errors.

The $K^0:K^\pm$ ratio differs significantly from unity over the range $0.03 < x_p < 0.09$, averaging 0.86 ± 0.03 ; we observe a similar difference in flavor-inclusive events (not shown), as has been observed previously [7]. Assuming that primary charged and neutral kaons are produced equally in the fragmentation process, this implies that some hadron species is pro-



4-98
8400A16

Figure 22: Ratios of measured differential cross sections for various pairs of hadron species in light-flavor events, along with the predictions of the three fragmentation models. In all cases the charge-conjugate states are included in both numerator and denominator. Here, “K” denotes the average of K^0/\bar{K}^0 and K^\pm . The JETSET predictions for the $K^*:\pi^+$, $\phi:\pi^+$, $\phi:K^*$ and $K^*:K$ ratios have been scaled by factors of 2/3, 1/2, 4/3 and 2/3, respectively (see text), in order to clarify the comparison of the momentum dependence.

duced that decays preferentially into charged kaons. Our measured cross sections indicate that decays of ϕ and K^* mesons would each account for only ~ 0.01 of the difference from unity. Decays of D - and B -hadrons cannot be the source of this difference since they have been excluded explicitly.

The predictions of the three fragmentation models are also shown in fig. 22, and all describe the qualitative features of the data. The JETSET prediction for each ratio involving K^* or ϕ mesons differs from the data by a large normalization factor, and those predictions have been scaled by factors derived from fig. 15 in order to compare the momentum dependence with that of the data. All models underestimate the slope of the $K:\pi^+$ ratio, but reproduce those of the $\phi:\pi^+$ and $K^*:\pi^+$ ratios, overestimating the latter ratio only at the highest- x_p point. The x_p dependence of the $p:\pi^+$ ratio is reproduced by all models at low x_p , but only by the JETSET model for $x_p > 0.2$. However the JETSET model shows a normalization difference from the data of about 20%. Similar differences in the model predictions for the $\Lambda:K$ ratio cannot be resolved with the current statistics. No model reproduces the measured $K^0:K^+$ ratio; all predict a roughly constant value of 0.98 in the range of our measurement. All models predict a larger value of the $K^*:K$ ratio at the highest- x_p point than is observed in the data. A similar set of comparisons for flavor-inclusive events (not shown) yielded the same conclusions.

These ratios can be used to study the suppression of baryons, vector mesons and strange hadrons in the fragmentation process. Quantifying such suppression at the primary fragmentation level is problematic due to possible effects of different masses of the two hadron species in the ratio and the fact that decay products populate a different x_p region than their primary parents. We therefore used the JETSET model, in which there are tunable parameters controlling the relative production of baryons, strange hadrons and vector mesons, to extract suppression parameters in the context of that model. We first considered the relative production of pseudoscalar (P) and vector (V) mesons, traditionally expressed in terms of the parameter $P_V = V/(V + P)$. Since we might expect that measured ratios are not the same at very high x_p , where leading hadron production is important, as they are lower x_p , we defined arbitrarily a “fragmentation” region, $0.05 < x_p < 0.25$, and a “leading” region, $x_p > 0.45$. In each region we averaged our measured $K^*:K$ ratio, and compared it with those obtained in the same region from the JETSET generator run with a series of input values of the P_V parameter for strange mesons. We interpolated to find the P_V value at which the model prediction for each ratio was equal to that measured in the data, and these values are listed in table 22 for the two x_p regions and for both flavor-inclusive and light-flavor events. The two measurements in each momentum range are consistent, but the P_V value measured in the fragmentation region is significantly higher than that measured in the leading region for both flavor categories.

We next considered the relative production of baryons (B) and mesons (M), in terms of the parameter $P_B = B/(B + M)$. A similar set of comparisons of our $p:\pi$ and $\Lambda:K$ ratios with the predictions of the JETSET model as P_B was varied yielded the measured P_B values listed in table 23. The four values extracted from the $p:\pi$ ratio are consistent. The value from the $\Lambda:K$ ratio in light-flavor events is consistent with these four, but that in flavor-inclusive events is slightly larger.

Information on the suppression of strangeness is available from several of our measurements. It is conventional to define a suppression factor γ_s as the probability of creating an

Vector:Pseudoscalar Production Parameter P_V		
x_p Range	inclusive	light-flavor
0.055–0.219	0.405 ± 0.020	0.433 ± 0.033
0.439–1.000	0.226 ± 0.029	0.279 ± 0.029

Table 22: Measurements of the vector-meson fraction P_V extracted from the measured $K^*:K$ production ratio in the context of the JETSET model.

Baryon:Meson Production Parameter P_B			
Ratio	x_p Range	inclusive	light-flavor
p: π^\pm	0.055–0.165	0.076 ± 0.003	0.074 ± 0.004
$\Lambda:K$	0.061–0.237	0.101 ± 0.003	0.087 ± 0.005
p: π^\pm	0.493–0.987	0.081 ± 0.006	0.081 ± 0.009

Table 23: Measurements of the baryon fraction P_B in the context of the JETSET model.

$s\bar{s}$ from the vacuum, relative to that of creating a $u\bar{u}$ or $d\bar{d}$, at a given point in the fragmentation process. As has been suggested in ref. [33], the normalized production difference (see section 8) at high x_p between a strange hadron and its antihadron in light quark jets provides a robust way of investigating strangeness suppression for any neutral hadron, such as K^{*0}/\bar{K}^{*0} , that is unlikely to be a decay product of a heavier primary particle. If we assume leading particle dominance, so that \bar{K}^{*0} can be produced only in s and \bar{d} jets, and that the relative production in \bar{d} jets is suppressed by a factor of γ_s , then we expect the normalized difference to be $D_{\bar{K}^{*0}} = (1 - \gamma_s)/(1 + \gamma_s)$. From our point in the bin $0.5 < x_p < 1$ we used this equation to derive a “direct” measurement of $\gamma_s = 0.26 \pm 0.12$, where we first scaled our given $D_{\bar{K}^{*0}}$ value by 0.923 to account for the fact that we assumed contributions from u , d and s jets in the original unfolding, whereas we now assume only d and s contribute. Similarly, assuming dominant production of leading K^\pm and accounting for the different branching fraction and forward-backward asymmetry of up- and down-type events, one expects $1.05D_{K^-} = (1 - 0.55\gamma_s)/(1 + 0.77\gamma_s)$. From this we derive $\gamma_s = 0.41 \pm 0.17$, using our D_{K^-} data in the range $0.47 < x_p < 0.77$.

We also used the JETSET model to predict the normalized differences as a function of γ_s , and to extract from our measured $D_{\bar{K}^{*0}}$ and D_{K^-} the γ_s values listed in table 24. Also listed in table 24 are γ_s values extracted in the context of the JETSET model from our measured $K:\pi^+$, $\phi:K^*$ and $\Lambda:p$ ratios. For each ratio, the values derived from the flavor-inclusive and light-flavor events are consistent. However there is a significant x_p dependence in the values obtained from the $K:\pi^+$ ratio in both flavor categories, and there are several other significant differences between pairs of values from the same flavor category. This indicates that the

Strangeness Suppression Factor, γ_s			
Ratio	x_p Range	inclusive	light-flavor
$D_{\bar{K}^*0}$	0.482–1.000	–	0.194 ± 0.141
D_{K^-}	0.493–0.768	–	0.249 ± 0.110
$K:\pi^+$	0.055–0.219	0.236 ± 0.016	0.266 ± 0.014
$\phi:K^*$	0.048–0.263	0.163 ± 0.027	0.184 ± 0.052
$\Lambda:p$	0.050–0.182	0.339 ± 0.014	0.311 ± 0.032
$K:\pi^+$	0.493–0.768	0.575 ± 0.084	0.483 ± 0.091
$\phi:K^*$	0.482–1.000	0.160 ± 0.060	0.239 ± 0.075

Table 24: Measurements of the strangeness suppression factor γ_s in the context of the JETSET model. The notation D_h refers to the normalized differences discussed in section 8.

JETSET model cannot accommodate all of our data with a single γ_s value and all other parameters set to their default values.

10 Summary and Conclusions

We have measured the production of the seven hadron species π^\pm , K^\pm , K^0/\bar{K}^0 , K^{*0}/\bar{K}^{*0} , ϕ , p/\bar{p} , and $\Lambda^0/\bar{\Lambda}^0$ as a function of scaled momentum x_p over a wide range in hadronic Z^0 decays. The SLD Cherenkov Ring Imaging Detector enabled the clean and efficient identification of stable charged hadrons, yielding precise measurements of their production cross sections, as well as the identification of relatively clean samples of the strange mesons K^{*0}/\bar{K}^{*0} and ϕ reconstructed in decay modes containing charged kaons. Our measurements of differential production cross sections, total cross sections and ratios of production of these hadron species in flavor-inclusive hadronic Z^0 decays are consistent with averages of those from experiments at LEP.

Using the SLD vertex detector to isolate high-purity light- and b -tagged event samples, we have measured the production of these seven hadron species in light-, c - and b -flavor events. Significant differences between flavors were found, consistent with expectations based on the known properties of B and D hadron production and decay. Our π^\pm , K^\pm and p/\bar{p} data at high x_p were used to test the predictions of Gribov and Lipatov for the shape of the x_p distribution of primary leading hadrons as $x_p \rightarrow 1$. We find the predictions of the theory to be consistent with the flavor-inclusive (light-flavor) meson data for $x_p > 0.66$ ($x_p > 0.47$) and with the proton data for $x_p > 0.43$ ($x_p > 0.38$). The shape of the $\xi = -\ln(x_p)$ distribution for each hadron species in events of each flavor is consistent with the Gaussian form predicted by MLLA QCD+LPHD near its peak. The peak positions ξ^* for each hadron species in light-flavor events are more consistent with a monotonic dependence on hadron mass than

those in flavor-inclusive events.

Using the large forward-backward asymmetry induced by the polarized SLC electron beam to separate light quark from light antiquark hemispheres, we have updated our measurements of hadron and antihadron production in light quark jets. Differences are observed at high x_p between baryon and antibaryon production, which is evidence for the production of leading baryons, i.e. baryons that carry the quantum numbers of the initial quark. Differences are also observed for both pseudoscalar and vector K -mesons, which indicate not only leading production of these two hadron species but also that leading strange mesons are produced more often from initial s quarks than from initial u or d quarks.

Our data were used to test the predictions of three fragmentation models with default parameters. In most cases these simulations reproduced the data to within a few percent. However the JETSET 7.4 model predicts too many p/\bar{p} , K^{*0}/\bar{K}^{*0} and ϕ mesons at all x_p , and too many K^\pm and K^0/\bar{K}^0 at low x_p . The UCLA model predicts too many pions in the 2–20 GeV/c range, a shoulder in the x_p distributions for baryons at high x_p , and larger differences between baryon and antibaryon production at high x_p than are seen in our light-quark data. The HERWIG 5.8 model predicts a shoulder in the x_p distribution for most hadron species at high x_p , a large excess of low- x_p pions and kaons in b -flavor events and of medium- x_p pions in c -flavor events, and a rapid variation in the baryon-antibaryon differences as a function of x_p . All models predict a charged:neutral kaon ratio very close to unity, which is inconsistent with our light-flavor and flavor-inclusive data. Also, no model is consistent with the x_p dependence of either our $K:\pi$ ratio or our $K^*:K$ ratio.

We have studied several parameters of the fragmentation process. The differences between kaon and antikaon production in light quark jets allow two new, direct measurements of strangeness suppression at high momentum. We have also used our ratios of production of pairs of hadron species to extract fragmentation parameters in the context of the JETSET model. We find the vector:pseudoscalar meson parameter to be dependent on x_p , and the strangeness suppression parameter to be dependent both on x_p and on the hadron species used to form the ratio.

Acknowledgements

We thank the personnel of the SLAC accelerator department and the technical staffs of our collaborating institutions for their outstanding efforts on our behalf. We thank S. Brodsky and L. Dixon for useful discussions.

References

- [1] See e.g. R.K. Ellis, D.A. Ross, A.E. Terrano, Nucl. Phys. **B178** (1981) 421.
- [2] S. Moretti, RAL-TR-97-065, hep-ph/9711518.
- [3] T.I. Azimov, Y.L. Dokshitzer, V.A. Khoze and S.I. Troyan, Z. Phys. **C27** (1985) 65.
- [4] G. Marchesini and B.R. Webber, Nucl. Phys. **B238** (1984) 1.

- [5] V.N. Gribov and L.N. Lipatov, *Sov. J. Nucl. Phys.* **15** (1973) 675.
- [6] D.H. Saxon, *High Energy Electron-Positron Physics*, Eds. A. Ali and P. Söding, World Scientific (1988), p. 539.
- [7] A. Böhrer, *Phys. Rep.* **291** (1997) 107.
- [8] SLD Collab., K. Abe et al., *Phys. Rev. Lett.* **78** (1997) 3442.
- [9] G. Marchesini et al., *Comp. Phys. Comm.* **67** (1992) 465.
- [10] T. Sjöstrand, *Comp. Phys. Comm.* **82** (1994) 74.
- [11] S. Chun and C. Buchanan, *Phys. Rep.* **292** (1998) 239.
- [12] SLD Design Report, SLAC-Report 273 (1984).
- [13] M.D. Hildreth et al., *Nucl. Inst. Meth.* **A367** (1995) 111.
- [14] C. J. S. Damerell et al., *Nucl. Inst. Meth.* **A288** (1990) 236.
- [15] K. Abe et al., *Nucl. Inst. Meth.* **A343** (1994) 74.
- [16] D. Axen et al., *Nucl. Inst. Meth.* **A238** (1993) 472.
- [17] S. Brandt et al., *Phys. Lett.* **12** (1964) 57;
E. Farhi, *Phys. Rev. Lett.* **39** (1977) 1587.
- [18] SLD Collab., K. Abe et al., *Phys. Rev.* **D53** (1996) 1023.
- [19] K. Abe et al., *Nucl. Inst. and Meth.* **A371** (1996) 195.
- [20] T.J. Pavel, Ph.D. Thesis, Stanford University, January 1997; SLAC-Report-495.
- [21] SLD Collab., K. Abe et al., *Phys. Rev. Lett.* **73** (1994) 25.
- [22] DELPHI Collab., P. Abreu et al., *Nucl. Phys.* **B444** (1995) 3.
- [23] OPAL Collab., P.D. Acton et al., *Z. Phys.* **C63** (1994) 181.
- [24] ALEPH Collab., D. Buskulic et al., *Z. Phys.* **C66** (1995) 355.
- [25] SLD Collab., K. Abe et al., *Phys. Rev. Lett.* **72** (1994) 3145.
- [26] K.G. Baird, Ph.D. Thesis, Rutgers University, December 1995; SLAC-Report-95-483.
- [27] Particle Data Group, *Phys. Rev.* **D54** (1996) 1.
- [28] M.O. Dima, Ph.D. Thesis, Colorado State University, March 1997; SLAC-Report-505.
- [29] ALEPH Collab., D. Buskulic et al., *Z. Phys.* **C69** (1996) 379.
- [30] SLD Collab., K. Abe et al., *Phys. Rev.* **D53** (1996) 2271.

- [31] SLD Collab., K. Abe et al., Phys. Lett. **B386** (1996) 475.
- [32] See e.g. DELPHI Collab., P. Abreu et al., Phys. Lett. **B416** (1998) 247.
- [33] G. D. Lafferty, Phys. Lett. **B353** (1995) 541.

**List of Authors

K. Abe,⁽²⁾ K. Abe,⁽¹⁹⁾ T. Abe,⁽²⁷⁾ I. Adam,⁽²⁷⁾ T. Akagi,⁽²⁷⁾ N. J. Allen,⁽⁴⁾ A. Arodzero,⁽²⁰⁾
W.W. Ash,⁽²⁷⁾ D. Aston,⁽²⁷⁾ K.G. Baird,⁽²⁶⁾ C. Baltay,⁽³⁷⁾ H.R. Band,⁽³⁶⁾ M.B. Barakat,⁽¹⁴⁾
O. Bardon,⁽¹⁷⁾ T.L. Barklow,⁽²⁷⁾ J.M. Bauer,⁽¹⁶⁾ G. Bellodi,⁽²¹⁾ R. Ben-David,⁽³⁷⁾
A.C. Benvenuti,⁽³⁾ G.M. Bilei,⁽²³⁾ D. Bisello,⁽²²⁾ G. Blaylock,⁽¹⁵⁾ J.R. Bogart,⁽²⁷⁾
B. Bolen,⁽¹⁶⁾ G.R. Bower,⁽²⁷⁾ J. E. Brau,⁽²⁰⁾ M. Breidenbach,⁽²⁷⁾ W.M. Bugg,⁽³⁰⁾
D. Burke,⁽²⁷⁾ T.H. Burnett,⁽³⁵⁾ P.N. Burrows,⁽²¹⁾ A. Calcaterra,⁽¹¹⁾ D.O. Caldwell,⁽³²⁾
D. Calloway,⁽²⁷⁾ B. Camanzi,⁽¹⁰⁾ M. Carpinelli,⁽²⁴⁾ R. Cassell,⁽²⁷⁾ R. Castaldi,⁽²⁴⁾
A. Castro,⁽²²⁾ M. Cavalli-Sforza,⁽³³⁾ A. Chou,⁽²⁷⁾ E. Church,⁽³⁵⁾ H.O. Cohn,⁽³⁰⁾
J.A. Coller,⁽⁵⁾ M.R. Convery,⁽²⁷⁾ V. Cook,⁽³⁵⁾ R. Cotton,⁽⁴⁾ R.F. Cowan,⁽¹⁷⁾ D.G. Coyne,⁽³³⁾
G. Crawford,⁽²⁷⁾ C.J.S. Damerell,⁽²⁵⁾ M. N. Danielson,⁽⁷⁾ M. Daoudi,⁽²⁷⁾ N. de Groot,⁽²⁷⁾
R. Dell'Orso,⁽²³⁾ P.J. Dervan,⁽⁴⁾ R. de Sangro,⁽¹¹⁾ M. Dima,⁽⁹⁾ A. D'Oliveira,⁽⁶⁾
D.N. Dong,⁽¹⁷⁾ P.Y.C. Du,⁽³⁰⁾ R. Dubois,⁽²⁷⁾ B.I. Eisenstein,⁽¹²⁾ V. Eschenburg,⁽¹⁶⁾
E. Etzion,⁽³⁶⁾ S. Fahey,⁽⁷⁾ D. Falciari,⁽¹¹⁾ C. Fan,⁽⁷⁾ J.P. Fernandez,⁽³³⁾ M.J. Fero,⁽¹⁷⁾
K. Flood,⁽¹⁵⁾ R. Frey,⁽²⁰⁾ T. Gillman,⁽²⁵⁾ G. Gladding,⁽¹²⁾ S. Gonzalez,⁽¹⁷⁾ E.L. Hart,⁽³⁰⁾
J.L. Harton,⁽⁹⁾ A. Hasan,⁽⁴⁾ K. Hasuko,⁽³¹⁾ S. J. Hedges,⁽⁵⁾ S.S. Hertzbach,⁽¹⁵⁾
M.D. Hildreth,⁽²⁷⁾ J. Huber,⁽²⁰⁾ M.E. Huffer,⁽²⁷⁾ E.W. Hughes,⁽²⁷⁾ X. Huynh,⁽²⁷⁾
H. Hwang,⁽²⁰⁾ M. Iwasaki,⁽²⁰⁾ D. J. Jackson,⁽²⁵⁾ P. Jacques,⁽²⁶⁾ J.A. Jaros,⁽²⁷⁾ Z.Y. Jiang,⁽²⁷⁾
A.S. Johnson,⁽²⁷⁾ J.R. Johnson,⁽³⁶⁾ R.A. Johnson,⁽⁶⁾ T. Junk,⁽²⁷⁾ R. Kajikawa,⁽¹⁹⁾
M. Kalelkar,⁽²⁶⁾ Y. Kamyshkov,⁽³⁰⁾ H.J. Kang,⁽²⁶⁾ I. Karliner,⁽¹²⁾ H. Kawahara,⁽²⁷⁾
Y. D. Kim,⁽²⁸⁾ R. King,⁽²⁷⁾ M.E. King,⁽²⁷⁾ R.R. Kofler,⁽¹⁵⁾ N.M. Krishna,⁽⁷⁾
R.S. Kroeger,⁽¹⁶⁾ M. Langston,⁽²⁰⁾ A. Lath,⁽¹⁷⁾ D.W.G. Leith,⁽²⁷⁾ V. Lia,⁽¹⁷⁾ C.-J. S. Lin,⁽²⁷⁾
X. Liu,⁽³³⁾ M.X. Liu,⁽³⁷⁾ M. Loretì,⁽²²⁾ A. Lu,⁽³²⁾ H.L. Lynch,⁽²⁷⁾ J. Ma,⁽³⁵⁾
G. Mancinelli,⁽²⁶⁾ S. Manly,⁽³⁷⁾ G. Mantovani,⁽²³⁾ T.W. Markiewicz,⁽²⁷⁾ T. Maruyama,⁽²⁷⁾
H. Masuda,⁽²⁷⁾ E. Mazzucato,⁽¹⁰⁾ A.K. McKemey,⁽⁴⁾ B.T. Meadows,⁽⁶⁾ G. Menegatti,⁽¹⁰⁾
R. Messner,⁽²⁷⁾ P.M. Mockett,⁽³⁵⁾ K.C. Moffeit,⁽²⁷⁾ T.B. Moore,⁽³⁷⁾ M. Morii,⁽²⁷⁾
D. Muller,⁽²⁷⁾ V. Murzin,⁽¹⁸⁾ T. Nagamine,⁽³¹⁾ S. Narita,⁽³¹⁾ U. Nauenberg,⁽⁷⁾ H. Neal,⁽²⁷⁾
M. Nussbaum,⁽⁶⁾ N. Oishi,⁽¹⁹⁾ D. Onoprienko,⁽³⁰⁾ L.S. Osborne,⁽¹⁷⁾ R.S. Panvini,⁽³⁴⁾
H. Park,⁽²⁰⁾ C. H. Park,⁽²⁹⁾ T.J. Pavel,⁽²⁷⁾ I. Peruzzi,⁽¹¹⁾ M. Piccolo,⁽¹¹⁾ L. Piemontese,⁽¹⁰⁾
E. Pieroni,⁽²⁴⁾ K.T. Pitts,⁽²⁰⁾ R.J. Plano,⁽²⁶⁾ R. Prepost,⁽³⁶⁾ C.Y. Prescott,⁽²⁷⁾
G.D. Punkar,⁽²⁷⁾ J. Quigley,⁽¹⁷⁾ B.N. Ratcliff,⁽²⁷⁾ T.W. Reeves,⁽³⁴⁾ J. Reidy,⁽¹⁶⁾
P.L. Reinertsen,⁽³³⁾ P.E. Rensing,⁽²⁷⁾ L.S. Rochester,⁽²⁷⁾ P.C. Rowson,⁽⁸⁾ J.J. Russell,⁽²⁷⁾
O.H. Saxton,⁽²⁷⁾ T. Schalk,⁽³³⁾ R.H. Schindler,⁽²⁷⁾ B.A. Schumm,⁽³³⁾ J. Schwiening,⁽²⁷⁾
S. Sen,⁽³⁷⁾ V.V. Serbo,⁽³⁶⁾ M.H. Shaevitz,⁽⁸⁾ J.T. Shank,⁽⁵⁾ G. Shapiro,⁽¹³⁾ D.J. Sherden,⁽²⁷⁾
K. D. Shmakov,⁽³⁰⁾ C. Simopoulos,⁽²⁷⁾ N.B. Sinev,⁽²⁰⁾ S.R. Smith,⁽²⁷⁾ M. B. Smy,⁽⁹⁾
J.A. Snyder,⁽³⁷⁾ H. Staengle,⁽⁹⁾ A. Stahl,⁽²⁷⁾ P. Stamer,⁽²⁶⁾ R. Steiner,⁽¹⁾ H. Steiner,⁽¹³⁾
M.G. Strauss,⁽¹⁵⁾ D. Su,⁽²⁷⁾ F. Suekane,⁽³¹⁾ A. Sugiyama,⁽¹⁹⁾ S. Suzuki,⁽¹⁹⁾ M. Swartz,⁽²⁷⁾
A. Szumilo,⁽³⁵⁾ T. Takahashi,⁽²⁷⁾ F.E. Taylor,⁽¹⁷⁾ J. Thom,⁽²⁷⁾ E. Torrence,⁽¹⁷⁾
N. K. Toumbas,⁽²⁷⁾ A.I. Trandafir,⁽¹⁵⁾ J.D. Turk,⁽³⁷⁾ T. Usher,⁽²⁷⁾ C. Vannini,⁽²⁴⁾
J. Va'vra,⁽²⁷⁾ E. Vella,⁽²⁷⁾ J.P. Venuti,⁽³⁴⁾ R. Verdier,⁽¹⁷⁾ P.G. Verdini,⁽²⁴⁾ S.R. Wagner,⁽²⁷⁾
D. L. Wagner,⁽⁷⁾ A.P. Waite,⁽²⁷⁾ Walston, S.,⁽²⁰⁾ J. Wang,⁽²⁷⁾ C. Ward,⁽⁴⁾ S.J. Watts,⁽⁴⁾

A.W. Weidemann,⁽³⁰⁾ E. R. Weiss,⁽³⁵⁾ J.S. Whitaker,⁽⁵⁾ S.L. White,⁽³⁰⁾ F.J. Wickens,⁽²⁵⁾
B. Williams,⁽⁷⁾ D.C. Williams,⁽¹⁷⁾ S.H. Williams,⁽²⁷⁾ S. Willocq,⁽²⁷⁾ R.J. Wilson,⁽⁹⁾
W.J. Wisniewski,⁽²⁷⁾ J. L. Wittlin,⁽¹⁵⁾ M. Woods,⁽²⁷⁾ G.B. Word,⁽³⁴⁾ T.R. Wright,⁽³⁶⁾
J. Wyss,⁽²²⁾ R.K. Yamamoto,⁽¹⁷⁾ J.M. Yamartino,⁽¹⁷⁾ X. Yang,⁽²⁰⁾ J. Yashima,⁽³¹⁾
S.J. Yellin,⁽³²⁾ C.C. Young,⁽²⁷⁾ H. Yuta,⁽²⁾ G. Zapalac,⁽³⁶⁾ R.W. Zdarko,⁽²⁷⁾ J. Zhou.⁽²⁰⁾

(The SLD Collaboration)

- ⁽¹⁾ *Adelphi University, South Avenue- Garden City, NY 11530,*
⁽²⁾ *Aomori University, 2-3-1 Kohata, Aomori City, 030 Japan,*
⁽³⁾ *INFN Sezione di Bologna, Via Irnerio 46 I-40126 Bologna (Italy),*
⁽⁴⁾ *Brunel University, Uxbridge, Middlesex - UB8 3PH United Kingdom,*
⁽⁵⁾ *Boston University, 590 Commonwealth Ave. - Boston, MA 02215,*
⁽⁶⁾ *University of Cincinnati, Cincinnati, OH 45221,*
⁽⁷⁾ *University of Colorado, Campus Box 390 - Boulder, CO 80309,*
⁽⁸⁾ *Columbia University, Nevis Laboratories P.O.Box 137 - Irvington, NY 10533,*
⁽⁹⁾ *Colorado State University, Ft. Collins, CO 80523,*
⁽¹⁰⁾ *INFN Sezione di Ferrara, Via Paradiso, 12 - I-44100 Ferrara (Italy),*
⁽¹¹⁾ *Lab. Nazionali di Frascati, Casella Postale 13 I-00044 Frascati (Italy),*
⁽¹²⁾ *University of Illinois, 1110 West Green St. Urbana, IL 61801,*
⁽¹³⁾ *Lawrence Berkeley Laboratory, Dept. of Physics 50B-5211 University of California-
Berkeley, CA 94720,*
⁽¹⁴⁾ *Louisiana Technical University, ,*
⁽¹⁵⁾ *University of Massachusetts, Amherst, MA 01003,*
⁽¹⁶⁾ *University of Mississippi, University, MS 38677,*
⁽¹⁷⁾ *Massachusetts Institute of Technology, 77 Massachusetts Avenue Cambridge, MA
02139,*
⁽¹⁸⁾ *Moscow State University, Institute of Nuclear Physics 119899 Moscow Russia,*
⁽¹⁹⁾ *Nagoya University, Nagoya 464 Japan,*
⁽²⁰⁾ *University of Oregon, Department of Physics Eugene, OR 97403,*
⁽²¹⁾ *Oxford University, Oxford, OX1 3RH, United Kingdom,*
⁽²²⁾ *Universita di Padova, Via F. Marzolo, 8 I-35100 Padova (Italy),*
⁽²³⁾ *Universita di Perugia, Sezione INFN, Via A. Pascoli I-06100 Perugia (Italy),*
⁽²⁴⁾ *INFN, Sezione di Pisa, Via Livornese, 582/AS Piero a Grado I-56010 Pisa (Italy),*
⁽²⁵⁾ *Rutherford Appleton Laboratory, Chilton, Didcot - Oxon OX11 0QX United Kingdom,*
⁽²⁶⁾ *Rutgers University, Serin Physics Labs Piscataway, NJ 08855-0849,*
⁽²⁷⁾ *Stanford Linear Accelerator Center, 2575 Sand Hill Road Menlo Park, CA 94025,*
⁽²⁸⁾ *Sogang University, Ricci Hall Seoul, Korea,*
⁽²⁹⁾ *Soongsil University, Dongjakgu Sangdo 5 dong 1-1 Seoul, Korea 156-743,*
⁽³⁰⁾ *University of Tennessee, 401 A.H. Nielsen Physics Bldg. - Knoxville, Tennessee
37996-1200,*
⁽³¹⁾ *Tohoku University, Bubble Chamber Lab. - Aramaki - Sendai 980 (Japan),*
⁽³²⁾ *U.C. Santa Barbara, 3019 Broida Hall Santa Barbara, CA 93106,*
⁽³³⁾ *U.C. Santa Cruz, Santa Cruz, CA 95064,*
⁽³⁴⁾ *Vanderbilt University, Stevenson Center, Room 5333 P.O.Box 1807, Station B
Nashville, TN 37235,*
⁽³⁵⁾ *University of Washington, Seattle, WA 98105,*
⁽³⁶⁾ *University of Wisconsin, 1150 University Avenue Madison, WI 53706,*

⁽³⁷⁾ *Yale University, 5th Floor Gibbs Lab. - P.O.Box 208121 - New Haven, CT 06520-8121.*